# UNIVERSITÀ DEGLI STUDI DI PARMA

**Corso di Dottorato in**

**Progettazione e Sintesi di Composti Biologicamente Attivi**

*Ciclo XXVIII*

# Application of Molecular Modelling studies to the search of novel approaches for neuroprotection and stem cells applications


Coordinatore

Chiar.mo Prof. Marco Mor

Tutor

Chiar.mo Prof. Marco Mor

Dottoranda

Laura Scalvini

# Summary

# ENDOCANNABINOIDS DEGRADING ENZYMES AS TARGET FOR THE DEVELOPMENT OF NOVEL APPROACHES FOR NEUROPROTECTION

# 1. The endocannabinoid system: an overview

The last decades of last Century allowed the discovery of true milestones in the field of cannabinoid research, such as the characterisation of cannabinoid receptors[1] and the identification of *N*-arachidonoylethanolamide (anandamide; AEA) in 1992 as the first endogenous cannabinoid-like substance[2]. Since then, a great deal of effort has gone into the characterisation of the components of the complex endocannabinoid signalling system, and into the understanding of their role in the regulation of the synaptic transmission. Shortly after the isolation of AEA, a second endogenous ligand for cannabinoid receptors, 2-arachidonoyl-*sn*-glycerol (2-AG), was identified and recognised as a primary component of the endocannabinoid-mediated neurotransmission in the CNS[3–5] (Figure 1).

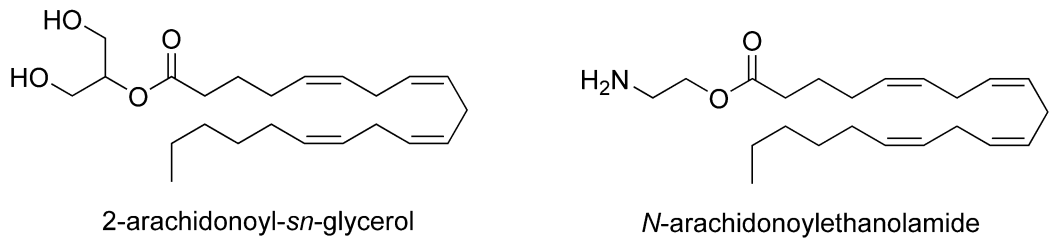


*Figure 1 Chemical structures of the endocannabinoids 2-AG (left) and AEA (right)*

At the same time, evidences showing that the cannabinoid receptors, $CB_1$ and $CB_2$, are the most abundant GPCRs in the brain, and that the cannabinoid-dependent effects are suppressed by the genetic ablation of the cannabinoid receptor type 1 ($CB_1$), corroborated the hypothesis that the endocannabinoid signalling is a major actor in the modulation of synaptic communication. $CB_1$ receptors are abundant in all types of CNS synapses, including GABAergic and glutamatergic axons in cortical, neocortical, hippocampal, hypothalamic and cerebellar neuron populations, and cholinergic, noradrenergic and serotoninergic axons of subcortical ascending pathways[6–11]. On the other hand, $CB_2$ receptors are particularly abundant on immune cells and on activated microglia, which suggests that these receptors play a crucial role in the modulation of the inflammatory component characterising neurodegenerative pathologies[12,13].

The $CB_1$ receptor and its endogenous ligands 2-AG and AEA are thus key actors in the modulation of synaptic transmission, and perturbations in the regulation of the endocannabinoid system may lead to severe consequences in the CNS.

Going to details, experimental evidences collected in the last decades point to the endocannabinoid system as an efficient biological system, dedicated to the protection and recovery from neural damages and injuries.

Their hydrophobic nature makes the endocannabinoids an unconventional class of neurotransmitters[14,15]. They are not stored in synaptic vesicles, but are synthesised on demand through the cleavage of membrane phospholipid precursors. AEA and 2-AG are thus produced as a response to finely timed and positioned *stimuli*, and exert their signalling actions through the activation of the $CB_1$ receptors in central synapses, and of the $CB_2$ receptors in immune system and microglia cells[16]. Notably, the architecture and distribution of the ECB system components outline that AEA and 2-AG act as retrograde messengers in the CNS. Immunohistochemical studies have revealed that $CB_1$ receptors are mainly localised on presynaptic GABAergic interneurons of the hippocampus and of the most axon terminals of central and peripheral nervous system[17]. Evidences showing that $CB_1$ agonists are able to suppress the release of GABA are in accordance with the retrograde-messenger function exerted by the endocannabinoids[18,19].

Moreover, electrophysiological studies revealed that the depolarisation of postsynaptic neurons determines a short-term reduction of GABA release from terminals innervating the same postsynaptic neurons[8]. This phenomenon, known as depolarisation-induced suppression of inhibition (DSI), supported the hypothesis of the existence of retrograde signalling-based regulation of specific neurons populations in the brain. The localisation of $CB_1$ receptors in presynaptic axons, and evidences showing that selective $CB_1$ antagonists inhibit the depolarisation-induced suppression of excitation (DSE)[20] proved that the endocannabinoid system plays a fundamental role in the retrograde control of synaptic communication of GABAergic neurons[17], and in several other forms of synaptic plasticity[21].

Several evidences strongly support the fact that $CB_1$ receptors always mediate a response determining the reduction of neurotransmitter release, regardless the physiological nature of the synapsis (i.e., GABAergic or glutamatergic) and its anatomical localisation within the CNS. Nonetheless, this event is affected by a different time course. For example, the

short-term neurotransmission depression has a very rapid onset, but is a transient event. On the other hand, long-term depression lasts for a longer time interval, but is characterised by a slower inception[22]. These differences, observed in the time scale of the $CB_1$-mediated effects, are strictly related to the specific alteration in the downstream signal transduction produced. While the short-term depression is associated to the inhibition of voltage-gated $Ca^{2+}$ channels, long-term regulation of synaptic transmission is involved in the downregulation of the adenylyl cyclase-protein kinase A[23].

Although 2-AG and AEA share some functional properties, differences in the *stimulus*-dependent response and alteration of these neurotransmitters levels have been observed, suggesting that the production of 2-AG or AEA is strictly controlled by different upstream (pato-)physiological events, and that these events are strongly influenced by the specific neural circuits they take place in. For example, 2-AG acts as the principle retrograde messenger in most forms of homo- and heterosynaptic short-term depression and in several forms of long-term depression[24,25]. On the other hand, AEA is involved in the maintenance of synapses homeostasis acting as a retrograde messenger[26–30], and exerts other functions through the activation of the postsynaptic transient receptor potential (TRP)$V_1$ receptors[31,32]. AEA and 2-AG appear thus to have distinct and complementary roles mediated by $CB_1$ receptors situated in diverse cell types and synaptic circuits. The different functions exerted by these neuromodulators also reflect the diverse and complementary distribution of the enzymatic machinery that is involved in their hydrolytic deactivation. Monoglyceride lipase (MGL), the 2-AG degrading enzyme, is situated into the presynaptic domain of neural circuits, in close proximity to $CB_1$ receptors[17,33], while fatty acid amide hydrolase (FAAH), which hydrolyses AEA, is predominantly situated on the intracellular membrane of postsynaptic neurons[34].

Differences between 2-AG- and AEA-mediated effects are also related to the timescale they occur at; while phasic events, including DSI, are mediated by 2-AG, tonic signalling engages both 2-AG and AEA, although under different pathological and physiological conditions. Although AEA and 2-AG seem to be involved in parallel and complementary signalling pathways, their actions interplay in specific endocannabinoid-mediated events. For example, the single inhibition of FAAH or MGL is not sufficient to evoke catalepsy or drug-discrimination, which are typical side effects related to the administration of $CB_1$

agonists. On the other hand, the simultaneous inhibition of FAAH and MGL produces $\Delta^9$-THC-like effects, including drug discrimination behaviours, suggesting that the combination of 2-AG and AEA actions is fundamental for the fully activation of $CB_1$ receptors.

## *1.1 Endocannabinoids metabolism*

Although a great deal has been learned about the endocannabinoid system and about the effects mediated by 2-AG and AEA, the overall view of the complex metabolism of these neuromodulators still lacks important details to be complete. While a comprehensive description of the events that lead to the synthesis and degradation of 2-AG has been provided, the mechanism laying behind the biosynthesis of anandamide, and the pato-physiological events promoting it, are still unclear.

2-AG is produced through the cleavage of the membrane precursor phosphatidylinositol-4,5-bisphosphate (PIP2), which is converted into the second messenger 1,2-diacylglycerol (DAG)[5]. DAG is a lipid messenger itself, being involved in the modulation of protein kinase C, but also serves as substrate for the enzyme diacylglycerol lipase-α (DGL-α)[35,36,15,5], which catalyses the hydrolysis of DAG into 2-AG. Notably, DGL-α distribution in postsynaptic domains of central glutamatergic synapses overrides the population of metabotropic glutamate receptors ($mGluR_1$ and $mGluR_5$)[37–39]. Interestingly, both mGlu receptors and DGL-α present a binding motif for the synaptic scaffold protein Homer[40,41], which enables the cross-linking activation of DGL-α, as a consequence of mGluR activation. This complex and finely tuned signalling mechanism forms the perisynaptic signalling machinery (PSM)[42], which converts the increase of glutamate levels into a trigger for the production of 2-AG and the subsequent activation of presynaptic $CB_1$ receptors, producing a negative-feedback signal. The 2-AG effects are finally terminated by its hydrolytic deactivation by the serine hydrolase MGL, which accounts for more than 80% of total 2-AG degradation *in vitro,* and thus represents the major 2-AG degrading enzyme[33,43,44]. Two other serine hydrolases play a secondary role in 2-AG hydrolysis, ABHD-6[45,46] and ABHD-12[47], which account for ≈9% and ≈4%, respectively, of 2-AG degradation. More specifically, ABHD-6 is located postynaptically, and participates in the modulation of 2-AG-dependendent neural

transmission, while ABHD-12 catalyses the hydrolysis of different lipid substrates. Beside MGL and ABHD-6, cyclooxygenase-2 (COX2) has recently been discovered as a regulator of the endocannabinoids levels[48–50] and, specifically, of 2-AG activity[51,52]. COX-2 catalyses the oxidation of 2-AG and AEA, and the subsequent production of several secondary messengers, including prostaglandin $E_2$ glycerol ester ($PGE_2$) and other prostaglandins mediating neural inflammation[53–55]. These data reveal a wider landscape for the endocannabinoids-mediated signalling, which in its complexity appears as a crossroad between multiple physiological processes.

While the information about 2-AG biosynthetic route have depicted a comprehensive representation of the events leading to 2-AG production and release, the reactions involved in AEA biosynthesis are still controversial and not completely understood. A "canonical route", hypothesised by different research groups, suggests a model in which AEA is released as the product of the hydrolysis of the precursor *N*-arachidonoyl-phosphatidylethanolamide (NAPE), catalysed by the enzyme phospholipase D (PLD)[56–58]. The NAPE-PLD, however, catalyses only the last step of AEA biosynthesis, while the enzymes responsible for the production of diarachidonoyl-phosphatidylcholine and NAPE are still mysterious. Notably, *stimuli* related to an increase of intracellular calcium levels determine a rapid and transient enhancement of NAPE concentration.

As for 2-AG, AEA is degraded through a two-step mechanism, involving a selective carrier-based uptake. AEA is finally hydrolysed by FAAH[59–63], an amidase-signature enzyme, which is also involved in the degradation of non-cannabinoid fatty acid ethanolamides such as palmitoylethanolamide (PEA) and oleoylethanolamide (OEA), and fatty acyl esters, including 2-AG, at least *in vitro*[64]. Although these evidences initially suggested the hypothesis that FAAH might be involved in the hydrolysis of both AEA and 2-AG, experimental data showing that FAAH inhibition, or genetic ablation, affect 2-AG levels, clearly indicated that the degrading pathways of 2-AG and AEA are separated[33,43,44,65,66].

## *1.2 Alteration of the endocannabinoid system in neurodegenerative disorders: therapeutic perspectives*

The endocannabinoid system has been related to the regulation of several physiological events. For example, it has been shown that 2-AG plays a crucial role in the neural network activity that modulates cognition, nociception, and development of neurons from neural progenitor cells. Similarly, AEA regulates the stress-dependent synaptic plasticity in the amygdala, stress responses and anxiety, and contributes to the modulation of nociceptive transmission. On the other hand, one of the most important applications of the endocannabinoids is the retrograde regulation of the synaptic activity. The raising of glutamate levels is a hallmark of traumatic events leading to neural damage, including cerebral ischemia and epileptic seizures. The abnormal enhancement of the glutamate levels associated to neural insults, on the other hand, triggers the biosynthesis and the release of the endocannabinoids, and thus promote the $CB_1$-dependent reduction of excitotoxicity and neuroprotection.

Notably, in several neurological disorders the malfunctioning of the endocannabinoid signalling is a distinctive and manifest characteristic.

Experimental data show that the selective inhibition or genetic ablation of $CB_1$ receptors on glutamatergic neurons lead to the reduction of seizure threshold, and to an augmented probability of neuronal death in epilepsy mouse models. The expression $CB_1$ receptors and DGL-α, which is responsible for 2-AG synthesis, appears to be downregulated in subjects affected by intractable temporal lobe epilepsy[67,68]. Moreover, the cross-linking mechanism of DGL-α and $mGluR_5$ in glutamatergic terminals is compromised by a subnormal level of the long isoform of the synaptic scaffold protein Homer. Taken together, these evidences clearly point out that the entire perisynaptic signalling machinery involved in 2-AG-mediated neuromodulation is compromised in patients affected by epilepsy.

Further evidences support the hypothesis of a severe impairment of the endocannabinoid signalling related to CNS disorders characterised by neuronal damages[69–71], including closed head injury[72], cerebral ischemia[73–77] and autoimmune encephalomyelitis[78], and that the ECB system is involved in the recovery of physiological functions after a localised and circumscribed damage.

On the other hand, ECB system impairment has been related to severe chronic neural disorders. Neurodegenerative diseases are associated with a progressive decline of normal functions exerted by the CNS, including cognitive processes and the regulation of motility, which are determined by the abnormal alteration of signalling mechanisms and, eventually, are related to modifications of the normal histological structure and functions. The accumulation of toxic metabolic products, misfolded macromolecules and non-functional organelles lead to the loss of normal brain functionalities coupled with an alteration of the overall brain architecture. The ECB system influences the neural activity, producing neuroprotective effects mediated by the activation of $CB_1$ receptors, and regulating the activated glia responses through the $CB_2$ receptors. The CB receptors, their endogenous substrates and the enzymatic machinery involved in their metabolism thus play a crucial role in contrasting the progression of neurodegenerative pathologies, such as Parkinson's disease (PD), Huntington's disease[79–81], multiple sclerosis[69,82–85] and Alzheimer's disease (AD)[86–88].

The ECB system represents an extraordinarily important target for the treatment of neural disorders. Nonetheless, beside the benefits elicited by the direct activation of CB receptors, the observation of severe side effects, including tolerance, physical dependence[89], psychoactive effects[90–92], impairment of sensorimotor gating[93,94], related to the chronic administration of CB agonists, have been raising strong liabilities against their clinical development. In this perspective, the modulation of the enzymes responsible for the degradation of the endocannabinoids represents an attractive strategy in order to uncouple the detrimental and undesired effects from the beneficial outcomes deriving from the activation of CB receptors.

# 2. MGL as a promising target for neuroprotection

## *2.1 MGL is the main 2-AG degrading enzyme*

The degradation of 2-AG consists of a two-step mechanism, starting with a selective carrier-based uptake into cells, which is followed by the hydrolytic cleavage of the glycerol-ester head. While MGL has been purified for the first time in 1976[95], it has been identified as the main 2-AG hydrolysing enzyme only more recently[33,43,44]. MGL is a serine hydrolase that catalyses the degradation of 2- and 1-monoglycerides into glycerol and fatty acids.

RNAi-mediated silencing experiments and the ablation of the gene encoding for MGL have confirmed that this enzyme exerts a crucial role in the physiological deactivation of 2-AG. In contrast to FAAH, MGL population is circumscribed to specific regions of the CNS, such as the cerebellum, the cortex and the anterodorsal nucleus of the thalamus.

MGL biological functions are not limited to the degradation of 2-AG, and mediate the production of non-esterified arachidonic acid as precursor for the synthesis of eicosanoids in several cell types. Nonetheless, its localization overlapping the distribution of $CB_1$ receptors in most central synapses makes MGL the key actor in the regulation of 2-AG levels in the CNS.

### *2.1.1 Characterisation of MGL*

In the last four decades, a great deal of effort has gone into the characterisation of the structure and functions of MGL. Rat, mouse and human MGL are characterised by a 303 amino acids sequence, with 84.2% and 83.8%, respectively, of sequence identity for rMGL and mMGL with hMGL, and 92% of sequence identity for rMGL with mMGL. Several experiments, including cloning[96–98], site-directed mutagenesis[97] and mass-spectrometry[99,100] analysis helped to delineate the mechanisms behind MGL-mediated hydrolysis of 2-AG, and to identify the highly conserved catalytic triad consisting of S122, D239 and H269.

Interestingly, experimental data showing that MGL activity is affected by the action of cysteine-reacting compounds such as *p*-chloromercuribenzoic acid (*p*CMB), mercury chloride ($Hg_2Cl_2$) and *N*-ethylmaleimide supported the hypothesis that MGL is characterised by at least one sulfhydryl-sensitive site that is required for the maintenance of

the enzymatic activity[101]. Different research groups have been contributing to the characterisation of the role of the cysteine residues that modulate MGL activity and to their localisation. The first homology model of rMGL identified C208 and C242 as critical residues near the catalytic site, while biological results and mass-spectrometry data provided evidences for irreversible inhibition mediated by the formation of covalent adducts between maleimide-based ligands and C208 and C242[99,101]. Beside maleimide-based scaffolds, other cysteine targeting compounds, including disulfiram (tetraethylthiuram disulphide), isothiazolinone-based compounds and natural terpenoids have been evaluated for their ability to regulate MGL activity by interacting with C201 and C208.

While the localisation of the critical cysteine residues has been determined by X-ray experiments, mutagenesis data shed light on the impact of C201, C208 and C242 on hMGL activity. Interestingly, the single point mutation of C242 to alanine is sufficient to modify the balance of the monoglyceride isomers hydrolytic reaction catalysed by hMGL (*sn*-1 *vs* *sn*-2)[102]. Because of C242 close proximity to the catalytic triad, its mutation to alanine compromises the binding of nucleophilic serine-targeting fluorophosphonate probe TAMRA-FP, which is used as a probe to characterise the profile of catalytically active serine hydrolase in activity-based protein profiling experiments. Taken together, these data suggest that C242 has a fundamental role in the substrate recognition, binding and enzymatic transformation events.

Although experimental data have been raising C201 and C208 as regulatory cysteine residues, targeted by specific classes of inhibitors, the single point mutations C201A and C208A do not affect the kinetics properties of MGL[103].

## *2.2 MGL structure and functions*

### *2.2.1 MGL crystal structures*

MGL is a member of the α/β hydrolase superfamily of enzymes, which include ester hydrolases, peptide hydrolases, lipid hydrolases, dehalogenases and C-C bond breaking enzymes. The members of this superfamily are characterised by a conserved β-sheet core structure, composed by seven parallel and one antiparallel strands, that is surrounded by α helices. While the β-core represents a highly conserved motif among the members of α/β

hydrolase superfamily, a variable and flexible structural element, called “lid”, or “cap” domain buries the more rigid core region of the enzyme, hiding and shaping at the same time the region of the catalytic site.

An exhaustive overview of the three-dimensional features and of the structure of hMGL active site has been provided by the determination of several crystal structures. The first crystal structures of the enzyme have been recently disclosed by two distinct research groups (PDB: 3HJU, 3JWE/3JW8)[104,105]. The structures present two protein per asymmetric unit, each with the catalytic site access oriented towards the phospholipid bilayer. hMGL presents the typical three-dimensional architecture shared by the members of the α/β hydrolase superfamily, with the β-sheet core enclosed by six α helices (α1, α2, α3, α6, α7 and α8). hMGL presents two additional helices (α4 and α5), which are part of the lid domain. The lid domain comprises residues 151 to 225, that is helices α4, α5 α6 and the loop connecting helices α4 to α5, and α5 to α6. Within this extended region, the helix α4 and the loop connecting α4 to α5 delineate a U-shaped channel, modelling the access to the catalytic site.

The available crystal structures also provide a clear picture of the architecture of hMGL active site, which comprises the catalytic triad S122, D239 and H269 (Figure 2 and 4). The active site is situated within the inner region of the β-core, with the catalytic serine being part of the GXSXG consensus motif, on a turn between α3 and β5, covered by the lid domain. The catalytic residues are oriented to maximize the nucleophilic character of S122, forming a hydrogen-bond network, which includes the negatively charged D239, the imidazole ring of H269 and the hydroxyl group of S122. In close proximity to the catalytic triad, the oxyanion hole, which comprises the NH groups of A51 and M123 backbone, stabilises the anionic transition state formed during the hydrolysis of 2-AG.

Furthermore, the crystal structures also elucidated the position of the cysteine residues that have been proven to be crucial for the enzymatic activity, providing information essential for the comprehension of their role in the MGL activity modulation. Going to details, C33 is located on β strand 2, on a superficial position of the β core far apart from the active site. C242 is in close contact with the catalytic triad, located only 4 Å away from S122[104].

C201 is situated on the loop between helices α5 and α6, within the lid domain; while the C201 side chain is oriented towards the solvent, the backbone is also accessible from the

hydrophilic cleft of the active site. On the other hand, C208 is placed at the top of helix α6, with the thiol group completely pointing towards the cytosol, farther away from the active site.

An additional characteristic highlighted by the crystal structures is the presence of an opening of 5 Å connecting the active site and the cytosolic environment outside the enzyme. This small opening is delimited by a subset of lid domain residues, namely P178, S181, L184, T194, Q195, R202 and A203 (Figure 2), situated on the loops connecting α4 to α5 and α5 to α6. Interestingly, in the crystal structure 3HJU, a glycerol molecule, used as cryoprotectant during the processing procedures, has been co-crystallised with the enzyme and is placed within the binding site pointing towards the opening[104]. These evidences suggest that the aperture may provide an exit path for the glycerol after the hydrolytic decativation of 2-AG.

### *2.2.2 Architecture of hMGL binding site*

The determination of different crystal structures of hMGL without any ligand binding the active cavity, and in presence of specific inhibitors, helped to elucidate the structure of substrate-binding site, providing fundamental information for the rational drug design. The catalytic triad is placed at the bottom of a tight hydrophobic channel. The side chains of residues L148, A164, L176, I179, L205, V207, I211, L213, L214, V217 and L241 line the cavity that is thought to accommodate the lipophilic tail of 2-AG, while helices α4 and α5 delimit the U-shaped entrance of this channel (Figure 2). Notably, in the X-ray structure 3JW8[105], the lipophilic tunnel is in part filled with residual molecules of 2-methyl-pentane-2,4-diol (MPD), which is necessary during the crystal growth process. According to the authors, the presence of MPD molecules inserted in the lipophilic tunnel suggests that the endogenous substrate could be extracted from the membrane, and accommodate with the glycerol head pointing towards the catalytic triad. At the lower end of the channel, in close proximity to the active site, the environment of the binding cavity is more hydrophilic. The imidazolic nitrogen atoms of H121 and H272, the guanidinium group of R57 and the negatively charged E53 delimit a tight polar cavity that in the crystal structure 3HJU is filled with a residual molecule of glycerol (Figure 2).

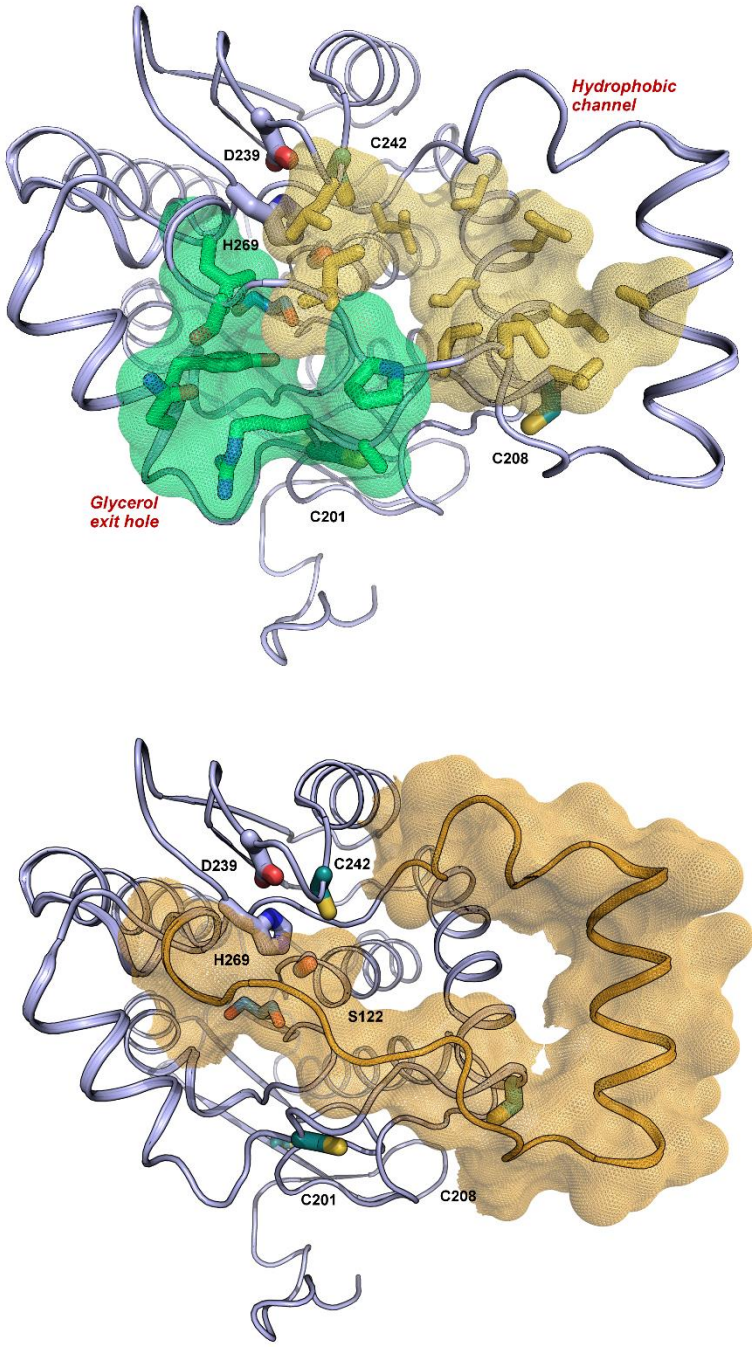


*Figure 2 Crystal structure of hMGL (PDB 3HJU). Upper panel: the active site residues (S122, H269, and D239) are represented with light-blue carbons; regulatory cysteines (C201, C208, C242) are depicted in dark green. The putative glycerol exit hole (light-green surface) is in close contact with the catalytic site. The residues lining the hydrophobic channel of the active site are coloured in yellow. Lower panel: the U-shaped access to the catalytic site delimited by the lid domain is represented in orange. A glycerol molecule co-crystallised with the protein is coloured with blue carbons.*

The existence of an alcohol-binding pocket situated between the active site and the postulated exit route for glycerol strongly suggests that it may bind the polar head of 2-AG, stabilizing its binding mode during the cleavage reaction.

Further information has been obtained from the analysis of the crystal structure of hMGL inhibited by active site-directed ligands. Presently, the crystal structures of hMGL covalently bound with two distinct carbamate-based inhibitors (PDB: 3JWE[105] and 4UUQ[106]), and of hMGL in complex with a reversible inhibitor (PDB: 3PE6) are available[107].

3JWE is the crystal structure of hMGL with the carbamate-based inhibitor SAR629[108] (Figure 3), which irreversibly blocks MGL by making a stable adduct with the catalytic residue S132 (S122 in 3HJU). In accordance to what observed for the unbound enzyme, 3JWE has two proteins per asymmetric unit, with the monomers oriented in a specular way. The covalent inhibitor adopts in each monomer the same conformation. In spite of these similarities, however, the electron density of helix α4 of monomer A has not been determined, while the same region adopts a stable conformation in monomer B. Moreover, a second molecule of SAR629 has been co-crystallised with the enzyme, and occupies the upper part of the active site access. While the second molecule of SAR629 is not involved in the molecular mechanism leading to inactivation of the enzyme, its presence may have had a role in the stabilisation of α4 conformation, which corresponds to that observed in the unbound form of hMGL obtained in the same conditions[105]. SAR629 is characterised by a symmetric moiety that consists of two specular fluorophenyl rings. This portion adopts a Y-shaped conformation and occupies the lower part of the lipophilic tunnel, with one of the fluorophenyl rings fitting a hydrophobic pocket delimited by L158, L223 and L224 (L148, L213 and L214 in 3HJU), and the second aromatic branch in contact with L186, L189 and L215 (L176, L179 and L205 in 3HJU).

A second crystal structure of hMGL covalently bound to a carbamate inhibitor has been recently determined (PDB: 4UUQ)[106]. Similarly to what observed for the complex hMGL-SAR629, the crystal of the complex hMGL-SAR127303 consists of two specular monomers. Contrary to SAR629, SAR127303 does not have a symmetric, Y-shaped structure (Figure 3), and the inhibitor adopts different binding modes in the two monomers,

which in turn present a different arrangement of the lid domain portion in contact with the inhibitor molecules. Specifically, 4UUQ differs from the previously reported X-ray structures in a small region of the lid domain, limited to the loop between helix α4 and β strand 6. Going to details, this rearrangement determines a reduction of the aperture of the lid domain, which thus makes a different network of interactions with the sulfonyl group of the inhibitor molecule.

Finally, a further crystal structure of hMGL in complex with a non-covalent reversible inhibitor has been determined (PDB: 3PE6)[107]. Contrary to what has been reported for the other available X-ray structures, 3PE6 was crystallised without the addition of surfactants or detergents through the mutation of L36, L169 and L176 in alanine, serine and serine, respectively, in order to obtain a more soluble form of the enzyme. Notably, these residues are placed on the β core (L36) and on the lid domain (L169 and L176).

As revealed by the crystal structure, the inhibitor ZYH occupies almost the entire binding pocket, placing the 3-(4-(pyrimidin-2-yl)piperazin-1-yl)azetidinyl moiety (Figure 3) in the alcohol-binding pocket described above, and the 2-cyclohexylbenzoxazol-6-yl in the lipophilic tunnel, extending approximately in the same region occupied by the covalent inhibitors SAR127303 and SAR629. The main characteristic unveiled by this crystal structure, however, is a substantial conformational modification involving the helix α4 of the lid domain.

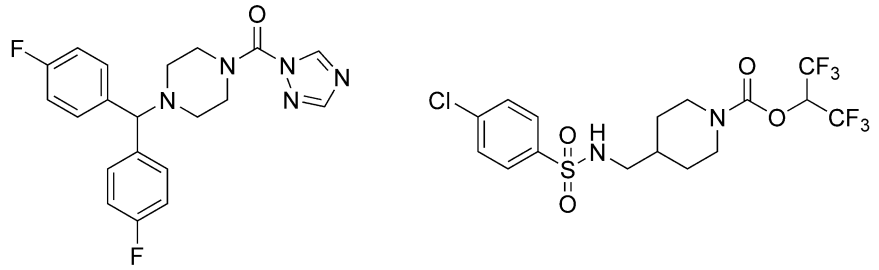

SAR 629



SAR127303

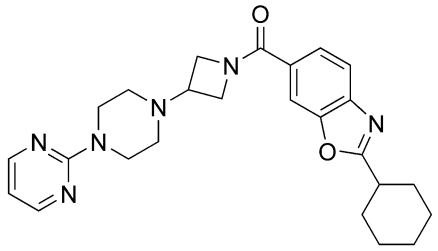

ZYH

*Figure 3 Chemical structure of MGL inhibitors co-crystallised with the human enzyme.*

### *2.2.3 Structure and functions of the lid domain*

As already mentioned, the lid domain is a region composed by a series of helices interconnected that enclose the β core region and, at the same time, shape the entrance to the catalytic site, covering it and reducing its exposure to the solvent. The lid domain structure is a common feature shared by many lipases, members of the α/β hydrolase superfamily, including human pancreatic and gastric lipase. Going to details, lipases are known to be hydrolases, whose catalysis is activated at the interface between aqueous and lipid-substrate phase. The interaction between the catalytic site and the interface is mediated by the lid domain, which serves as a lipid gate for the substrate to the active site. This phenomenon, also known as "interfacial activation", has been widely investigated for this class of hydrolases[109–111], and allow the lipases to exist in equilibrium between two distinct

conformations –closed and open-, which correspond to a shielded or substrate-accessible active site.

In most lipases, the inner wall of the lid domain is hydrophobic; upon the opening event, this apolar surface is exposed, leading to an increase of the solvent-accessible surface area. For this reason, the closed conformation of lid domain lipases is likely to be predominant in water, while the open conformation should be stabilised by the interaction with a membrane or, at least, in presence of organic solvents. Furthermore, it has been postulated that in lipases characterised by a simple lid domain, consisting of only one helix, the transtition from the open to the closed conformation takes place through a rigid body movement. In contrast, in lipases with a complex lid domain, a more complex conformational rearrangement is thought to be involved in the opening mechanism, which thus might be a limiting step from a kinetic point of view.

In hMGL, the lid domain consists of residues 151 to 225, although other authors identify it with a more restricted region, limited to the helix α4 and to the loop connecting helices α4 to α5, which define the U-shaped funnel preceding the active site cleft. As revealed by the available crystal structures, the helix α4 consists of residues 157-170, although in 3PE6 the structure of this helix also includes residues 153-157, probably as a consequence of the ligand-induced conformational rearrangements. Helix α4 is characterised by a marked lipophilic character, being composed of hydrophobic residues that orient their side chain outside the access channel. The helix α4 residues and those that form the loop between α4 and α5 (L174, L176 and L179) thus delineate a hydrophobic region at MGL surface. Interestingly, the lid domain of MGL is characterised by a more marked lipophilic nature compared to that of other lipases of the α/β hydrolases superfamily. This observation is consistent with experimental data showing that the enzyme is present both in the cytosol and in the membrane fraction of Cos-7 cells. MGL thus might act as an amphitropic protein, soluble in the cytosol, and able at the same time to interact with the membrane and to extract from it the lipophilic substrate[104]. This model, that has been proposed to explain the double nature of MGL, is supported by the analysis of the amino acid sequence of helix α4 and of its three-dimensional structure. The helix α4 in fact presents a series of hydrophobic residues oriented outside the channel of the active site, which may serve to anchor the enzyme to the membrane (Figure 5); besides, three more hydrophilic residues (Q152, E154

and K160) might mediate the interaction with the polar head of 2-AG, and thus play a role in the recognition process. Finally, the positively charged side chain of K160 could make polar interactions with the phosphate heads of the membrane phospholipids.

As already mentioned, distinct crystal structure of hMGL show remarkable conformational difference circumscribed to the lid domain, and more specifically to the residues of helix α4 and of the loop between α4 and α5, suggesting that, as in other lipases, the lid domain is affected by high conformational variability. The crystal structures of the unbound form of hMGL 3HJU and 3JW8 show the enzyme in its open conformation; on the other hand, the experimental procedures applied to obtain the crystallisation of the protein may have affected the architecture of the lid domain. The open-lid domain conformation of 3HJU might had been stabilised by the addition of detergents used in the purification protocol[104], while the use of a crystal soaking adjuvant such as MDP might have played role in the stabilisation of helix α4. As a proof of the lid domain structural flexibility, the helix α4 of monomer B in 3HJU is poorly defined, while the same region has not been determined in the first crystal structure of hMGL in complex with a covalent inhibitor. In the recently solved structure 4UUQ, the lid domain adopts different conformations in the two molecules found in the asymmetric unit, although the structural dissimilarities are limited to a small number of residues of the loop connecting β strand 6 to helix α4, and the aperture of the active site channel appears reduced in its extent. Finally, the crystal structure of hMGL in complex with a non-covalent inhibitor (3PE6) shows a remarkable difference in the lid domain, due to a rolling movement of helix α4 over the binding site (Figure 4). The authors described the new rearrangement of the lid domain as a closed conformation, compared to the widely open U-shaped channel observed in 3HJU. The alteration of the lid domain structure also reflects a change in the hydrophobic properties of this region. Notably, while the enzyme in its open conformation exhibits a set of hydrophobic residues, pointing outside the active site channel, the helix α4 of 3PE6 is characterised by a reduced hydrophobic profile, with the apolar residues turned towards the inner of the tunnel, and a set of hydrophilic residues facing the solvent.

The analysis of different structures determined through X-ray experiments led to the hypothesis that the hydrophobic nature of the lid domain may promote its interaction with the membrane, in order to allow the engagement of 2-AG. According to the proposed model,

after the substrate recruitment the helix α4 would roll over the binding site, closing the access to the active site, while the enzyme would dissociates from the membrane while cleaving 2-AG. Following the substrate hydrolysis, MGL might re-assume the open conformation and associate again to the membrane to reinstate the catalytically active state. The catalytic cycle appears thus to be strictly correlated to the reversible conformational modifications of the lid domain.

Very recently, fundamental NMR data have been reported providing evidences for the existence of an equilibrium between an active and an inactive form of hMGL in solution[112]. In the study reported by Tyukhtenko and colleagues, the enzyme hydrogen-bonding network has been taken into account as a determinant of the overall protein structure. The experimental results show that specific perturbations, such as pH or temperature variations and point mutations, are able to determine, in a predictable manner, significant changes in the downfield region of hMGL NMR spectra. Notably, the alteration observed in the hydrogen-bonding network are also related to the ability of the enzyme to engage a site-directed probe, paraoxon. The inability of the small ligand to access the active site has been related to a shift of the equilibrium in favour of the closed-lid domain conformation. These lines of evidence further confirm that hMGL activity can be finely modulated by controlling the events involved in the maintenance of the equilibrium between different lid domain conformations.

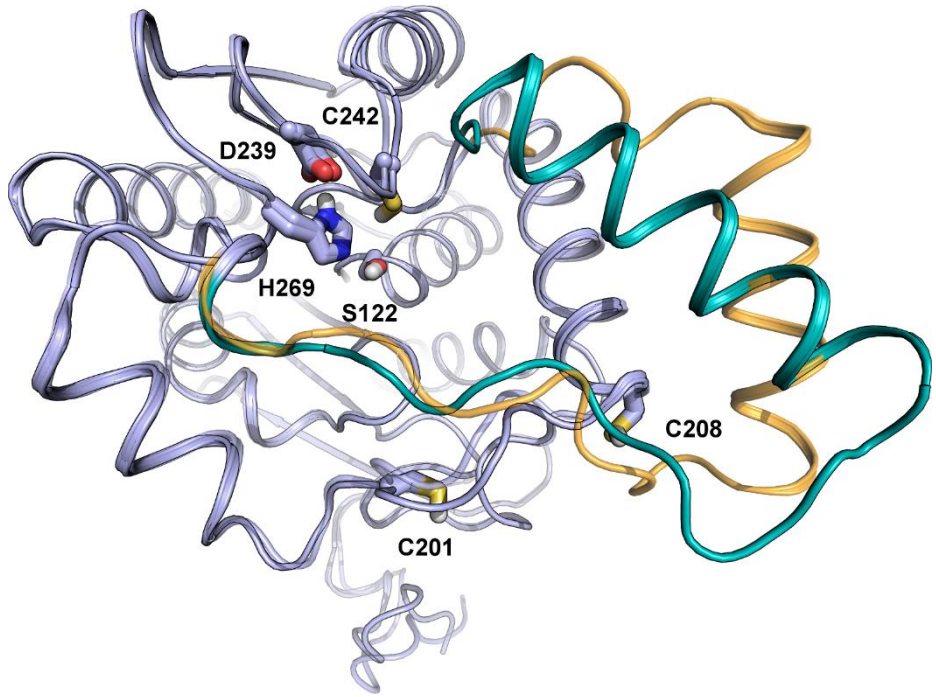


*Figure 4 Superposition of hMGL-crystallised structures; regulatory cysteines and the catalytic triad residues are shown as sticks. The open lid domain (PDB 3HJU) is coloured in orange; the lid domain in its closed conformation is represented in dark green.*

Recently, experimental data have provided evidences showing that the interaction between hMGL and models of biological membranes determines a transition from a solution form of the enzyme to a membrane-associated one, involving major conformational rearrangements limited to the lid domain[113]. Following the model of the interfacial activation observed in other lipases, the modifications induced by the interaction with the phospholipid bilayer might stabilise the open conformation of hMGL and promote the substrate recognition and deactivation. Notably, the interaction of hMGL with POPC (1-palmitoyl-2-oleoyl-*sn*-glycero-3-phosphocholine)/POPG(1-palmitoyl-2-oleoyl-*sn*-glycero-3-phosphoglycerol) nanodiscs is sufficient to improve by ≈2.5-fold the enzyme apparent affinity ($K_m$), and by 3-fold the enzyme apparent rate of hydrolysis ($V_{max}$). Furthermore, HDX mass spectrometry experiments proved that the presence of nanodisc bilayer suppresses the deuteration of the enzyme in a region circumscribed to the helices α4 and α6 of the lid domain. The experimental results are supported by molecular dynamics (MD) simulations of hMGL interacting with a model of membrane showing a conformational

modification of the lid domain resulting in an increased opening of the active site channel. Taken together, all these results provide solid evidences of the flexibility and of the amphitropic nature of hMGL lid domain that, similarly to what has been observed for other lipases, serves as a flexible gate keeper for the substrate recruitment.

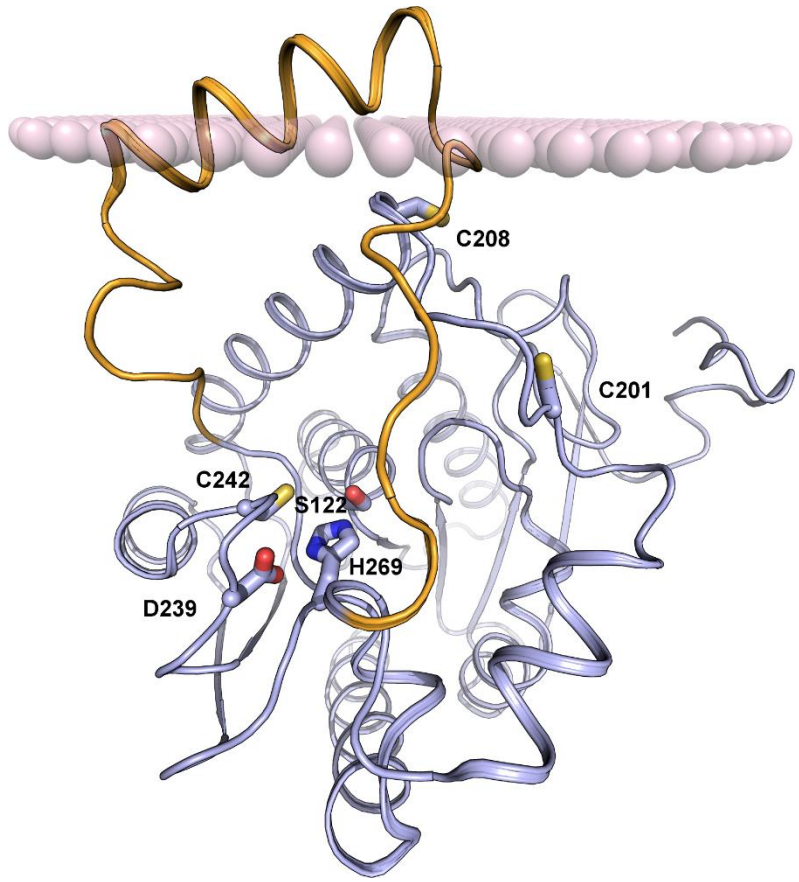


*Figure 5 Crystal structure of hMGL with the lid domain in open conformation (PDB 3HJU) represented in light blue cartoon. A portion of the lid domain delimiting the access to the catalytic site is depicted in orange. The catalytic triad and the regulatory cysteine residues are represented in sticks. The membrane profile is represented with spheres.*

### *2.2.4 Role of allosteric cysteine residues in MGL activity regulation*

A major feature of MGL is the presence of three cysteine residues that exert a fine control on the enzyme activity. While C242 is situated in close contact with the catalytic triad, and has been shown to have a role in the substrate recognition processes, two other cysteine

residues, C201 and C208 are located far apart from the active site, in a solvent exposed region within the lid domain structure (Figure 4 and 5). Evidences showing that maleimide-based compounds and other cysteine-reacting compounds are able to modulate MGL activity raised the interest about the possibility to target the regulatory cysteine residues to interfere with the hydrolytic deactivation of 2-AG.

Notably, a class of isothiazolinone-based compounds has been found to target selectively C201 and C208, giving a partially reversible inhibition of the enzyme through the formation of a reducible disulfide adduct. On the other hand, this result evokes the hypothesis that C201 and C208 might function as MGL activity regulator by converting a change in the environment redox state into a "turn off" signal for the enzyme.

The controlled production and release of reactive oxygen species (ROS) is a key event in the regulation of several physiological signalling processes[114,115], and cysteine residues appear to be a privileged target for modulators, such as hydrogen peroxide ($H_2O_2$), in order to transmit the signal[116–118]. Notably, in many biological systems, the transient transformation of cysteine thiol groups, leading to reversibly oxidised forms such as sulfenic acid and sulfenamide, represents an event that modulates the enzymatic activity of the target and, at the same time, protects it from further irreversible oxydation[119–124]. Interestingly, $H_2O_2$ levels are enhanced by the activation of ionotropic glutamate receptors[115], and given the strict relationship existing between the regulation of glutamate concentration and the modulation of the ECB system, it has been hypothesised that oxidative stimuli may act as a trigger sufficient to modulate MGL activity through the sulfenylation of the regulatory cysteines 201 and 208[125].

Notably, the exposition of rat MGL to increasing concentrations of $H_2O_2$ determines rapid and non-competitive of the enzyme activity, which is completely reinstated by enzyme dilution, while even high concentrations of $H_2O_2$ do not affect DGL-α activity. Single point mutations also showed that rMGL sensitivity to $H_2O_2$ is mediated by C201 and C208. Interestingly the double mutation of C201 and C208 determines an even more remarkable reduction of $H_2O_2$ potency, suggesting a cooperative interaction of the residues[103] and, on the other hand, ruling out the possibility that the MGL inhibition is mediated by the formation of a disulfide bond between C201 and C208. The identification of the covalent adduct between C201, and at a lower extent C208, and dimedone, which reacts selectively

with transient oxidised species, revealed that the $H_2O_2$-dependent inhibition of MGL is mediated by the formation of sulfenic acid[103].

Taken together, these evidences outline the role of MGL as a redox state-sensor, able to promote the $CB_1$-mediated retrograde transmission by enhancing the levels of the neuroprotective endocannabinoid 2-AG. Furthermore, the existence of the oxidation-sensitive sites corresponding to the allosteric cysteines 201 and 208 requests a new deal of effort to the search of new ligands selectively, targeting this allosteric site, in order to obtain a finely tuned modulation of 2-AG levels.

### *2.2.5 MGL as pharmacological target: known inhibitors*

The pharmacological regulation of 2-AG represents, from a medicinal chemistry point of view, a goal of great importance, given the wide range of physiological and pathological mechanisms involving this neuromodulator. On the other hand, adverse effects related to the chronic inhibition of MGL, including functional antagonism of $CB_1$ receptors and the decrease of long-term potentiation of CA1 synaptic transmission, raise doubts about the convenience of using MGL inhibitors in pharmacological treatment and, at the same time, demand the identification of allosteric modulators, endowed with greater selectivity and fewer side effects.

*URB602 and derivatives*

The *N*-phenylcarbamate URB602 ($IC_{50}$=223 μM) was the first MGL selective inhibitor to be discovered[126]. In spite of its low potency, URB602 showes a great selectivity for MGL against FAAH *in vivo* and promotes $CB_1$ activation-dependent stress-induced analgesia[126], and mediates antinociceptive mechanisms in several pain models[127,128]. URB602 inhibits MGL in non-competitive and time-dependent way, through a partially reversible mechanism[129]. The enhancement of potency gained through the substitution of the carbamate portion with a ureidic group ($IC_{50}$=115 μM), which has a lower tendency to react with the S122 hydroxyl group, suggests that these compounds are non-site-directed inhibitors.

A series of scaffold modifications, including isosteric replacements, ring size and substitution, *para*-substitution of the biphenyl moiety and the incorporation of a bicyclic element, have been performed in order to enhance the potency of *N*-phenylcarbamate compounds, leading to the identification of a *p*-OH substituted derivative showing higher potency at inhibiting MGL[130].

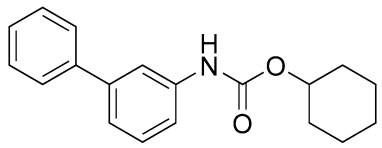


URB 602

*Figure 6 Chemical structure of URB602.*

## *JZL184 and site-directed inhibitors*

The piperidine-carbamate compound JZL184 was found through the application of competitive activity-based protein profiling (ABPP)[131]. JZL184 is characterised by high potency ($IC_{50}$= 8 nM) and irreversibly inhibits MGL through the formation of a stable covalent adduct with the catalytic serine 122[132], leading to the enhancement of 2-AG levels *in vivo*. While JZL184 shows a high selectivity for MGL over FAAH and other brain-located hydrolases, this compound also blocks carboxylesterases in peripheral tissues, shows inhibitory activity towards FAAH after chronic administration, and is characterised by low cross-species activity[132].

Furthermore, the chronic suppression of MGL due to repeated administration of JZL184 is related to desensitisation of $CB_1$ receptors, cross-tolerance to $CB_1$ receptor agonists, tolerance to the antinociceptive effects exerted by the compound and physical dependence[133]. These liabilities hamper the clinical usage of JZL184, limiting its application as a pharmacological probe of MGL activity. The class of 4-nitrophenyl derivatives, including JZL195[134], is characterised by a low selectivity among different hydrolases in general.

In order to develop selective MGL inhibitors with an improved cross-species profile, new classes of compounds, such as *O*-hexafluoroisopropylcarbamate[135,136] and *N*-hydroxysuccinimidyl[137] carbamate ligands have been studied. Among them, KML29[135] shows a complete selectivity for MGL over FAAH and other hydrolases at all doses, an improved cross-species activity, while maintaining good potency ($IC_{50}$=15nM). On the other hand, KML29 induces cannabimimetic side effects when administered *in vivo*[138].

More recently, another *O*-hexafluoroisopropylcarbamate derivative has been characterised; SAR127303[106] shares with KML29 the same leaving group and piperidine-carbamate functionality, and shows high selectivity for MGL over other hydrolases and an improved activity towards mouse and human MGL ($IC_{50}$=3.8 nM 29 nM, respectively). On the other hand, while SAR127303 exerts the typical effects related to the inhibition of MGL, it negatively affects memory and cognitive processes.

Selective inhibitors of MGL composed by a piperidine or piperazine ring with a putative serine-carbamoylating functionality include triazoleureas, such as JJKK-048[139], and *N*-hydroxysuccinimidyl carbamates, such as MJN110[137]. Other compounds with serine-reactive groups,such as tetrazolylureas and 1,3,4-oxadizol-3-ones had shown MGL-inhibitor activity, but these classes generally showed also inhibition of other serine hydrolases like FAAH[140,141]. Recently, a compound lacking reactive functionalities, CL6a has been described as a micromolar reversible inhibitor of MGL[142], addressing the catalytic pocket, similarly to what had been observed for the crystal structure with the non-covalent inhibitor ZYH[107], and a lipophilic ester[83] has been shown to inhibit MGL with sub-micromolar potency.

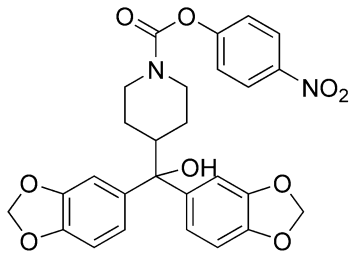


JZL184

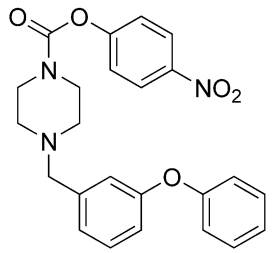


JZL195

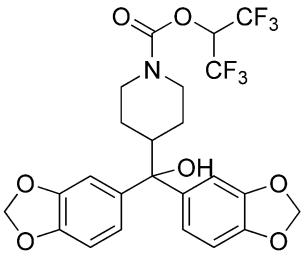


KML29

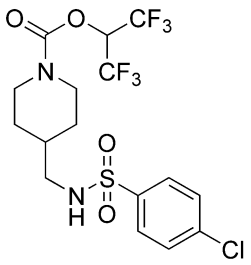


SAR127303

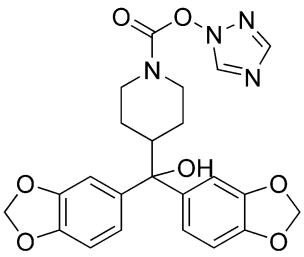


JJKK-048

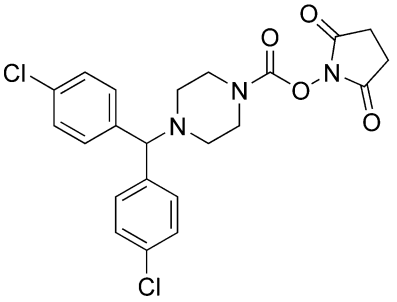


MJN110

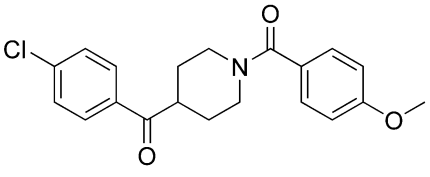


CL6a

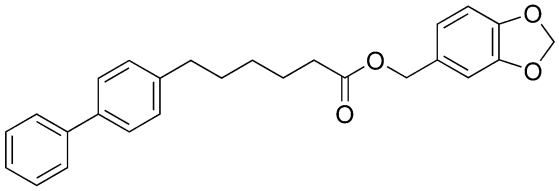


Comp21

*Figure 7 Chemical structures of MGL inhibitors targeting the catalytic pocket.*

*Cysteine-targeting compounds: N-substituted maleimides*

A broad series of *N*-substituted maleimides have been developed as potential MGL modulators, following the experimental evidences disclosing the existence of sulfhydryl sensitive sites playing a critical role in the enzyme activity regulation. A series of bulky-substituted *N*-maleimides showed high selectivity[101], suggesting that the inhibition of this class of compounds is mediated by the interaction with a cysteine residue characterised by hydrophobic surrounding-environment, such as C242, which is situated in close contact with the catalytic triad, placed at the bottom of the lipophilic active site access channel. Mass spectrometry data, corroborated by mutagenesis experiments and by molecular modelling studies revealed that the inhibition of MGL by the most potent compound in the series, *N*-arachidonoylmaleimide (NAM, $IC_{50}$=140 nM), is mediated by a Michael addition of the maleimide group to C201 and C208[99,100,102,143].

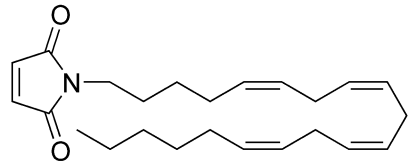


*N*-arachidonoylmaleimide (NAM)

*Figure 8 Chemical structure of NAM.*

*Cysteine-targeting compounds: disulfide compounds*

In order to further characterise the role of cysteine residues in the regulation of MGL activity, a series of disulfide compounds have been developed. Notably, disulfiram (dicyclopentamethylenthiuram disulfide, $IC_{50}$= 6.44±0.05μM), disulfiram derivatives and phenyl disulfide ($IC_{50}$= 5.79±0.05μM)[144]. According to the proposed mechanism, this class of compounds inhibit MGL through a redox process, involving the formation of a disulfide bond between the ligand and the targeted cysteine. According to this hypothesis, disulfiram derivatives inhibit hMGL by forming a mixed disulfide adduct with C208 and, at a lower extent, with C242[145]. Furthermore, results showing that the disulfide-dependent inhibition of MGL is restored by the application of the reducing agent dithiothreitol (DTT) support the hypothesis that the modulation of the redox state of critical allosteric cysteines is a promising and feasible alternative to the application of site-directed MGL inhibitors.

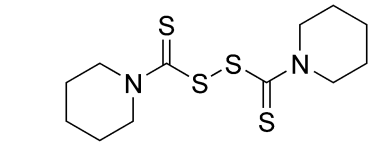


Dicyclopentamethylthiuram disulfide
(Disulfiram)

*Figure 9 Chemical structure of disulfiram.*

*Cysteine-targeting compounds: isothiazolone and benzisothiazolone derivatives*

Isothiazolone (ITZ) and benzisothiazolone (BTZ) based compounds have been recently found as potent cysteine-targeting MGL inhibitors. 2-octyl-4-isothiazol-3(2*H*)-one (octhilinone) shows a high potency towards rMGL ($IC_{50}$= 88±12nM), while the introduction of bulkier and more lipophilic substituents, such as the oleoyl group, enhances the inhibitory potency of these compounds ($IC_{50}$= 43±8nM)[146]. Notably, the substitution of the isothiazolone group with a benzisothiazolone functionality led to a potent inhibitor, providing evidences that the inhibitory mechanism of these compounds does not involve the formation of a Michael adduct. Moreover, the enzymatic activity is reinstated by the enzyme dilution, which is suggestive of a partially reversible mechanism; besides, the fact that DTT application is sufficient to reduce octhilinone potency without affecting MGL activity outlines that ITZ- and BTZ-based compounds block the enzyme through the formation of a mixed disulfide bond.

The mechanism of ITZ- and BTZ-mediated MGL modulation has been further characterised[147], showing that these compounds have higher inhibitory potency towards rMGL than hMGL, while they conserve high selectivity for MGL over other hydrolases, including FAAH. Finally, mutagenesis studies revealed that octhilinone and *N*-octylbenzisothiazolone show a marked selectivity for C208 and C201, respectively. Taken together, these results have increased the information about the regulatory allosteric cysteine residues 201 and 208, while revealing BTZ-based compounds as potential and promising MGL inhibitors.

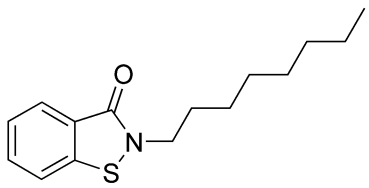


*N*-octylbenzisothiazolone

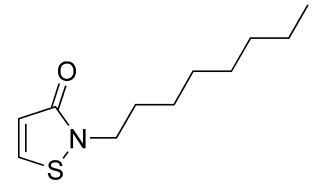


Octhilinone

*Figure 10 Chemical structures of ITZ- and BTZ-based compounds.*

*Cysteine-targeting compounds: natural terpenoids*

Two naturally occurring terpenoids, pristimerin and euphol, are characterised by high potency and selectivity toward MGL ($IC_{50}$= 93±8 nM and 315±1 nM, respectively)[148]; on the other hand, while pristimerin does not affect FAAH or NAAA (*N*-acylethanolamine acid amidase), it is also a potent inhibitor of a secondary 2-AG deactivating enzyme, ABHD6 ($IC_{50}$=98±8 nM. Pristimerin is a pentacyclic triterpenoid compound bearing a quinone-methide group. Despite the presence of a reactive group that could give covalent adducts with the cysteine thiol groups, rapid dilution assays revealed that pristimerin-mediated inhibition of MGL is a completely reversible event. Besides, it has been proven that pristimerin reduces the maximum catalytic activity of MGL, without affecting the Michaelis-Menten constant, and thus can be considered a rapid reversible and non-competitive inhibitor. Notably, euphol is characterised by similar stereo-chemical properties compared to pristimerin, while lacking the reactive quinone-methide functionality. Despite the lower potency, euphol presents an inhibitory kinetics that is equal to that of pristimerin. On the other hand, mutagenesis studies revealed that the mutation of C201 and C208 affects the activity of these compounds, although in different ways; C208G mutation indeed suppresses pristimerin-mediated effects, but does not reduce euphol potency, while C201G mutation decreases euphol potency without affecting pristimerin activity.

More recently, another natural terpenoid similar to pristimerin, β-amyrin[149], was found to block hMGL ($IC_{50}$= 2.8 μM); similarly to what has been observed for pristimerin, β-amyrin-mediated inhibition is based on a rapid, reversible non-competitive mechanism. Moreover, while β-amyrin does not condition the levels of AEA, the enhancement of 2-AG levels are attributable to a combined inactivation of MGL, ABHD6 and ABHD12.

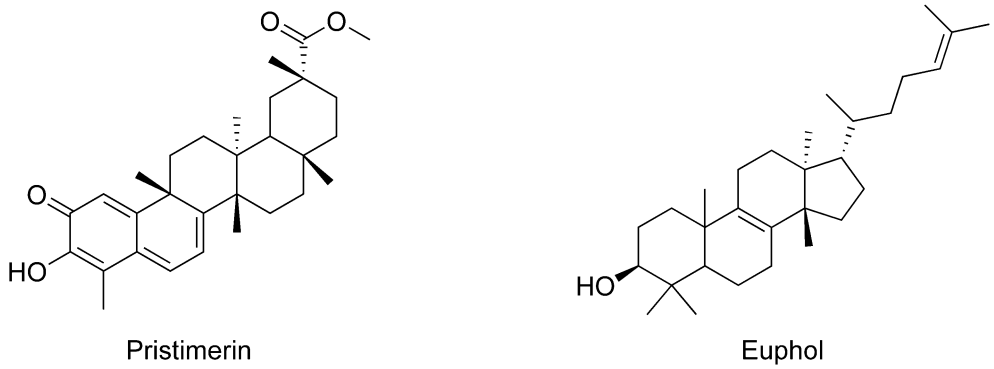


*Figure 11 Chemical structure of naturally occurring MGL inhibitors.*

## *2.3 Free-Energy studies unveil a possible mechanism for hydrogen peroxide-dependent MGL inhibition*

In the last few years a great deal of effort has been put into the investigation of the molecular and structural basis for the conformational flexibility of the lid domain, in order to understand to what extent this structural element is involved in the regulation of MGL activity. Experimental data, showing that the interaction between MGL and a model of nanodisc membrane is sufficient to improve the kinetics properties of the enzyme[113], strongly suggest that, similarly to other lipases, MGL undergoes the phenomenon of the "interfacial activation"[109–111]. The lid domain of this enzyme would thus act as a flexible lipid gate into the active site, playing a crucial and regulatory role during the catalytic cycle of the enzyme. On the other hand, the events triggering its opening and closing functions have not been elucidated yet.

The presence of two allosteric cysteine residues (C201 and C208) within the lid domain encourages the hypothesis that they may have a role in the complex mechanism regulating the lipid gate functionalities. Notably, these residues are situated in close contact with helix α4 and the loop connecting it to helix α5, which is the portion responsible for the interaction with the membrane and characterised by the highest conformational variability.

In an attempt to elucidate the effect of chemical modifications at C201 and C208 side chains on the conformational equilibrium of MGL and, specifically, of the lid domain, the recent experimental results on $H_2O_2$-mediated rMGL sulfenylation were considered. The experiments have found C201 and C208 to be the crucial trigger of oxidation-dependent MGL blockade. Nonetheless, while the action of $H_2O_2$ on C201 involves the formation of a stable sulfenic acid product, C208 appears to be less prone to the sulfenylation than C201, although mutagenesis data revealed that both cysteine residues are critical for MGL activity.

It was thus tempting to speculate the molecular basis for the C208 oxidation-dependent MGL inhibition. Interestingly, C208 and the following residue, F209, are placed at the tip of helix α6, in a conformation the geometry of which could allow a chemical reaction between the cysteine thiol group and the backbone nitrogen of F209, giving an internal sulfenamide. As reported in the literature, sulfenic acid intermediates can be detected as stable oxidised species, depending on the environment conditions. On the other hand, in

specific circumstances, which include the conformation of the residues, the backbone of neighbouring residues might react with the oxidised thiol group and give a sulfenamide, a reversible oxidised form of the cysteine residue protecting the protein from further and irreversible oxidative processes[119,121,150].

Starting from these evidences, it was hypothesised that the oxidation of C208 to sulfenic acid may be a transient event, rapidly leading to the formation of a reversible and unstable species involving C208 and F209. While no evidences of a sulfenamide product were observed in the mass spectrometry experiments performed on rMGL, this hypothesis provide a feasible explanation to the low tendency of C208 to react with dimedone as a stable sulfenic acid intermediate.

Notably, while the experimental data performed on rMGL have helped to elucidate the role of regulatory C201 and C208, our research group at the University of Parma has recently found that, similarly to the rat form of the enzyme, the human MGL is characterised by high sensitivity to hydrogen peroxide-mediated oxidative *stimuli*. In order to elucidate the role of C201 and C208 as redox-sensitive switcher of hMGL activity, a series of pharmacological assays using 2-oleoylglycerol (2-OG) as substrate, coupled to LC-MS, have been performed. A preliminary and important consideration resulted from the observation that hMGL, purchased by different suppliers, is spontaneously oxidised in the buffer sample, before any treatment. This condition is sufficient to give reduced enzymatic activity (Figure 12). The incubation of purchased hMGL with the reducing agent DTT reinstates completely the enzymatic activity, confirming its oxidised state. These evidences outline that the enzyme spontaneously undergoes a transient chemical modification, circumscribed to cysteine thiol groups, that is able to block the catalytic activity; this event, however, is completely reversible, and hMGL activity is restored by thiols-reacting reducing agents such as DTT.

The incubation of the re-activated enzyme with $H_2O_2$ determined a remarkable decrease of hMGL activity, which is reinstated by treatment with DTT. This suggests that the hMGL blockade exerted by $H_2O_2$ is mediated by the formation of a reversible form of oxidised cysteine thiol groups, i.e. the sulfenic acid. In order to test this hypothesis, dimedone was used to detect cysteine side chains oxidised to sulfenic acid after the exposure to hydrogen peroxide (Figure 12). Dimedone is widely used as a highly chemo-selective probe for

sulfenic acid; dimedone is a cyclic diketone, able to selectively react with sulfenic acid, yielding stable covalent adducts that are not cleaved by reducing agents such as DTT.

Interestingly, after incubation of hMGL with $H_2O_2$ in presence of dimedone, DTT could not restore enzyme activitiy, supporting the hypothesis that, as it has been observed for rMGL, the sulfenylation of cysteine residues is a key event in the hydrogen peroxide-mediated inhibition of hMGL.

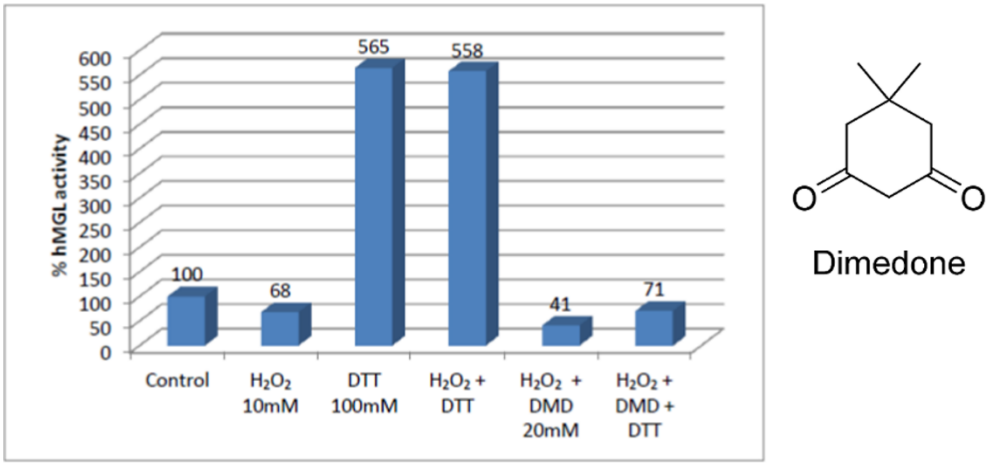


*Figure 12 Pharmacological assays revealed that hMGL in its initial conditions is not active (Control); the enzyme activity is restored by the action of DTT, which is able to reinstate the hMGL activity in presence $H_2O_2$. The incubation of hMGL with $H_2O_2$, dimedone (chemical structure on the right) and DTT revealed that $H_2O_2$ inhibits hMGL through the formation of sulfenic acid.*

In order to determine which cysteine residues are involved in the sulfenylation-mediated hMGL inhibition, mass spectrometry experiments on digested hMGL were performed. Notably, mass spectrometry data clearly showed that C201 is sensitive to hydrogen peroxide-dependent oxidation to sulfenic acid, which rapidly reacts with dimedone. It was not possible to detect the formation of an adduct between dimedone and oxidised C208 or C242. These data are consistent with the experimental results that have been recently presented on sulfenylation-mediated rMGL modulation[103].

Starting from these premises, the objective of this work was to investigate the effect of the oxidation of C201, C208, both C201 and C208 to sulfenic acid (as supported by biological data on both rat and human MGL), and to speculate the effect produced by the formation of

a sulfenyl amide at C208 on the conformational plasticity of hMGL. To this aim, unbiased MD simulations have been coupled to enhanced sampling methods, including Metadynamics and different implementation of this technique. At the same time, the effect of the presence of a model of phospholipid bilayer was investigated.

### *2.3.1 hMGL lives in its closed conformation in water*

#### *Molecular dynamics simulations of hMGL models in water*

The dynamics of hMGL in its opened-lid domain conformation (PDB: 3HJU), and of different models of hMGL with different modifications at C201 and C208 side chains were investigated. Going to details, three sets of six Molecular Dynamics simulations of native hMGL, of a model of the enzyme with C201 oxidised to sulfenic acid, and of hMGL modelled with C208 engaged in a sulfenyl amide adduct with F209 backbone were performed. Each simulation was carried out for 60 ns, using water as explicit solvent. The α/β core of the protein, including the active site region, was characterised by a dynamical stability in all the three sets of MD simulations, as revealed by the analysis of root mean square deviation (RMSD) and root mean square fluctuation (RMSF) of the backbone, suggesting that the perturbation of the chemical state of C201 or C208 has no influence on the architecture of the active site (Figure 13). On the other hand, the lid domain showed in each set of MD simulations a higher degree of flexibility. Notably, the largest fluctuations observed were limited to the helix α4 and to the residues of the loop connecting it to helix α5 (loop 4/5) and, eventually, consisted in an approaching movement of the lid domain rims, leading to the closure of the gate over the active site access.

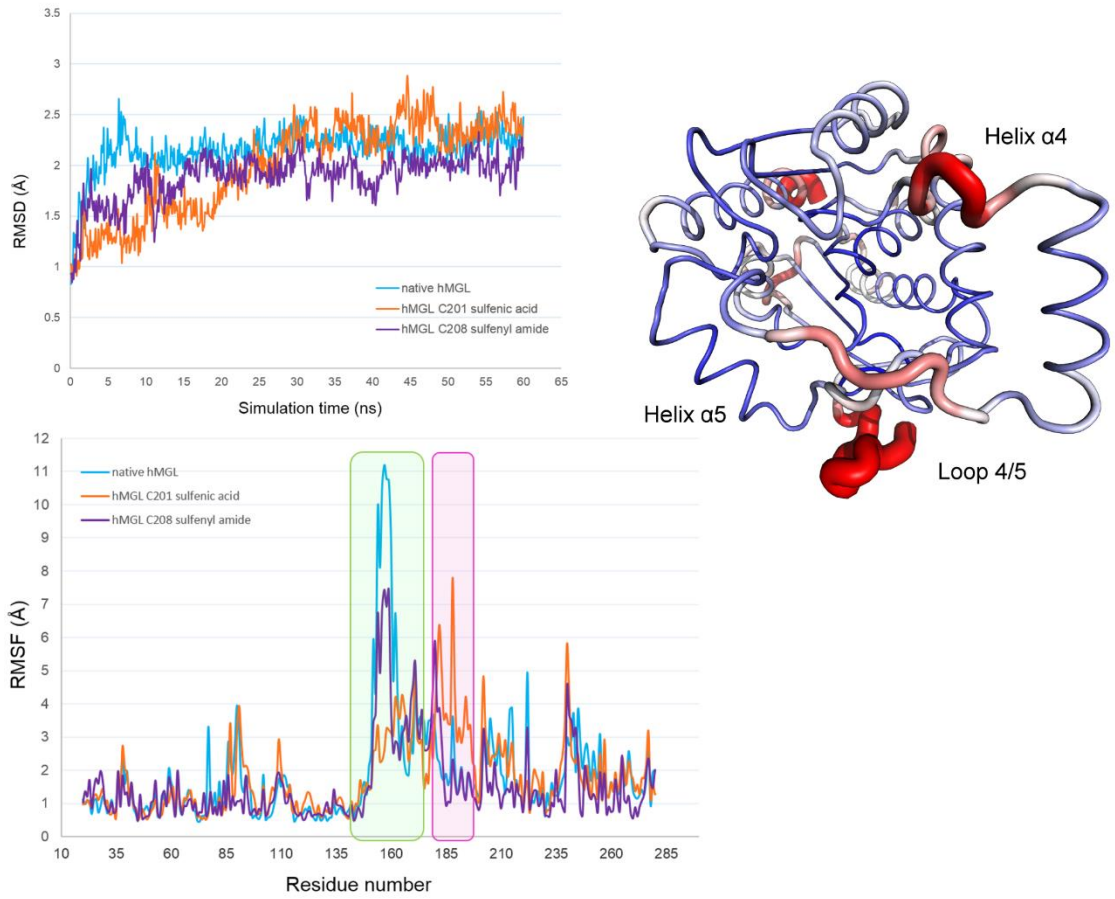


*Figure 13 Analysis of the RMSD (upper graph on the left) and of the RMSF (lower graph on the left) of three representative MD simulations of native hMGL, hMGL modelled with C201 mutated to sulfenic acid and hMGL modelled with C208 involved in an internal sulfenamide with F209. The α/β core of the protein is characterised by a dynamical stability, while residues of the helix α4 (highlighted in green) and of loop 4/5 (highlighted in pink) are characterised by a higher degree of flexibility. These results confirm the predicted high mobility of the lid domain region (beta-factor representation of hMGL on the right).*

In order to get more detailed information about this event, the lid domain fluctuations were analysed by considering the variation of the distances between the centres of mass of α carbons (Cα) of the residues on the loop 4/5 (i.e., residues 176-179) and on helix α4 (i.e., residues 150-157 and residues 158-164), measured throughout all the simulation time (Figure 14: native hMGL; Figure 15: hMGL modelled with C201 mutated to sulfenic acid; Figure 16: hMGL modelled with C208 mutated to a sulfenamide). Notably, the lid domain-closing event was observed with a variable frequency, depending on the hMGL model considered. Going to details, for the native hMGL MD simulations set, the lid domain was

characterised by a pronounced flexibility in all the simulations carried out and, in two cases out of six, the complete closure of the active site access was observed. In two other simulations, the distances between the reference points set within the lid domain increased, suggesting that the rims of the active site access spontaneously undergoes a breathing movement. Conversely, within the set of MD simulations of hMGL with C201 mutated to sulfenic acid, in four simulations out of six the complete closure of the lid domain was observed, while only one out of six simulations of hMGL modelled with the sulfenyl amide modification did not show the closing movement. According to these results, hMGL lid domain flexibly spans from an open conformation to a closed one, consistently with the crystallographic data reporting several structures characterised by different rearrangements of the active site access channel. On the other hand, while the MD simulations suggested that chemical modifications of the regulatory cysteine residues 201 and 208 favour the lid domain closure, at least a probabilistic level, they do not provide information about the free energy changes involved in the process. Furthermore, the results that have been collected must be integrated with the experimental evidences showing that MGL might be affected, as other lipases by the "interfacial activation" phenomenon. It is reasonable to assume that, while open when in contact with the substrate-containing membrane, MGL would spontaneously tend to assume a closed conformation in water in order to shield the active site in a polar environment.

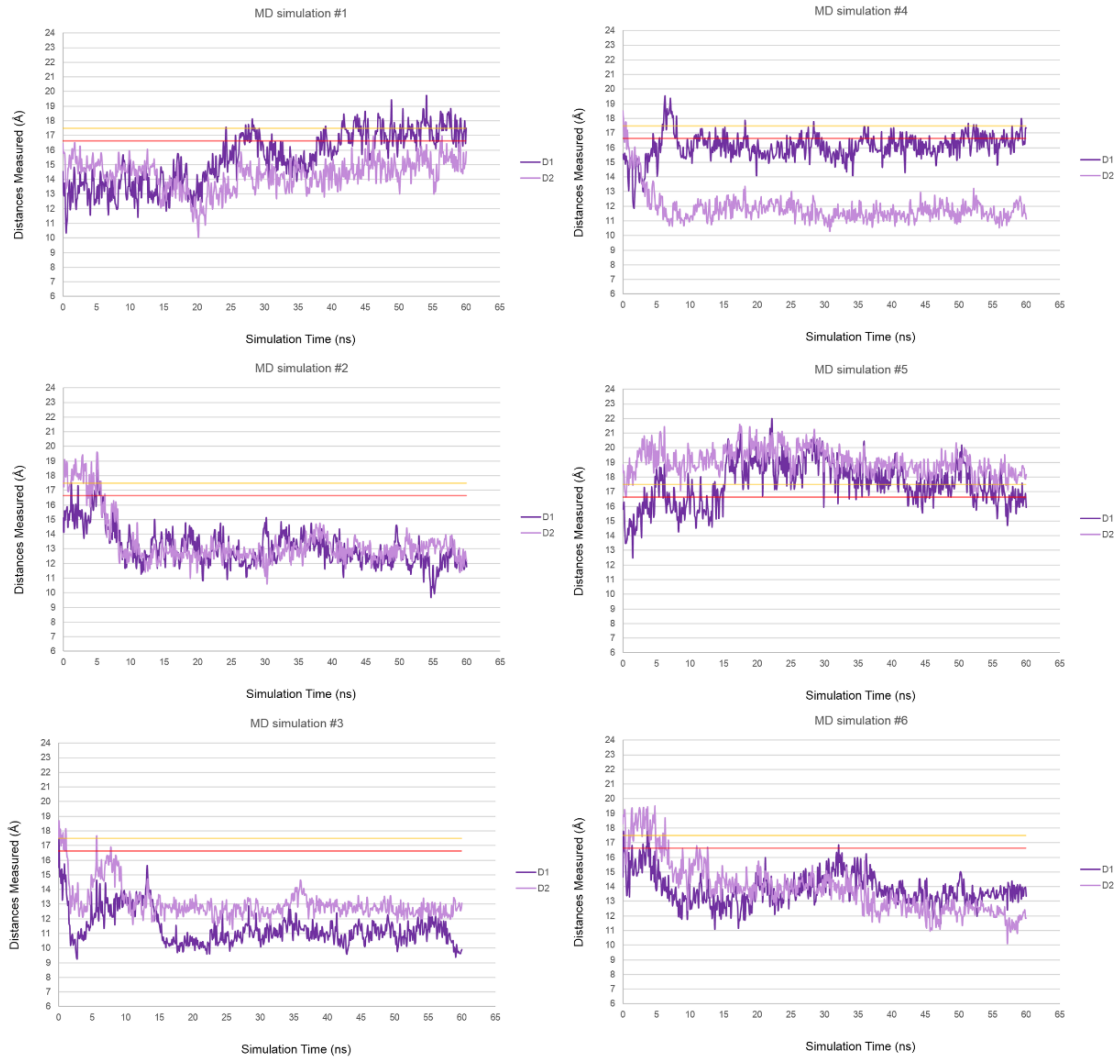


*Figure 14 Evaluation of the distances between fixed point on the lid domain throughout six MD simulations of native hMGL. The value of the distances in the crystal structure are reported as a reference (D1 red line, D2 orange line). In two simulations out of six (#1 and #5), the lid domain tends to assume a more opened conformation. In two simulations out of six (#3 and #4) a reduction of D1 and D2 values was observed.*

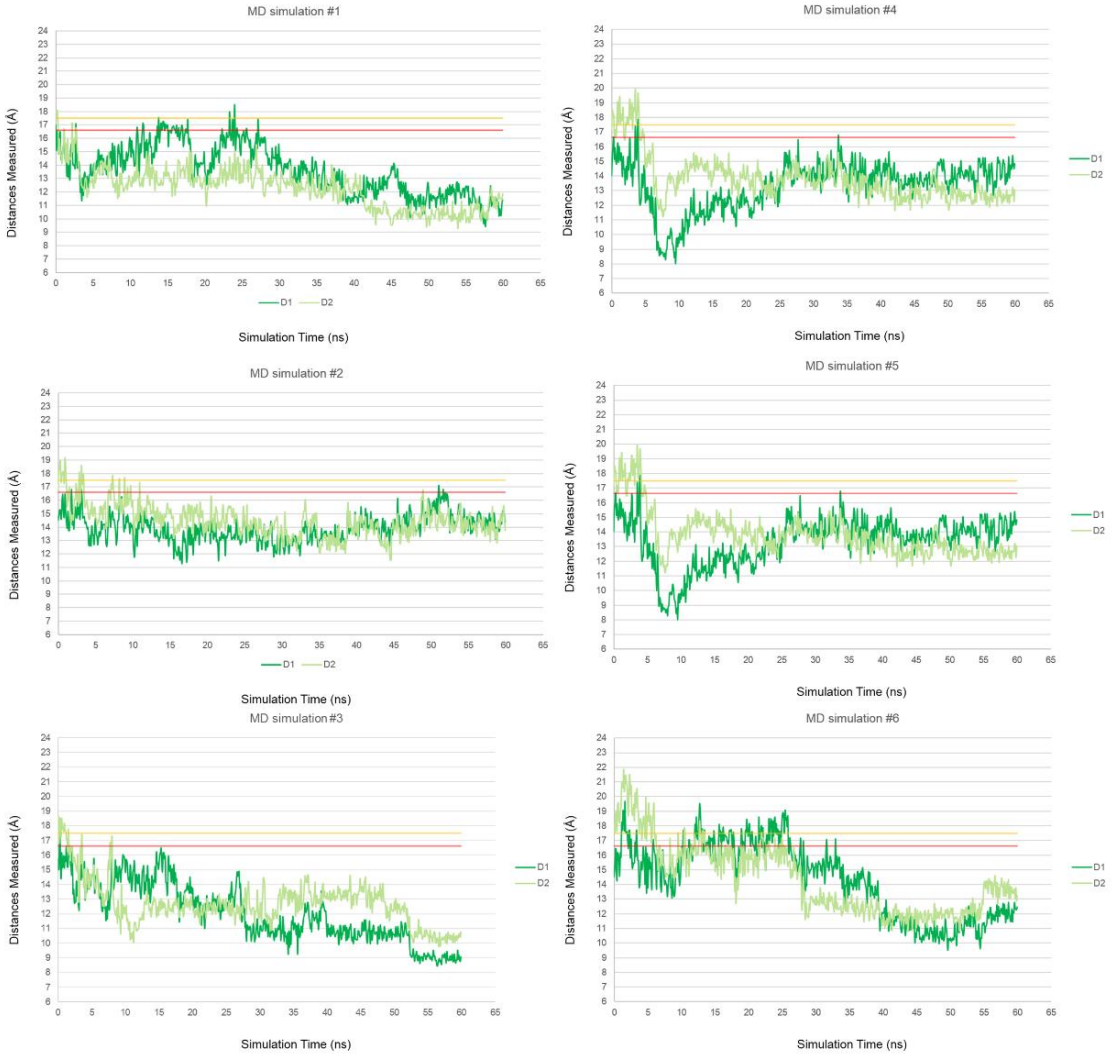


*Figure 15 Evaluation of the distances between fixed point on the lid domain throughout six MD simulations of hMGL modeled with C201 oxidized to sulfenic acid. The value of the distances in the crystal structure are reported as a reference (D1 red line, D2 orange line).*

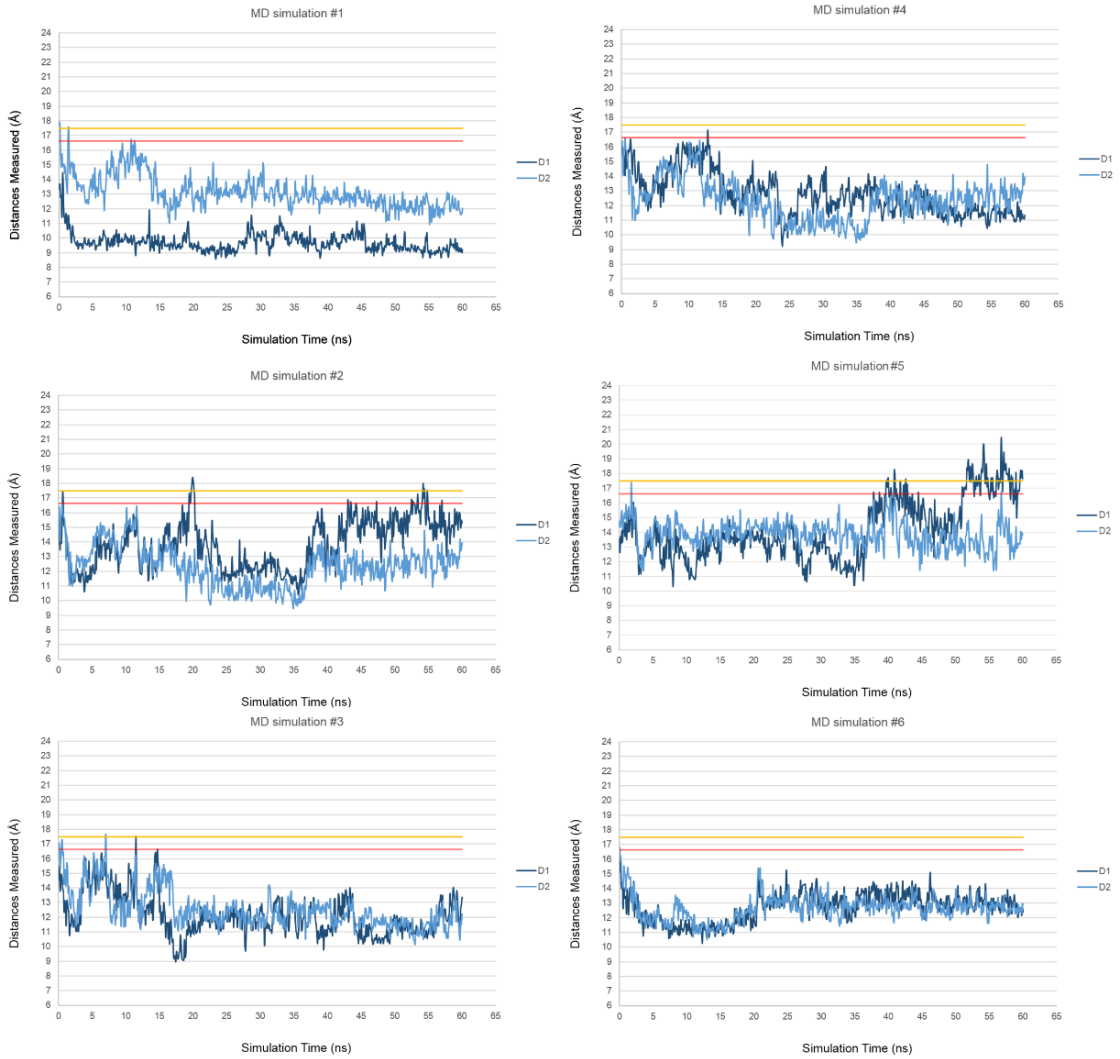


*Figure 16 Evaluation of the distances between fixed points on the lid domain throughout six MD simulations of hMGL modeled with C208 oxidized to sulfenyl amide. The value of the distances in the crystal structure are reported as a reference (D1 red line, D2 orange line).*

## *Free energy studies of native hMGL in water*

In order to further investigate the lid domain motion and the high flexibility that affects the conformational space of hMGL, free-energy studies were performed, by applying the well-tempered Metadynamics (WT Metadynamics) approach[151,152]. The Collective Variables (CVs), required to represent the conformational space of the system, were chosen in order to describe the helix α4 and loop 4/5 closure observed in plain MD simulations studies. In

order to define a set of appropriate CVs, suitable to reproduce the lid domain-closing event, the analysis of the distances between fixed points on the lid domain was considered. Two distances (D1 and D2) have been thus selected as CVs; the CV1 (D1) is the distance between the centre of mass of Cα of residues 176-179, situated on loop 4/5, and the centre of mass of Cα of residues 150-157, which include a portion of the loop preceding of helix α4. The CV2 (D2) is the distance between the centre of mass of residues 158-164, forming the initial segment of helix α4, and the same point on loop 4/5 used to define CV1 (Figure 17). In order to set a valuable parameter to discriminate between open and closed conformations, the CVs values, corresponding to D1 and D2 measured from the plain MD simulations trajectories described above, were chosen as a reference. Specifically, lower CVs values indicate a reduction in the distance between the lid domain rims, and thus indicate the closure of the active site access channel.

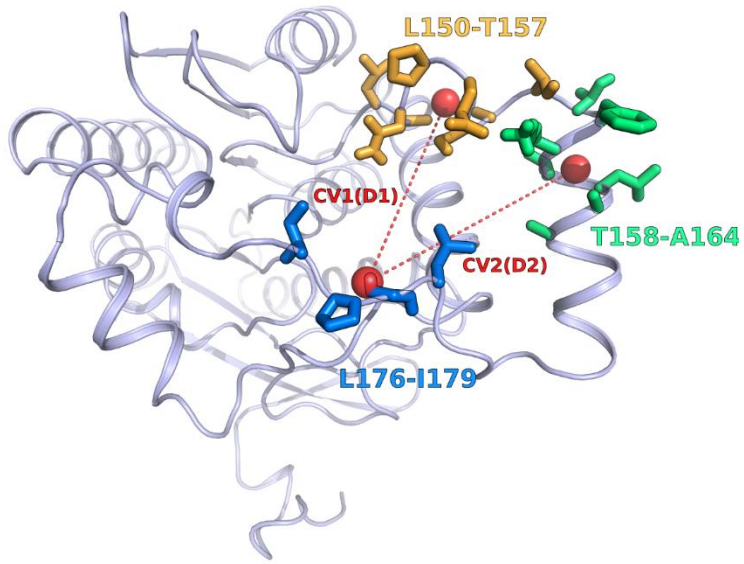


*Figure 17 The distances between the centre of mass of selected residues Cα on the lid domain rims were used as Collective Variables (CVs) (Distance 1 –D1, and Distance 2 –D2; represented with red dashes and spheres). CV1 and CV2 describe the lid domain motions observed in MD simulations involving loop 4/5 (residues 176-179, cyan spheres) and helix α4 (residues 150-157, orange spheres; residues 158-164, green spheres).*

The free-energy surface (FES) profile obtained clearly showed the presence of a free energy minimum corresponding to a closed conformation, as a consequence of the reduction of the distance between the rims of the lid domain along CV1 and, at a lower extent, CV2. Notably, as revealed by the FES, it was not possible to identify an energy well corresponding to the opened-lid domain rearrangement, corresponding to the initial conformation assumed by the enzyme, obtained from the crystal structure 3HJU. These results, together with the observations from the MD studies, are in accordance with the process of the interfacial activation. In this perspective, the hydrophobic character of MGL lid domain might have influenced the exploration of the enzyme conformational space in a polar environment. In fact, the crystal structure that has been used as hMGL model in this study was obtained in presence of surfactants, which might have influenced the rearrangement of the lid domain, promoting its open conformation. Taken together, these evidences suggest a possible explanation for the absence of a free-energy minimum corresponding to the crystallographic conformation.

### *2.3.2 The membrane opens the lipid gate of hMGL*

In order to evaluate the effect of the interaction between the cellular membrane and the lid domain on the conformational plasticity of this region, WT Metadynamics studies of native hMGL in presence of a POPC model were performed. The CVs adopted were the same used in the free-energy studies on the hMGL in water.

As an additional proof of the lid domain flexibility, a wide exploration of the conformational space described by the CVs was achieved in this case. Nonetheless, the FES profile obtained showed remarkable differences in comparison to the FES of hMGL in water. A free-energy minimum corresponding to the open lid domain conformation was present and, more interestingly, the FES profile showed the tendency of the system to assume a more disclosed conformation. Conversely, no free-energy minima corresponding to the closed lid domain were identified (Figure 18).

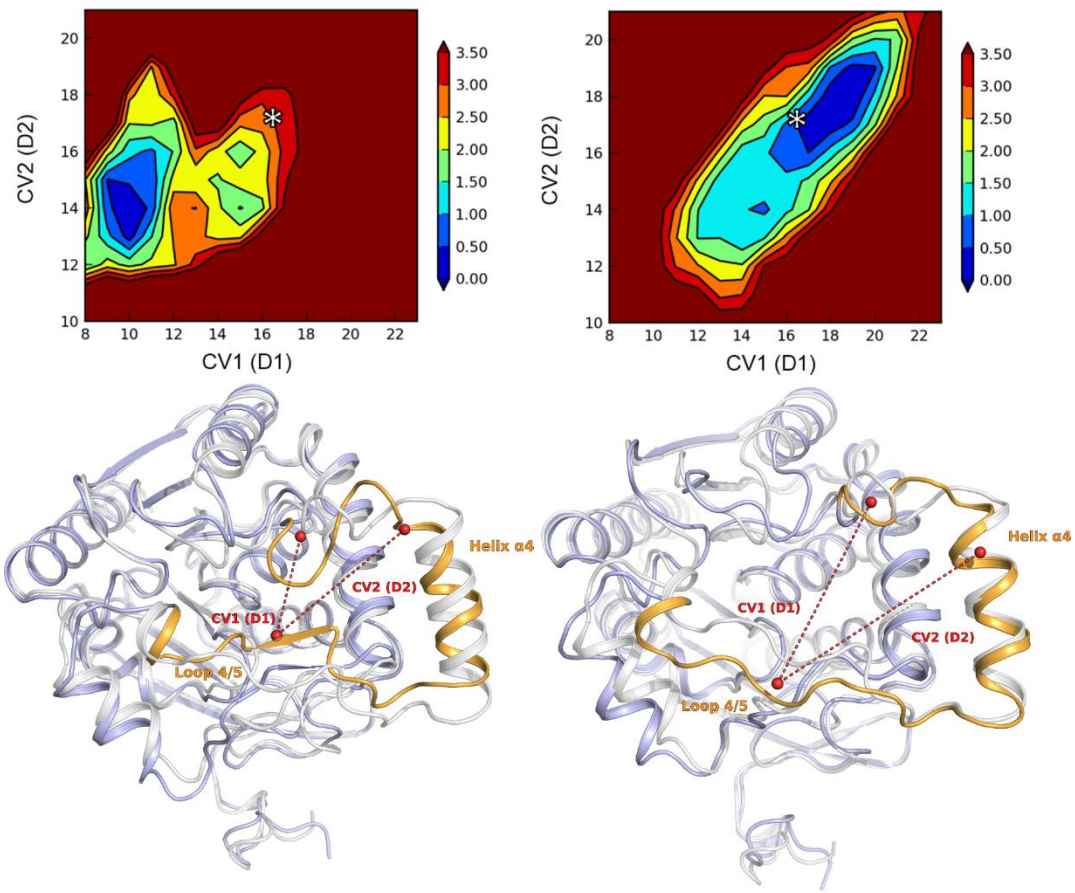


*Figure 18 The FES profile of native hMGL in water (left) and in presence of a membrane model (right). White asterisks mark the CVs values measured for the crystal structure of hMGL in its open conformation (PDB 3HJU). For the free-energy minima, representative structures are reported (light blue cartoon); the lid domain portion corresponding to helix α4 and loop 4/5 is depicted in orange. The variation of the CVs values is also represented by red dashes. The structures from WT Metadynamics simulations are superposed to the crystal structure of hMGL in its open conformation (grey cartoon).*

These results are consistent with both experimental and computational data recently presented, and furthermore support the hypothesis that MGL regulates the substrate recruitment by interacting with the phospholipid bilayer, which in turn might facilitate the 2-AG engagement by favouring the disclosure of the active site access channel[113].

*Free-energy studies of different hMGL models in presence of a POPC model*

The results of free-energy studies showing the importance of the presence of the phospholipid membrane to stabilise hMGL in its open conformation, which is energetically hindered in water, encouraged supplementary research in order to understand whether the oxidation of C201 and C208 is sufficient to perturb the conformational equilibrium of MGL, in spite of the membrane-mediated stabilising effect. To this aim, WT Metadynamics of hMGL modelled with C201 or C208 oxidised to sulfenic acid, hMGL modelled with both C201 and C208 oxidised to sulfenic acid and, finally, of hMGL modelled with a sulfenamide adduct at C208 and F209 backbone were performed. Finally, WT Metadynamics simulations of hMGL modelled C201A and C208 mutations were performed, in order to validate the hypothesis of the relationship between the lid domain conformational rearrangements and the oxidation of C201 and C208.

In spite of the presence of the POPC membrane, WT Metadynamics studies of hMGL modelled with oxidised forms of C201 and C208 revealed a different and unexpected scenario. The resulting FES profiles were remarkably different from those obtained for native hMGL, and showed free-energy minima corresponding to a closed-lid domain conformation. More specifically, the FES profile of hMGL modelled with C201 mutated to sulfenic acid presented an energy basin corresponding to a conformation characterised by the reduction of the active site access tunnel (Figure 19). This event appeared to be driven mainly by a contraction of CV2 and, at a lower extent, of CV1, and is completely opposite to the tendency of native hMGL to maintain a stable open wide conformation.

A similar result was obtained for a model of hMGL with C208 oxidised to sulfenic acid. In this case, the conformational reshaping event was characterised by a more marked reduction of both CV1 and CV2, and the FES profile showed an energy minimum corresponding to the closed lid domain. As an additional proof of the influence that the modification of C201 and C208 side chains exerts on hMGL conformational reshaping, the FES of hMGL modelled with both C201 and C208 oxidised was comparable to that obtained for hMGL with C208 mutated to sulfenic acid (Figure 20). This result is in accordance with experimental data suggesting a cooperative interaction between the two residues[103].

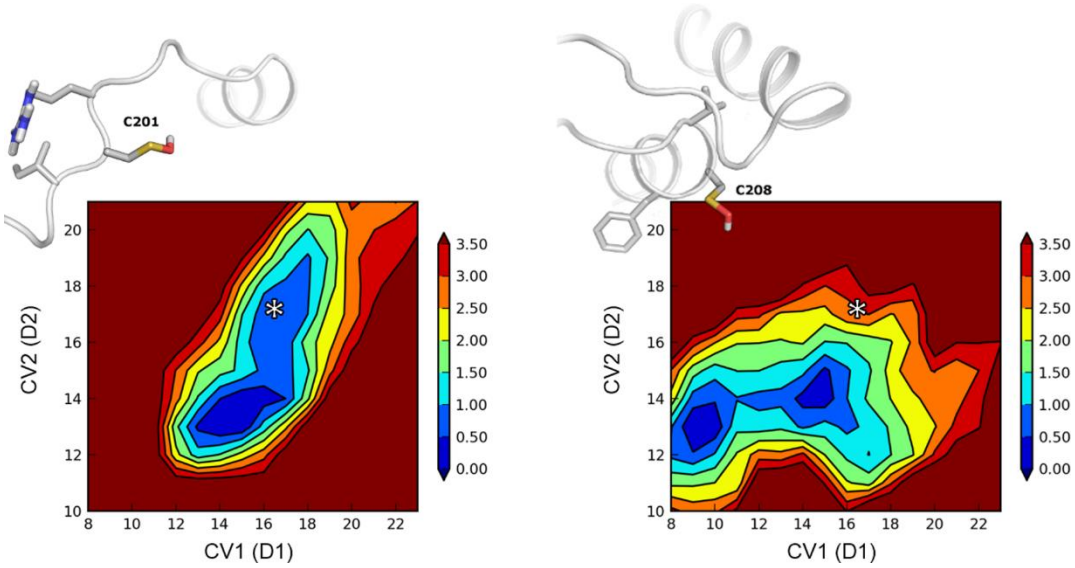


*Figure 19 Comparison of the FES profile of hMGL modeled with C201 (left) and C208 (right) oxidized to sulfenic acid. White asterisks mark the CVs values measured for the crystal structure of hMGL in its open conformation.*

These computational results are consistent with the biological data recently reported and provide a plausible mechanism for the sulfenylation-dependent blockade of rMGL activity, and with in-house data, which provide evidences for a similar behaviour for hMGL. On the other hand, although it was not possible to collect experimental data confirming the formation of a sulfenamide between C208 and F209 backbone, the effect of this transformation on the conformational equilibrium of the enzyme was evaluated. Notably, the FES obtained in this case was significantly different from those presented above, showing a free-energy minimum clearly circumscribed in a region defined by reduced distances between the lid domain rims, and thus corresponding to a completely closed conformation (Figure 20).

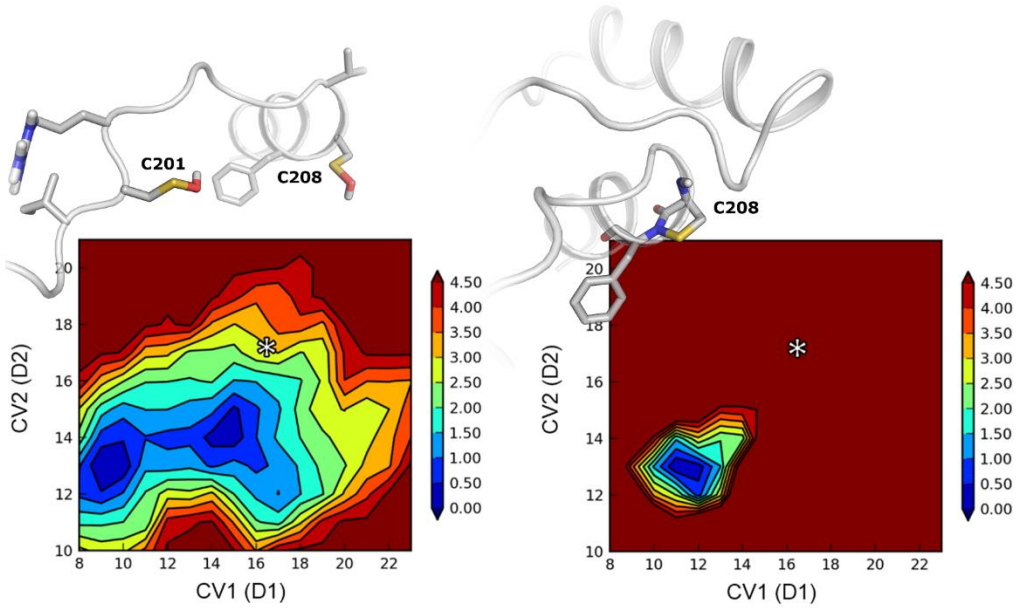


*Figure 20 The FES profile of hMGL with C201 and C208 modified to sulfenic acid show free-energy minima corresponding to the closure of the lid domain (left). The FES profile of hMGL with C208 modified to sulfenyl amide show free-energy minimum corresponding to the closure of the lid domain (right). A white asterisk marks the CVs values measured for the crystal structure of hMGL in its open conformation.*

## *Free-energy studies of hMGL with site-directed mutations C201A and C208A*

Following the results obtained from computational studies, and considering the line of evidences coming from biological and mass spectrometry experiments, a mechanism explaining the sulfenylation-mediated MGL inhibition was hypothesised. According to this model, the lid domain, which is known to act as a flexible gate, is maintained in a stable locked conformation by the specific chemical modification of C201 and C208. To test specificity of the model, i.e. its ability to distinguish inactivating from neutral chemical modifications, WT Metadynamics simulations of hMGL modelled with C201 and C208 mutated to alanine were performed.

Data from the literature outline that C201A and C208A mutations suppress the sulfenylation-mediated rMGL inhibition and that, on the other hand, do not affect the kinetics properties of the human enzyme. The investigation of the effect of C201A and C208A mutations on our hMGL model was thus of straightforward importance.

Notably, the FES profiles obtained for both the site-directed mutations models outlined the presence of free-energy minima corresponding to reduced values of CV1 and CV2 and thus related to slightly closed conformations of the lid domain. However, the FES also clearly showed the presence of energy wells matching the open conformation of the crystal structure 3HJU, which were completely absent on the FES of hMGL models with oxidised regulatory cysteines (Figure 21).

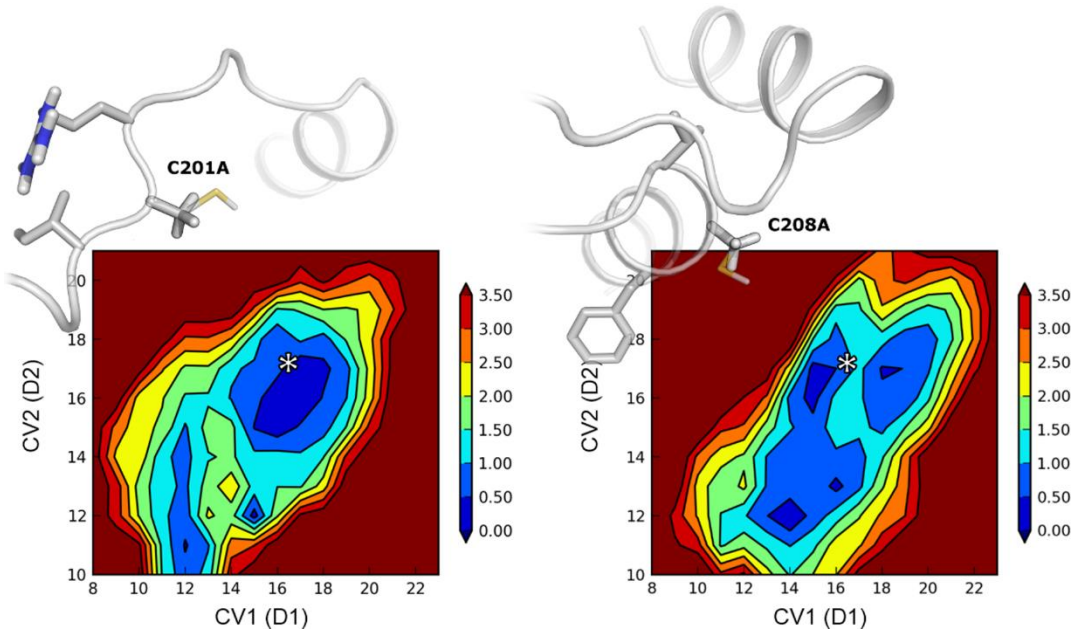


*Figure 21 Comparison of the FES oh hMGL with C201A (left) and C208A (right). A white asterisk marks the CVs values measured for the crystal structure of hMGL in its open conformation.*

## *Conclusions*

The combination of unbiased MD simulations and free-energy studies allowed to elucidate the possible events that govern the conformational space of hMGL, and specifically of the lid domain. The results of these studies reveal that the lid domain conformation is strongly influenced by the presence of the phospholipid bilayer, which maintain and favour a stable and completely open conformation, disclosing the active site access. This particular rearrangement is discouraged in absence of the membrane. This result came unexpectedly, since MGL was found to act as an amphitropic protein. On the other hand, these

observations are consistent with the fact that the activity of MGL, similarly to other lipases, is regulated by the interaction with lipid bilayers, according to the interfacial activation mechanism. The results of this work supply thus important information on the role of lipid models in molecular modelling studies on MGL, and provided valuable indications that have been extensively considered within this research project.

On the other hand, the aim of this project was the evaluation of the role of regulatory cysteine residues 201 and 208, which act as oxidative *stimuli*-sensitive switchers, able to regulate the enzyme activity depending on their oxidation state and, generally, on the environment redox state. The sulfenylation of these residues, that is, their modification to sulfenic acid, determines a wide conformational reshaping involving the lid domain and leading to its complete closure. This event would hide the catalytic site and hamper the recruitment of 2-AG from the cellular membrane, controlling the levels of the endocannabinoid at a cellular and extracellular level.

Following these premises, a feasible mechanism for the hydrogen peroxide-dependent MGL inhibition was hypothesised. According to this model, the events that trigger the oxidative-stimuli-mediated modulation of 2-AG levels are governed by the regulation of the lid domain motion, which is stabilised in a closed conformation by the oxidation of C201 and C208 to sulfenic acid. This model is corroborated by free-energy studies showing that the mutation of C201 and C208 to alanine is sufficient to reinstate the open conformation, related to the catalytically active enzyme.

While this hypothesis is corroborated by experimental data on the hydrogen-peroxide-mediated inhibition of rat and human MGL, the possibility that the sulphenylation of C208 may lead to the formation of a sulfenamide species was speculated in this project. This unstable species would protect the cysteine from the irreversible oxidation to sulfinic or sulfonic acid, hampering the irreversible blockade of the enzyme.

## *Computational protocol*

### *Protein Preparation*

In this work, the monomer A (chain A) of hMGL crystallised in its open conformation (PDB ID: 3HJU)[104] was used. The protein was prepared using the Protein Preparation Wizard[a] workflow within Maestro 9.6[b] in the Schrödinger 2013-3 suite. Hydrogen atoms were added to the structure and the protonation state of ionisable amino acids were chosen to be consistent with physiological pH. The overall hydrogen bonding network was optimised by fixing the tautomers of histidine residues and the orientation of hydroxyl and thiol groups, as well as the orientation of asparagine and glutamine side chains. Protein termini were protected with capping neutral groups. The glycerol molecule co-crystallised with MGL was removed, and the system was subjected to a restrained minimisation using the OPLS2005 force field to an overall RMSD of 0.3 Å.

Models of hMGL with modifications at C201 and C208 side chains (sulfenic acid, sulfenamide and site directed mutations to alanine) were built in Maestro.

### *Molecular Dynamics simulations*

Molecular Dynamics Simulations were performed using Desmond version 3.6[c]. The protein was solvated by approximatively 30600 spc[153] water molecules in a simulation box of 76Å× 72Å × 64Å. The OPLS2005[154] force field implemented in Desmond was used to model the systems. Bond lengths to hydrogen atoms were constrained by applying the M-SHAKE algorithm. Short-range electrostatic interactions were cut off at 9Å, whereas long-range electrostatic interactions were treated using the Smooth Particle Mesh Ewald method. A RESPA integrator was used with a time-step of 2 fs, while long-range electrostatic interactions were computed every 6 fs.

### *MD simulations Equilibration protocol*

Each MD simulation was performed was carried out in the NPT ensemble, coupling to the Langevin thermostat method.

The stages of the relaxation process are:

1. Minimization with the solute restrained
2. Minimization without any restraints

---

[a] Schrödinger Suite 2013-3 Protein Preparation Wizard; Epik version 2.6, Schrödinger, LLC, New York, NY, 2013; Impact version 6.1, Schrödinger, LLC, New York, NY, 2013; Prime version 3.4, Schrödinger, LLC, New York, NY, 2013.

[b] Maestro, version 9.6, Schrödinger, LLC, New York, NY, 2013.

[c] Desmond Molecular Dynamics System, version 3.6, D. E. Shaw Research, New York, NY, 2013. Maestro-Desmond Interoperability Tools, version 3.6, Schrödinger, New York, NY, 2013.

3. 200 ps simulation in the NVT ensemble using the Langevin thermostat with:
    a. temperature of 10 K
    b. 50 kcal/mol restraint on solute heavy atoms
4. 100 ps simulation in the NVT ensemble using the Langevin thermostat with:
    a. temperature of 100 K
    b. 25 kcal/mol restraint on protein backbone and beta carbons
5. 100 ps simulation in the NVT ensemble using the Langevin thermostat with:
    a. temperature of 200 K
    b. 25 kcal/mol restraint on protein backbone and beta carbons
6. 400 ps simulation in the NVT ensemble using the Langevin thermostat with:
    a. temperature of 300 k
    b. 12.5 kcal/mol restraint on protein backbone and beta carbons
7. 400 ps simulation in the NPT ensemble using the Langevin thermostat with:
    a. temperature of 300 k
    b. 12.5 kcal/mol restraint on protein backbone and beta carbons
8. 800 ps simulation in the NPT ensemble using the Langevin thermostat with:
    a. temperature of 300 k
    b. 5 kcal/mol restraint on protein backbone and beta carbons
9. 1000 ps simulation in the NPT ensemble using the Langevin thermostat with:
    a. temperature of 300 k
    no restraint on solute.

*WT Metadynamics in water*

The system was prepared following the same procedure used for the MD simulations. The free-energy profile of native hMGL was computed using the Well-Tempered Metadynamics implemented in Desmond 3.6. Metadynamics enhances the sampling of the specific collective variables (CVs; $s(s_1, s_2, \ldots s_m)$ in Equation 1) by adding a history-dependent potential $V(s, t)$. The potential $V(s, t)$ is the sum of Gaussians centred along the CVs trajectory.

$$V(s,t) = \sum_{j=1}^{n} G(s, t_j) = \sum_{j=1}^{n} w_j \prod_{i=1}^{m} \exp\left(-\frac{\left[s_j(t) - s_j(t_j)\right]^2}{2\sigma^2}\right)$$

(Eq.1)

$$t_{j+1} = t_j + \tau$$

(Eq.2)

According to Equation 1, Gaussians are deposited at specified time intervals, and are added to *V(s, t)*. The coordinates of the Gaussian deposition are determined by the current CVs values. In this work, distances between centres of mass of Cα of selected residues on the lid domain were used as CV1 ($s_1$; distance between 176-179 Cα and 150-157 Cα centres of mass) and as CV2 ($s_2$; distance between 176-179 Cα and 158-164 Cα centres of mass). The Gaussian width $\sigma$ was set to 0.05 Å, the Gaussian height $w_j$ was set to 0.03 kcal/mol, while the deposition time $\tau$ was 0.09 ps. In WT Metadynamics, the Gaussians heights $w_j$ are resized taking into account the value of *V(s, t)*

$$w_j = w \times \exp\left(\frac{V(s, t_j)}{k_B \Delta T}\right)$$

(Eq.3)

where the initial height of the Gaussians *w* was 0.03 kcal/mol, $k_B$ is the Boltzmann constant and the sampling temperature $\Delta T$ was 1200 K. In order to evaluate the convergence of WT Metadynamics simulations, free energy differences recorded every 5ns were measured. Once the results stopped changing over time, the simulations were considered as converged. WT Metadynamics simulations were then replicated, in order to confirm the results. Each WT Metadynamics simulation lasted for 100ns and results were evaluated upon convergence.

*WT Metadynamics simulations in presence of a POPC membrane model*

The hMGL structure was embedded in a POPC lipid bilayer model according to the coordinates of the 3HJU crystal structure deposited into the Orientation of Protein in Membrane (OPM)[155] database, and the protein membrane system was then solvated by approximatively 63000 spc water molecules, in a simulation box of 84Å×81Å×136Å. The OPLS2005 force field implemented in Desmond 3.6 was used to model the systems. Bond lengths to hydrogen atoms were constrained by applying the M-SHAKE algorithm. Short-range electrostatic interactions were cut off at 9Å, whereas long-range electrostatic interactions were treated using the Smooth Particle Mesh Ewald method. A RESPA integrator was used with a time-step of 2 fs, while long-range electrostatic interactions were computed every 6 fs. The systems were relaxed using a modified version of a membrane relaxation protocol implemented in the Desmond package. WT-Metadynamics simulations parameters were set as described above.

*WT Metadynamics simulations in presence of a POPC membrane model (membrane equilibration protocol details)*

Each MD simulation was performed was carried out in the NPT ensemble, coupling to the Langevin thermostat method.

The stages of the equilibration protocol consists of a membrane relaxation step (a prolonged version of the Membrane relaxation protocol provided by Desmond 3.6 implemented in the Schrodinger 2013-3 suite), with protein restrained, followed by the relaxation extended to the entire system:

1. Minimisation with restraints on the solute heavy atoms
2. Minimisation without any restraints
3. 2000 ps simulation in the NVT ensemble with the Berendsen thermostat method with:
    a. a temperature raising to 300 K
    b. 50 kcal/mol restraints on protein heavy atoms
4. 1600 ps simulation in the NPT ensemble with:
    a. a temperature of 300 K
    b. 50 kcal/mol restraints on protein heavy atoms
5. 2000 ps simulation in the NPT ensemble with:
    a. a temperature of 300 K
    b. restraints on protein heavy atoms decreasing from 50 to 10 kcal/mol
6. 400 ps simulation in the NPT ensemble with:
    a. a temperature of 300 K
    b. 10 kcal/mol restraints on protein heavy atoms
7. 1000 ps simulation in the NPT ensemble with:
    a. a temperature of 300 K
    b. 2 kcal/mol restraints on protein heavy atoms

The membrane relaxation was followed by a prolonged version of the equilibration protocol used to relax the protein before the MD simulations.

## *2.4 Design of novel benzisothiazolone derivatives as allosteric modulators of MGL activity*

The recent discovery of benzisothiazolone (BTZ) compounds as hit compounds for MGL inhibition has disclosed a new strategy for the design of selective MGL modulators, characterised by a reversible mechanism, which differentiates them from the irreversible active site-targeting inhibitors. As revealed by mutagenesis and MS data, BTZ-based compounds target C201 and C208, which represent thus an allosteric site. Moreover, evidences showing that these compounds inhibit MGL through the formation of a transient mixed disulfide bond suggest that BTZ ligands might represent a crucial point in the comprehension of the redox-dependent mechanisms ruling MGL activity.

The design of redox-reversible MGL modulators targeting the regulatory residues C201 and C208 is thus a promising strategy, aiming at the regulation of the enzyme activity and the consequent enhancement of 2-AG levels without the side effects related to the chronic MGL inactivation.

The results reported in this section are the outcome of an interdisciplinary work, involving the medicinal chemistry synthesis and bio-analytic units of our research group at the University of Parma. The research group of Prof. Piomelli at UCI performed the biological evaluation of the newly designed and synthesised compounds.

### *2.4.1 Characterisation of BTZ compounds*

BTZs are characterised by a sulfenamide-based sulfhydryl-reacting scaffold, and by the presence of driver groups, required for the drug-target recognition (R in Figure 22).

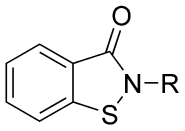


*Figure 22 Chemical structure of the benzisothiazolone scaffold.*

The sulfur atom is characterised by a marked electrophilic character, and may easily undergo the nucleophilic attack by amines, thiols, and halide, leading to the formation of sulfides or disulfides following a ring-opening event. Besides, BTZs are highly sensitive to reducing agents, including $H_2$, hydrides, and biological reducing agents, such as glutathione (GSH).

The high potency of compound **1** (Figure 23), that has been reported as the first potent BTZ-based MGL inhibitor ($IC_{50}$=59 nM), represents the starting point of an intense research aiming at the discovery of novel MGL modulators, endowed with higher selectivity and potency. To this aim, a particular attention was dedicated to the driver group R, in order to get a more complete information about the pharmacophoric space of allosteric site surrounding C201 and C208.

In order to evaluate the effect of the insertion of different substituents at the sulfenamide nitrogen on the drug recognition and, on the other hand, the effect of different substituents on the benzene ring on the reactivity of the sulfenamidic scaffold, synthesis and analytical studies have been performed on a wide series of BTZ derivatives. Conversely, computational studies, consisting of docking studies and free-energy simulations, were applied to the search and design of novel BTZs derivatives focusing on the decoration of the driver group.

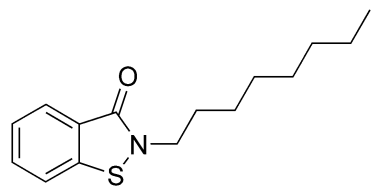


*N*-octylbenzisothiazolone
Compound **1**

*Figure 23 Chemical structure of compound **1**.*

### *2.4.2 Exploration of the pharmacophoric space: docking studies of UPR1218*

Starting from experimental evidences, suggesting that the insertion of a lipophilic substituent at the nitrogen atom is required to maintain a good potency profile, a phenethyl

derivative of the BTZ warhead (compound **2**, UPR1218) was synthesised. Notably, the insertion of an aromatic group in the side chain was sufficient to increase the inhibitory potency ($IC_{50}$=34.1 nM, on rMGL). In order to elucidate the role of the regulatory cysteine residues on UPR1218-dependent MGL inhibition, mutagenesis studies were performed. Interestingly, C201A, C208A and C201A/C208A mutants expressed in HeLa cells revealed a selectivity of **2** for C201. Going to details, C201A mutation is sufficient to determine a potency plunge ($IC_{50}$=242.9 nM), which is smaller for C208A ($IC_{50}$=72.6 nM); these evidences outlines suggest that **2** selectively target C201, in accordance with experimental data showing that BTZs preferentially interact with C201[156]. Interestingly, the double mutation C201A/C208A determines an even more marked drop of potency ($IC_{50}$=604.7 nM); this additive effect indicates that **2** inhibits MGL through a mechanism involving both C201 and C208, and that each cysteine gives an independent contribution to inhibition. The cysteine index value, calculated as the ratio between the $IC_{50}$ values on the double mutant C201A/C208A and the wild type enzyme, was considered as a parameter to evaluate the tendency of cysteine-targeting compounds to react with C201 and C208. Compound **2** shows a high cysteine index, which is suggestive of a selective interaction between the inhibitor and C201 or C208, or both. Conversely, a low cysteine index would indicate that the inhibition is mediated by the interaction with another sulfhydryl-sensitive site, i.e. C242. Rapid dilution assays revealed that **2** inhibits MGL through a reversible mechanism, consolidating the previous results obtained for this class of compounds and, more interestingly, providing evidences for high similarities in the effects produced by hydrogen peroxide and BTZs on MGL enzymatic activity. In order to evaluate the ability of **2** to regulate 2-AG levels, *in vitro* and *in vivo* experiments were performed. The levels of lactate dehydrogenase (LDH) in neuro-2a cells incubated with high levels of $H_2O_2$ were monitored, in order to evaluate the toxic effect mediated by the exposition to the oxidative stress stimulus. High levels of LDH were observed in presence of the selective $CB_1$ antagonist rimonabant, but not in presence of the $CB_2$ antagonist AM630. On the other hand, cultures incubated with $H_2O_2$ and the irreversible inhibitor JZL184 showed a reduced release of LDH. The co-administration of $H_2O_2$ and **2** exerted a protective effect against oxidative damage comparable to that produced by the treatment with JZL184. Notably, administration of **2** in a rat model, with a dose of 30 mg/Kg, determined an increase of 2-AG levels in the

brain after 2 hours. Taken together, these evidences indicate that **2** exerts a $CB_1$-dependent protective effect against oxidative damage, by enhancing in a reversible manner the 2-AG levels, and thus providing an alternative strategy to the chronic blockade of MGL produced by irreversible inhibitors such as JZL184.

In order to evaluate the binding mode of **2**, and to provide information for the rational design of more potent BTZ derivatives, a covalent docking study was performed. Following the proposed mechanism, consisting in the formation of a mixed disulfide between C201 thiol group the sulfur atom of BTZ compounds, the crystal structure 3HJU of hMGL was used as model structure for covalent docking studies, and modelled with C201 covalently bound to an opened-ring molecule of **2**. The docking poses obtained reveal a polar interaction between the sulfenamidic nitrogen and the backbone oxygen of P198, stabilising the binding mode. On the other hand, the aromatic ring of the driver group is accommodated within a surface-exposed hydrophobic cleft, lined by residues P11, Q12, G81, P198 and L199 (Figure 24).

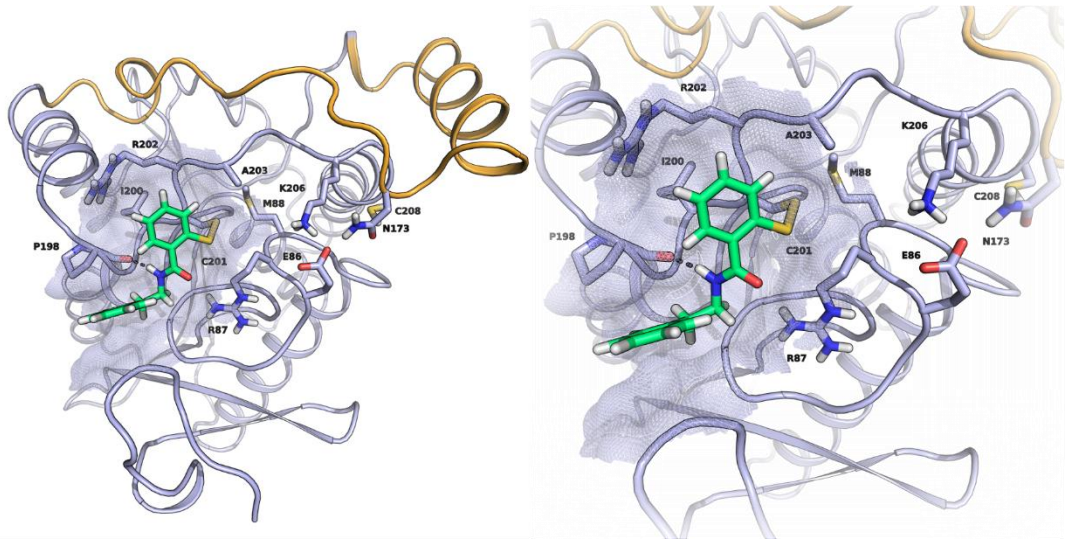


*Figure 24 Binding mode of compound **2** (green carbons) covalently bound to C201; the binding site is situated below the lid domain (orange cartoon). On the right, detail of the covalent adduct: compound **2** pose is stabilised by the formation of a hydrogen bond between the nitrogen atom and the oxygen backbone of P198.*

### *2.4.3 Evaluation of the effects of URB1218 on hMGL conformational equilibrium*

Experimental data have revealed that **2** determines an MGL blockade through a reversible mechanism, showing dose-response curves perfectly overlapping those obtained from the treatment of the enzyme with $H_2O_2$. On the other hand, the results of free-energy studies discussed above suggest that the oxidative-dependent MGL inhibition is mediated by a conformational rearrangement of the lid domain, which would hamper the access of the substrate to the catalytic site. In order evaluate the effect of the formation of a disulfide between C201 and **2** on the conformational equilibrium of hMGL, WT Metadynamics simulations were performed.

The model obtained from the covalent docking study, embedded in a POPC membrane model, was used as a starting point for the free-energy studies. As for the WT Metadynamics simulations of hMGL described in the previous chapter, the distances between centres of mass of Cα of residues on the lid domain were used as CV1 (distance between 176-179 Cα and 150-157 Cα centres of mass) and as CV2 (distance between 176-179 Cα and 158-164 Cα centres of mass).

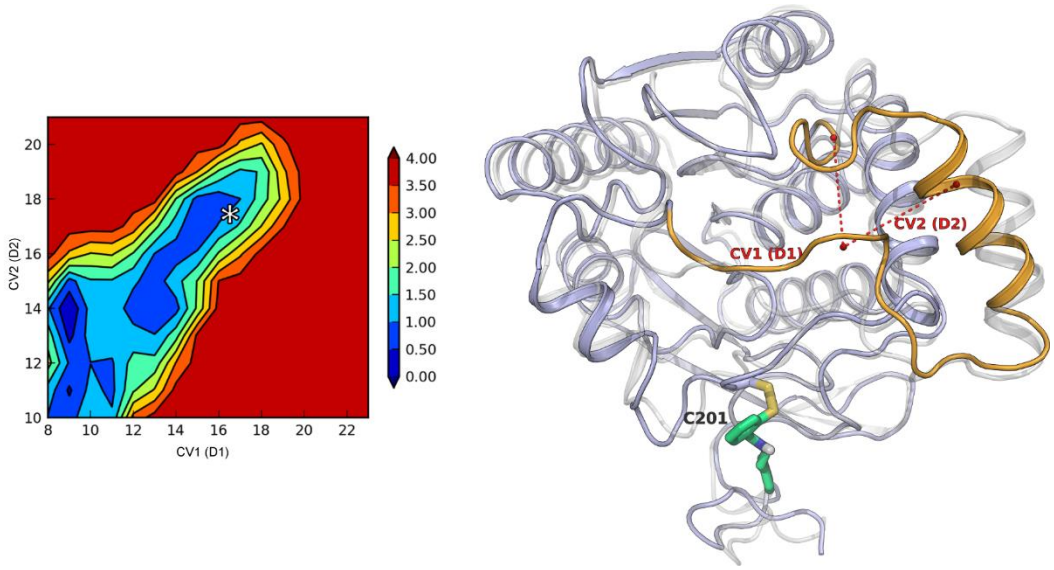


*Figure 25 The FES of WT Metadynamics (left) on hMGL modelled with a molecule of compound **2** covalently bound to C201 reveals an energy minimum corresponding to a closed-lid domain conformation (right).*

Similarly to what has been observed for hMGL modelled with C201 and C208 oxidised to sulfenic acid, the chemical modification of C201, temporarily oxidised as a consequence of the formation of a covalent adduct with **2**, determines a huge conformational reshaping limited to the lid domain. The FES obtained presents a free-energy minimum corresponding to closed-lid domain conformation (Figure 25), showing an opposite tendency of the system compared to the native hMGL, hMGL-C201A and hMGL-C208A systems. On the other hand, evident similarities in the effect produced on the conformational equilibrium of MGL reflect the analogies observed in the enzyme responses to the administration of both $H_2O_2$ and a selective cysteine-targeting inhibitor such as URB1218 (compound **2**).

### *2.4.4 Design, synthesis and biological evaluation of novel benzisothiazolone derivatives*

Starting from the scaffold of compound **2**, different derivatives were designed, in order to evaluate the effect on the inhibitory potency of these compounds determined by modifications of the side chain linker and by the insertion of different groups on the phenyl ring of the driver group. Moreover, the possibility to target both C201 and C208 through the coupling of two cysteine-reacting groups was investigated.

The introduction of a nitrogen atom at the α position of the sulfenamidic group led to the synthesis of compound **3**. As revealed by covalent docking studies, compound **3** assumes a binding mode comparable to the conformation adopted by the covalently bound compound **2**. Similarly to compound **2**, the interaction between **3** and MGL is strengthened by the formation of an hydrogen bond involving the oxygen of P198 backbone and the exocyclic nitrogen of the inhibitor (Figure 26, left panel). Compound **3** is characterised by an increased inhibitory potency ($IC_{50}$=19.5 nM) and, interestingly, by a reduced selectivity for C201 over C208. The single mutations C201A and C208A do not determine a drastic drop of potency, as observed for **2**, and the compound shows a comparable potency on the single mutants ($IC_{50}$=54.4 nM on C201A and 44.9 on C208A). On the other hand, the double mutation of C201 and C208 produces a marked potency plunge ($IC_{50}$=782.0 nM), suggesting that compound **3** can easily inhibit both single mutants, interacting either with

the spared C201 or C208. Notably, the introduction of the exocyclic nitrogen atom may also promote an enhancement of compound **3** solubility.

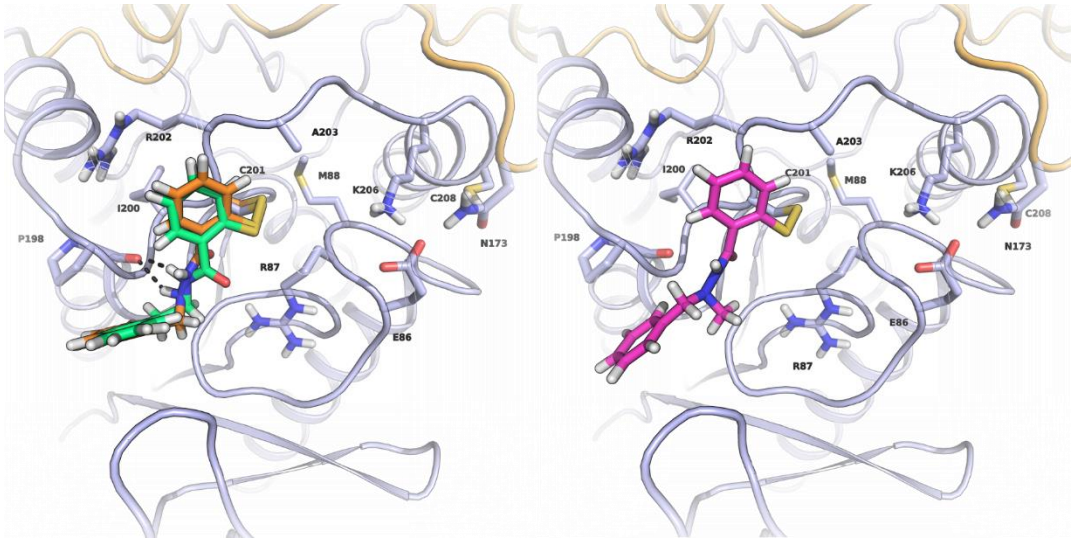


*Figure 26 On the left: covalently bound compounds **2** (green carbons) and **3** (orange carbons) assume a similar binding mode, strengthened by the formation of a hydrogen bond with P198 (black dashes). On the right: the introduction of the N-methyl group in compound **4** hinders the formation of polar interactions between the ligand and the protein.*

Starting from the encouraging results obtained for compound **3**, the structure-activity relationships of 2-amino BTZ derivatives were investigated (Figure 27). The introduction of a methyl group on the exocyclic nitrogen yielded compound **4**. The covalent docking studies revealed that the insertion of the methyl group is detrimental for the formation of positive interactions between the inhibitor and the enzyme, hampering the formation of the hydrogen bond between P198 and the nitrogen atoms of both the sulfenamidic core and the driver group (Figure 26, right panel). These results reflect the ten-fold loss of activity observed for compound **4**.

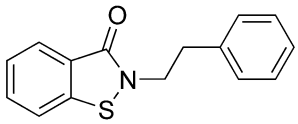

Compound **2**

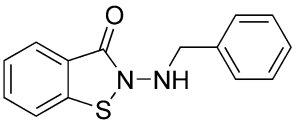

Compound **3**

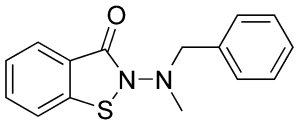

Compound **4**

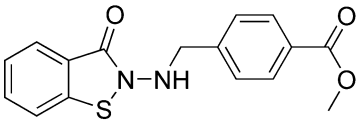

Compound **5**

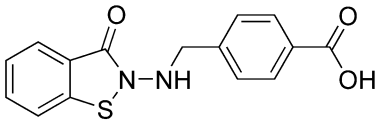

Compound **6**

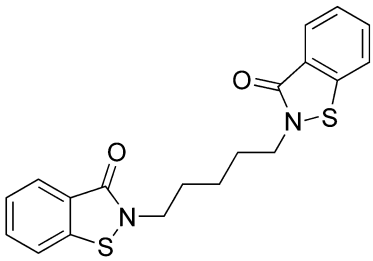

Compound **7**

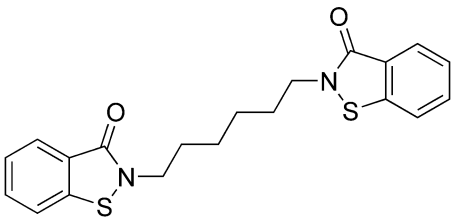

Compound **8**

*Figure 27 Chemical structures of BTZ derivatives.*

In order to evaluate the effect of the introduction of polar substituents on the phenyl ring of the driver portion, compounds **5** and **6**, characterised by the presence of a methyl ester group and of an acid group, respectively, in the para position of the benzylamino side chain, were designed. The docking studies of **5** and **6** suggest similar binding modes for the two compounds, involved in the formation of polar contacts with K206 (compound **5**; Figure 28, left panel) and eventually with E86 (compound **6**; Figure 28, right panel). Notably, K206 and E86 are involved in the formation of a saline bridge, and are both in close contact with the second critical cysteine residue, C208. On the other hand, these interactions outlined by the computational model do not reflect a specific *in vitro* enhancement of activity ($IC_{50}$=93.9 nM for **5** and 277.7 nM for **6**).

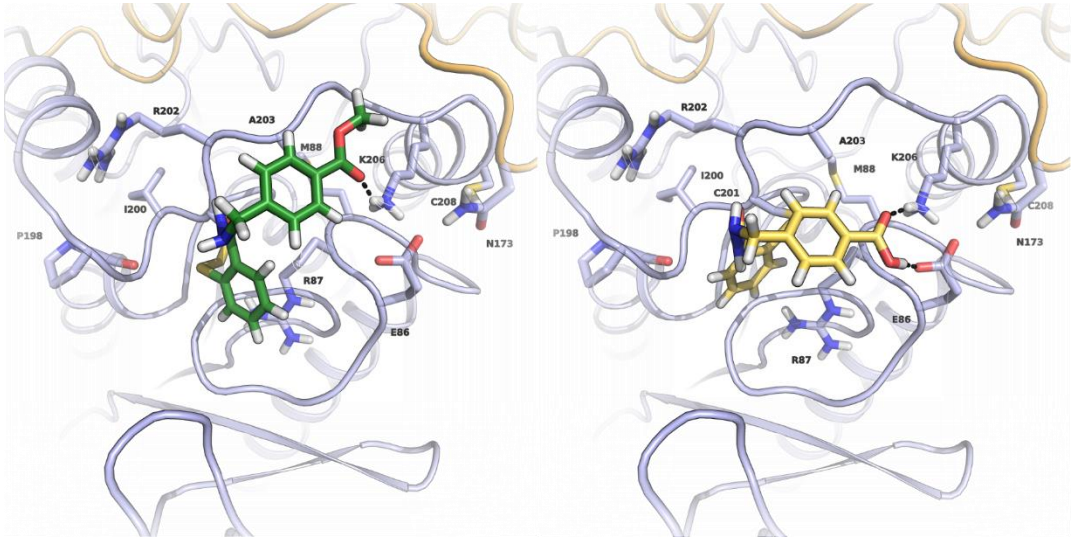


*Figure 28 Binding modes of compounds **5** (dark green carbons, on the left) and **6** (yellow carbons, on the right) show a similar interaction with K206; hydrogen bonds are highlighted by black dashes.*

| | $IC_{50}$ (nM) | | | | |
|---|---|---|---|---|---|
| **Compound** | **Wild type** | **C201A** | **C208A** | **C201A-C208A** | **Cys Index (C201A-C208A/WT)** |
| **2** | 34.1 ± 2.0 | 242.9 ± 18.0 | 72.6 ± 30.3 | 604.7 ± 10.2 | 17.7 |
| **3** | 19.5 ± 0.8 | 54.4 ± 4.1 | 44.9 ± 8.7 | 782.0 ± 77.5 | 40.1 |
| **4** | 189.4 ± 39.7 | / | / | / | / |
| **5** | 93.9 ± 5.5 | / | / | / | / |
| **6** | 277.7 ± 1.9 | / | / | / | / |
| **7** | 11.5 ± 1.5 | 229.8 ± 69.0 | 219.8 ± 33.9 | 1460.7 ± 465.0 | 127.0 |
| **8** | 16.8 ± 0.4 | 114.3 ± 8.9 | 82.7 ± 11.6 | 2079.6 ± 40.0 | 129.3 |

*Table 1 Inhibition of purified rMGL with selective mutation of C201 and C208.*

The promising experimental results obtained for compound **3**, showing the beneficial effect produced by the exocyclic nitrogen, and highlighting the additive effect disclosed by the double C201A and C208A mutation, encouraged an alternative approach in the design of a novel BTZ derivatives. Specifically, mutagenesis studies supported the design of

compounds concurrently interacting with both C201 and C208, in order to exploit the additive effect exerted by the redox-dependent chemical modification of these residues.

In order to test this hypothesis, an induced fit docking (IFD) study of bidentate ligands was performed. The symmetric ligands are characterised by the presence of two identic BTZ warhead based on compound **3**, separated by an alkyl spacer of variable length.

IFD results indicated compound **7** and **8**, characterised by a five- and six-membered alkyl chain, as promising bidentate MGL inhibitors. The flexible spacer of both **7** and **8** occupies the solvent-exposed regions separating C201 and C208, while the sulfenamidic sulfur atoms are situated in close contact with the thiol groups of C201 and C208 (Figure 29).

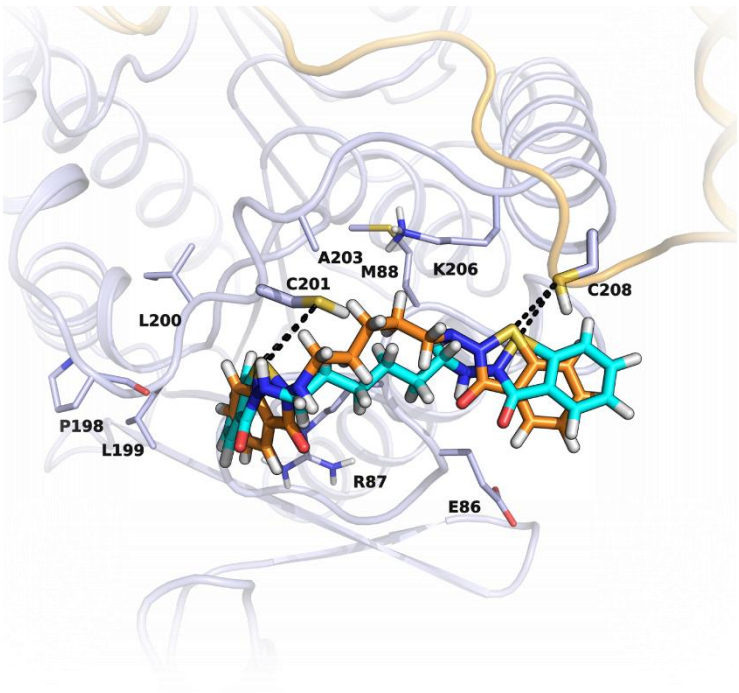


*Figure 29 Superposition of the binding modes of compounds **7** and **8**, which occupy the region between C201 and C208. Black dashes indicate the distance between the cysteine residues thiol groups and the sulfur atoms of the ligands.*

Notably, both compounds **7** and **8** are characterised by high potency, with an $IC_{50}$ of 11.6 nM and 16.8 nM, respectively. In order to investigate either the increased inhibitory activity

is attributable to the concurrent interaction with C201 and C208, *in vitro* assays with MGL mutants were performed. The single mutation of C201 or C208 to alanine was sufficient to determine a twenty-fold decrease of inhibitory potency for compound **7** ($IC_{50}$=229.8 nM on C201A and 219.8 nM on C208A); consistently, the cysteine index value obtained was very high (1460.7), supporting the proposed mechanism of double and simultaneous interaction with the cysteine residues. On the other hand, compound **8** showed a lower loss of activity compared to **7**, especially on C208A ($IC_{50}$=82.7 nM), but maintained a high value of cysteine index, confirming the expected mechanism of action.

## *Conclusions*

MGL represents a pharmacological target of extraordinary importance, considering the wide effects exerted by its substrate in the CNS and in peripheral tissues. On the other hand, the experimental evidences showing the detrimental effects produced by the chronic blockade of MGL have made the development of active site-directed inhibitors a questionable approach. In this perspective, the discovery of partially reversible modulators, able to interact with the allosteric site represented by the regulatory cysteine residues 201 and 201, is a fundamental step forward in the field of the search of novel MGL inhibitors.

Isothiazolone and benzisothiazolone scaffolds can thus be considered a promising starting point for the development of novel MGL modulators. The analogies observed between the effects exerted by these compounds and by hydrogen peroxide represent a key point in the comprehension of the mechanisms ruling the enzyme responses to oxidative *stimuli*. Specifically, while MGL inhibition represents an effective counteraction against oxidation damages, BTZs might reproduce the same protective effects, while avoiding the impairments related to oxidative stress.

Starting from these premises, a comprehensive SAR study for BTZ derivatives has been performed, coupled to enhanced sampling simulations, have been performed, in order to shed light on the mechanism of action of these compounds, and to identify novel lead compounds.

These studies led to the identification of compounds **2** and **3**, and of bidentate ligands **7** and **8** as promising compounds, characterised by an improved inhibitory activity compared to

the reference compound **1** reported in the literature. On the other hand, the SAR obtained for these derivatives revealed that, while modifications at the driver portion can improve the drug-target recognition and enhance the ligands affinity, the phenethyl side chain has only a marginal role in the mechanism laying behind BTZ-mediated MGL inhibition. Conversely, the high potency of these compounds is attributable to the high reactivity of the sulfenamidic core towards cysteine thiol groups. Furthermore, the absence of a proper binding site surrounding the solvent exposed region of the allosteric cysteines hinders the possibility to get an exhaustive comprehension of the binding modes of BTZs at their site of action.

Thanks to the collaboration with the research group of Prof. Piomelli, the main achievement of this project was the characterisation of the mechanism of action of BTZs, which mimic the hydrogen peroxide-dependent blockade of MGL. *In vitro* and *in vivo* studies sustained the hypothesised mechanism of action, providing evidences for the BTZ-mediated enhancement of 2-AG and reduction of cellular damages produced by hydrogen peroxide. WT Metadynamics performed on hMGL modelled with a covalent adduct between C201 and UPR1218 (compound **2**) unveiled a plausible mechanism for BTZ-mediated MGL blockade. Free-energy studies suggest that, similarly to what have been observed in previous investigations, the redox-dependent modification of regulatory cysteines may represent the triggering event responsible for the closure of the lid domain, precluding the access of 2-AG to the active site.

## *Computational protocol*

### *Protein preparation*

In this work, the monomer A (chain A) of hMGL crystallised in its open conformation (PDB ID: 3HJU) was used. The protein was prepared using the Protein Preparation Wizard [d]workflow within Maestro 9.2[e] in the Schrödinger 2012 update 2 suite. Hydrogen atoms were added to the structure and the protonation state of ionisable amino acids were chosen to be consistent with

[d] Schrödinger Suite 2011 Protein Preparation Wizard; Schrödinger, LLC: New York, 2011; Epik version 2.2; Schrödinger, LLC, New York, NY, 2011; Impact, version 5.7; Schrödinger, LLC: New York, 2011; Prime, version 3.0; Schrödinger, LLC: New York, 2011.
[e] Maestro, version 9.2; Schrödinger, LLC: New York, 2011.

physiological pH. The overall hydrogen bonding network was optimised by fixing the tautomers of histidine residues and the orientation of hydroxyl and thiol groups, as well as the orientation of asparagine and glutamine side chains. Protein termini were protected with capping neutral groups. The glycerol molecule co-crystallised with MGL was removed, and the system was subjected to a restrained minimisation using the OPLS2005[154] force field to an overall RMSD of 0.3 Å.

*Covalent docking studies of compounds **2-6***

The Prime Covalent Docking tool within Prime 3.1[f] was used to perform covalent docking studies.

The covalent docking protocol operates by defining the protein residue and the ligand atoms involved in the formation of the covalent adduct. The procedure allows to sample the conformations of the side chains lining the binding site, while the backbone is maintained in its original conformation. The procedure works through the following steps:

1. The side chains of selected residues included in the sampling are temporarily removed, to allow the accommodation of the ligand.
2. The rotatable bonds of the ligand and of the side chain of the attachment residue are sampled, leading to the identification of a high number of initial poses.
3. The initial poses are clustered.
4. For each cluster, the side chains removed at step 1 are reintroduced for prediction and refinement.
5. For each cluster, the attachment residue, the ligand and the residues included in the sampling are refined and minimised.

The outcomes from step 5 are collected as covalent docking poses.

In this work, both the attachment residue (C201) and residues within 8 Å of C201 were allowed to adjust in the sampling and refinement procedure. Compounds **2**-**6** were initially prepared using Ligprep 2.5[g], and then minimized with Macromodel 9.9[h], applying the OPLS2005 force field to an energy gradient of 0.05 kJ $mol^{-1}$ $Å^{-1}$. 20 poses were collected for each covalent docking run

[f] Prime, version 3.0; Schrödinger, LLC: New York, 2011.
[g] LigPrep, version 2.5; Schrödinger, LLC: New York, 2011.
[h] MacroModel, version 9.9, Schrödinger, LLC, New York, NY, 2011.

and ranked according to the Prime Energy values. The top ranked poses were selected and subjected to energy minimization to an energy gradient of 0.05 kJ $mol^{-1}$ $Å^{-1}$.

*Induced Fit Docking study of compounds **7** and **8***

The Induced Fit Docking (IFD) protocol was applied in order to account for both ligands and protein flexibility during the ligand docking procedure. As a first step, a softened-potential docking was performed by applying van der Waals radii scaling factors of 0.6 and 0.5 on the non polar-atoms of the protein and the ligands, respectively. Energy grids for this first docking run were centred on Cys201 and Cys208, with the enclosing box length in X and in Y set to 10 Å and the box length in Z set to 16 Å. Compounds **7** and **8**, which were previously prepared with Ligprep 2.5, were then flexibly docked in the standard precision mode. The resulting complexes were then subjected to the protein refinement step. In this stage, residues within a distance of 6 Å from any ligand pose were refined through a side-chain conformational search[i] and finally minimized. The final step of the IFD procedure involved a further docking run[j] of the ligands in the protein structures generated in the previous step. The complexes were evaluated according to their IFD score and finally minimized with Macromodel 9.9[k], applying the OPLS2005 force field to an energy gradient of 0.05 kJ $mol^{-1}$ $Å^{-1}$.

*Free-energy studies of hMGL modelled with C201 covalently bound to UPR1218*

hMGL modelled with a molecule of UPR1218 covalently bound to C201 was embedded in a POPC lipid bilayer model according to the coordinates of the 3HJU crystal structure deposited into the Orientation of Protein in Membrane (OPM)[155] database, and the protein membrane system was then solvated by approximatively 63000 spc[153] water molecules, in a simulation box of 84Å×81Å×136Å. The OPLS2005[154]force field implemented in Desmond 3.6[l] was used to model the systems. Bond lengths to hydrogen atoms were constrained by applying the M-SHAKE algorithm. Short-range electrostatic interactions were cut off at 9Å, whereas long-range electrostatic interactions were treated using the Smooth Particle Mesh Ewald method. A RESPA integrator was used with a time-step of 2 fs, while long-range electrostatic interactions were computed every 6 fs. The systems were relaxed using a modified version of a membrane

[i] Prime, version 3.0; Schrödinger, LLC: New York, 2011.
[j] Glide, version 6.1; Schrödinger, LLC: New York, 2011.
[k] MacroModel, version 9.9; Schrödinger, LLC: New York, 2011.
[l] Desmond Molecular Dynamics System, version 3.6, D. E. Shaw Research, New York, NY, 2013.

relaxation protocol implemented in the Desmond package. The stages of the equilibration protocol consists of a membrane relaxation step (a prolonged version of the Membrane relaxation protocol provided by Desmond 3.6 implemented in the Schrodinger 2013-3 suite), with protein restrained, followed by the relaxation extended to the entire system:

1. Minimisation with restraints on the solute heavy atoms
2. Minimisation without any restraints
3. 2000 ps simulation in the NVT ensemble with the Berendsen thermostat method with:
    a. a temperature raising to 300 K
    b. 50 kcal/mol restraints on protein heavy atoms
4. 1600 ps simulation in the NPT ensemble with:
    a. a temperature of 300 K
    b. 50 kcal/mol restraints on protein heavy atoms
5. 2000 ps simulation in the NPT ensemble with:
    a. a temperature of 300 K
    b. restraints on protein heavy atoms decreasing from 50 to 10 kcal/mol
6. 400 ps simulation in the NPT ensemble with:
    a. a temperature of 300 K
    b. 10 kcal/mol restraints on protein heavy atoms
7. 1000 ps simulation in the NPT ensemble with:
    a. a temperature of 300 K
    b. 2 kcal/mol restraints on protein heavy atoms

The membrane relaxation was followed by a prolonged version of the equilibration protocol provided by Desmond 3.6.

The free-energy profile of the hMG-UPR1218 complex was computed using the Well-Tempered Metadynamics implemented in Desmond 3.6. In this work, distances between centres of mass of Cα of selected residues on the lid domain were used as CV1 (distance between 176-179 Cα and 150-157 Cα centres of mass) and as CV2 (distance between 176-179 Cα and 158-164 Cα centres of mass). The Gaussian width was set to 0.05 Å, while the Gaussian height was set to 0.03 kcal/mol, and the deposition time was 0.09 ps.

In WT Metadynamics, Gaussians heights are resized taking into account the value of $V(s, t)$, i.e. the potential values as a sum of the Gaussians deposited along the CV

$$w_j = w \times \exp\left(\frac{V(s, t_j)}{k_B \Delta T}\right)$$

(Eq.4)

where the initial height of the Gaussians *w* was 0.03 kcal/mol, $k_B$ is the Boltzmann constant and the sampling temperature $\Delta T$ was 1200 K. In order to evaluate the convergence of WT Metadynamics simulations, free energy differences recorded every 5ns were measured. Once the results stopped changing over time, the simulations were considered as converged. WT Metadynamics simulations were then replicated, in order to confirm the results. Each WT Metadynamics simulation lasted for 100ns and results were evaluated upon convergence.

## *2.5 Investigating the free-energy of 2-AG binding*

As already discussed, a major feature of hMGL is the presence of a lid domain, which serves as flexible gate for the recruitment of the substrate 2-AG through the interaction with the phospholipid bilayer of biological membranes.

The role of the membrane on the conformational equilibrium of the enzyme, and specifically of the lid domain, has been widely investigated[113,112], suggesting that the interaction between hMGL and the cellular membrane is a key element for the catalytic cycle of the enzyme. Specifically, the results of free-energy studies presented in this dissertation and recent experimental data[113] outline that the lid domain favours the engagement of the lipid substrate by assuming an extensively open conformation, stabilised by the interaction with the membrane. On the other hand, while it has been clarified that the presence of the membrane is sufficient to enhance the kinetic properties of the enzyme for the hydrolysis of 2-AG[113], the mechanism laying behind the recruitment of the substrate and the binding process are still to be elucidated.

In this work, free-energy studies have been applied to investigate the role of the membrane in the substrate-binding process.

### *2.5.1 Application of the Multiple Walkers Metadynamics approach to sample the 2-AG unbinding*

In order to provide an estimation of the free-energy profile associated to the bound and unbound state of 2-AG, the well-tempered Metadynamics method, coupled to the Multiple Walkers routine, was used.

As already discussed, the Metadynamics approach allows the enhanced sampling of a system conformational space, and accelerates rare events by introducing an appropriate history-dependent potential, while reducing the free-energy surface of the system of interest to a function of few collective variables (CVs). A properly defined potential, which is defined as Gaussians deposited along the CVs, discourages the system to re-visit the same phase space region, allowing a full exploration of alternative stable and meta-stable configurations. Once the system has visited with equal probability all the configurations

within the phase space, a free-energy surface profile is obtained as the picture negative of the potential added along the CVs[157,152,151].

The Multiple-Walkers implementation[158] is based on the concurrent run of N metadynamics simulations coupled to N independent walkers, which simultaneously fill a common free-energy well. In this case, the FES is given by the sum of the Gaussians deposited by each walker, which, does not interact with the other walkers and explores the CVs space in an autonomous manner. A specific implementation of the multiple walkers has been used in this work, allowing the independence of each run, except for the outcome file, containing the sum of the Gaussians deposited, and consenting a parallelised calculation.

The concurrent filling of free-energy wells by different walkers allows to overcome the Metadynamics issues related to the inaccuracy of the FES reconstruction, while providing an improvement in terms of the FES convergence.

### *Simulation of the 2-AG unbinding*

Molecular docking studies were performed to obtain a model of hMGL in complex with the natural substrate 2-AG. Consistently with the enzymatic mechanism of action and with X-ray crystallographic data, the 2-AG was docked within the binding site, placing the ester group in proximity to the nucleophile serine 122, and the glycerol head overalpping the glycerol molecule co-crystallised with hMGL[104]. The lipophilic tail extents within the wide cleft delimited by the hydrophobic residues of the lid domain inner rims.

In order to investigate the effect of the presence of the membrane on the binding free-energy profile of 2-AG, multiple-walkers WT Metadynamics was performed on hMGL in complex with the substrate. The model obtained from docking studies, embedded in a POPC membrane model, was selected as a starting point for the free-energy studies. The first collective variable (CV1) was the distance between the centre of mass of 2AG heavy atoms, and the centre of mass of the heavy atoms of the amino acid residues lining the cleft accommodating the polar head of 2-AG (i.e. A51, H121, S122, M123, Y124, H269). The second collective variable was selected as the dihedral angle between the inertial axis of the protein, determined by the axis passing through the centres of mass of the protein and of

helix α1 and α5, and the inertial axis of the 2AG, described as the axis passing through the centres of mass of the heavy atoms of the glycerol-head and of the substrate lipophilic tail.

The well-tempered implementation of Metadynamics was thus coupled to the multiple walkers routine, using four walkers. The four simulations lasted for 40 ns and the cumulative FES profile was evaluated.

Although this work is currently underway, and a comprehensive evaluation of the binding free-energy for 2-AG deserves further investigations, the preliminary results obtained provide general information about the unbinding mechanism of 2-AG.

The cumulative FES reveals a large and deep basin, corresponding to a reduced distance between the centres of mass of the ligand and of the protein (CV1), whose initial value, measured for the bound state, was of 7 Å. The analysis of CV1 of walkers #1 and #2 revealed the tendency of the ligand to rearrange its own conformation within the binding site, without the exploration of the unbound state. Notably, both the walkers revealed that the 2-AG polar head is strongly anchored to the hydrophilic cleft within the MGL binding site through the formation of hydrogen bonds between the hydroxyl groups of the substrate and H121 and Y194.

On the other hand, the FES also shows the presence of deep minimum corresponding to a high value of CV1, that is, 25-30 Å between the reference points on the protein and the ligand, and to a CV2 value around 0-1 rad. The analysis of CVs trend and of the trajectories revealed that the second basin corresponds to an unbound-2-AG state and, more specifically, to a membrane-embedded 2-AG state, explored by the walker #3 (Figure 30). Conversely, as revealed by the CVs and trajectories analysis, in walker #4 the ligand rapidly dissociates from MGL, but does not interact with the membrane, exploring the phase space within the water solvent box.

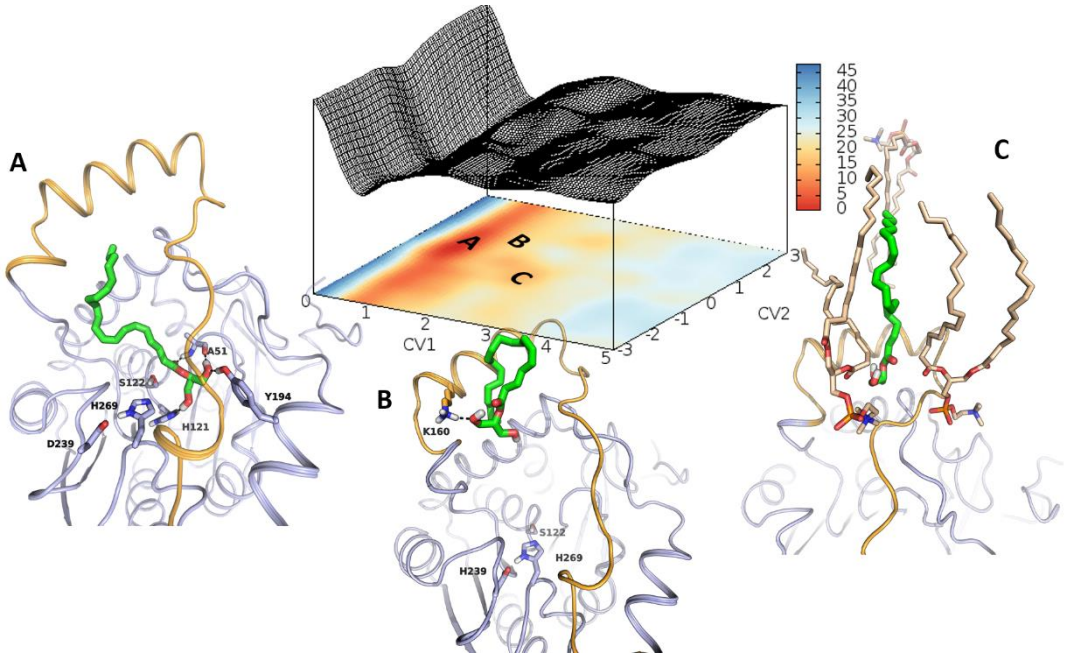


*Figure 30 Free Energy Surface obtained from the Multple Walkers WT-Metadynamics on hMGL complexed with 2-AG. CV1 is the distance (expressed in nanometres) between the centres of mass of selected residues within the binding pocket and of 2-AG. CV2 is the dihedral defining the torsion of the axes of inertia of the protein and of 2-AG. A deep energy well (A) corresponds to the bound-2-AG state; a second deep energy basin correspond to the membrane embedded-2-AG state (C). A second unbound-2-AG conformation, in which the substrate has abandoned the binding site, but is still interacting with the protein (B), corresponds to a higher energy basin.*

## *Conclusions*

Recent experimental data have confirmed that, similarly to other lipases, hMGL enzymatic activity is strongly affected by the interaction of its lid domain with the phospholipid bilayer. Nonetheless, the binding mechanism of 2-AG, and an estimation of the ligand binding free-energy are still unknown. In this project the Multiple Walkers Metadynamics, a particular implementation of the Metadynamics approach, was coupled to the Well-Tempered technique, in order to improve the efficiency of the phase space exploration and to ameliorate the convergence of the FES calculation.

The preliminary results of this work outline a scenario in which 2-AG populates two distinct free-energy minima, corresponding to a bound state and to an unbound/membrane-associated state, respectively. While these results represent a partial outcome of an

underway project, they provide the basis for further computational studies, aiming at the elucidation of the role of the cellular membrane on hMGL binding kinetics.

## *Computational protocol*

### *Protein Preparation*

In this work, the monomer A (chain A) of hMGL crystallised in its open conformation (PDB ID: 3HJU) was used. The protein was prepared using the Protein Preparation Wizard [m]workflow within Maestro 9.2[n] in the Schrödinger 2012 update 2 suite. Hydrogen atoms were added to the structure and the protonation state of ionisable amino acids were chosen to be consistent with physiological pH. The overall hydrogen bonding network was optimised by fixing the tautomers of histidine residues and the orientation of hydroxyl and thiol groups, as well as the orientation of asparagine and glutamine side chains. Protein termini were protected with capping neutral groups. The system was subjected to a restrained minimisation using the OPLS2005[154] force field to an overall RMSD of 0.3 Å.

### *Docking of 2-AG in hMGL*

All the compounds structures were built in Maestro 9.8[n] and optimised using LigPrep 3.0[o].

The docking studies were performed using Glide 6.3[o]. The docking grid was characterised by a cubic inner box of 20 Å, centred on the position of the co-crystallised molecule of glycerol. In order to obtain a proper orientation of the 2-AG polar head within the binding pocket, the formation of hydrogen bonds between the carboxylic oxygen atom of 2-AG and the backbone nitrogen of A51 and M123. Other settings, including the van der Waals radii, were maintained to their default value. The complexes obtained were then ranked according to the Emodel scoring function, which accounts for the internal strain energy of the model, the energy grid score and the binding affinity predicted by the GlideScore. The top-ranked poses were then submitted to minimisation using the OPLS2005 force field within MacroModel 10.4[p] applying the Polak-Ribiere conjugate gradient method to a covergence treshold of 0.05 kJ $mol^{-1}Å^{-1}$. During the

[m] Schrödinger Suite 2011 Protein Preparation Wizard; Schrödinger, LLC: New York, 2011; Epik version 2.2; Schrödinger, LLC, New York, NY, 2011; Impact, version 5.7; Schrödinger, LLC: New York, 2011; Prime, version 3.0; Schrödinger, LLC: New York, 2011.
[n] Maestro, version 9.2; Schrödinger, LLC: New York, 2011.
[o] Glide, version 6.3, Schrödinger, LLC, New York, NY, 2014.
[p] MacroModel, version 10.4, Schrödinger, LLC, New York, NY, 2014.

minimisation, the ligands and residues within 8 Å from them were free to move, while the backbone of other residues was kept fixed.

*System preparation*

hMGL modelled with a molecule of 2-AG covalently bound to C201 was embedded in a POPC lipid bilayer model according to the coordinates of the 3HJU crystal structure deposited into the Orientation of Protein in Membrane (OPM)[155] database. The protein membrane system was then solvated by approximatively 53000 TIP3P water molecules, using the System Builder tool implemented in Desmond 3.6[q]. The AMBER14 force field parameters were used to model the protein; the parameters for the ligand were obtained from the Generalized Amber Force Field (GAFF), while the phospholipid bilayer modelled using the Lipid14 parameters implemented in the AMBER14 release. Bond lengths to hydrogen atoms were constrained by applying the M-SHAKE algorithm. Short-range electrostatic interactions were cut off at 9Å, whereas long-range electrostatic interactions were treated using the Smooth Particle Mesh Ewald method. A RESPA integrator was used with a time-step of 2 fs, while long-range electrostatic interactions were computed every 6 fs. The system was equilibrated following the same equilibration protocol described above.

*Multiple Walkers WT-Metadynamics parameters*

The Plumed 2.1 plugin[159], combined to Gromacs 5.0.4[160] were used to engine the Multiple Walkers WT-Metadynamics simulation, with a total number of four walkers. The height of the Gaussians was set to 1, while the width was set to 0.35 nm for both the CVs, with a deposition frequency of 1 ps. The bias factor was set to 10 and the sampling temperature was set to 300K.

The data presented above have been collected at 40 ns of simulation time.

The Plumed 2.1 plugin was used to perform the analysis of the CVs and to recalculate the FES.

[q] Desmond Molecular Dynamics System, version 3.6, D. E. Shaw Research, New York, NY, 2013.

# 3. Bivalent ligands targeting FAAH and BuChE for AD treatment

Alzheimer's disesase (AD) is a worldwide diffused chronic neurodegenerative disorder mainly affecting population > 65 years of age, and characterised by typical symptoms such as the impairment of memory and cognitive processes, swings, disorientation and delirium. Most patients showing the symptoms have the sporadic form, which is characterised by a late onset (80-90 years of age) and is the consequence of a failure of the mechanisms involved in the elimination of amyloid-β (Aβ) peptides from specific areas in the brain. Aggregation of Aβ peptides, which are generated by the proteolytic cleavage of the transmembrane amyloid protein precursor (APP), leads to the formation of neuritic placques. This event has been related to the direct disruption of synaptic connections, and to dysfunctions mediated by small Aβ oligomers. Other histopathological hallmarks are represented by the formation of τ protein aggregates[161], neuroinflammation and oxidative stress[162–165].

A remarkable loss of presynaptic cholinergic neurons[166] in specific brain areas is also recognised as a key event in the deterioration of the cognitive processes. This evidence has led to the development of cholinesterase inhibitors targeting the enzymes responsible for acetylcholine (ACh) degradation, with the aim to potentiate the ACh-mediated transmission and to counteract in this way the loss of cholinergic neurons.

Despite years of research have been dedicated to the discovery of effective treatments, the complexity of this pathology hindered the identification of therapies that efficaciously block the AD progression, limiting the available marketed drugs to compounds that only alleviate the symptoms. Notably, these compounds, with the exception of memantine, an *N*-methyl-D-aspartate (NMDA) receptor antagonist, are cholinesterase inhibitors, including rivastigmine, donepezil and galantamine.

Recently, a new therapeutic approach has been developed with the aim to hit simultaneously diverse targets involved, at different levels, in the AD progression. To date, this approach has been found to be a successful strategy in order to get a combination of multiple effects mediated by ligands, named bivalent, or multivalent, ligands, bearing different

functionalities[167]. Given the multifactorial character of its aetiology, AD represents an optimal test field for the design of novel bivalent ligands.

Evidences showing that glia components have a critical role in different neurodegenerative diseases and, more specifically, that the microglia is activated in response to Aβ and neural damages events related to AD, have raised the interest in targeting this specific CNS cell population.

Notably, immunohistochemical experiments have evidenced that both $CB_2$ receptors and FAAH are selectively overexpressed in neuritic placque-associated astrocytes and microglia, suggesting that the ECB system might play a critical role in mediating the neuroinflammation events characterising the AD progression[168]. The expression of $CB_2$ receptors, that in normal CNS tissue is low, is upregulated as a response to the microglia activation, that is, as a response to neural damage-provoking events. Conversely, the $CB_2$ receptors activation starts counteracting neuroprotective actions[169,170], including the regulation of calcium homeostasis, mitochondrial functions and control of excitoxicity[87]. Conversely, the upregulation of FAAH in the areas surrounding the neuritic plaques suggests that this enzyme might play a critical role in the production of arachidonic acid, that is, a precursor of prostaglandines synthesis, from the hydrolysis of the substrate anandamide.

On the other hand, recent evidences have shown that, while the activity of AChE progressively decreases with AD progression, BuChE present a completely different trend increasing its enzymatic activity in the late stages of the pathology, and thus might represent a critical target for the treatment of severe forms of neurodegeneration.

Starting from these premises, a novel approach combining the modulation of FAAH activity and the inhibition of BuChE has been proposed as a potential efficient strategy for the treatment of AD.

## *3.1 FAAH as a target for neuroprotection*

### *3.1.1 FAAH characterisation*

Since the first characterisation of FAAH as the enzyme responsible for the oleamide-hydrolase activity[171], a great deal of effort has been put into the characterisation of this enzyme.

Unlike other members of the amidase signature (AS) family, to which it belongs, FAAH is an integral membrane enzyme, characterised by a predicted N-terminal transmembrane domain, which is absent in other AS enzymes. Notably, the deletion of this domain also produced a catalytically active enzyme, which was found to interact with the membrane, even in presence of basic detergents[172], suggesting that the interaction with the membrane is a key element in the catalytic activity of FAAH.

A series of mutagenesis, kinetic and chemical labelling experiments were fundamental to determine S241 as the catalytic serine[173]; other mutagenesis studies revealed that FAAH is characterised by an unusual serine-serine-lysine catalytic triad, consisting of the nucleophilic serine 241 and by S217 and K142. Notably, K142 plays a role both as base and as acid during the catalytic cycle. More specifically, K142 acts as a base maximising the nucleophilic character of the catalytic serine, through the interaction with the bridging serine 217. This model is supported by mutagenesis studies proving that the mutation K142A is sufficient to produce a catalytically inefficient enzyme[174,175], similarly to what has been observed in other hydrolases lacking the activating histidine residue[176,177], and by mechanistic models based on QM/MM computations[178].

At the end of the catalytic process, K142 acts as an acid involved in the protonation of the leaving group during the catalytic hydrolysis of the substrate; this mechanism is impaired in K142A mutants. Interestingly, while the mutant K142E shows a significantly reduced nucleophile strength, and thus a reduced reactivity rate towards compounds that irreversibly block FAAH by forming a stable covalent adduct at S241 (i.e. fluorophosphonate-based compounds), it hydrolyses both amides and esters at the same rate[175]. These lines of evidence point out that FAAH activity is deeply related to the nature of its unusual catalytic triad, and specifically to the presence of K142, whose protonation state rules and coordinates the stages of the nucleophile attack and then of the leaving group protonation

during the catalytic cycle. Consistently with the peculiar architecture of its catalytic triad, FAAH shows an optimum of activity at pH ≈ 9[172,174,179].

### *3.1.2 FAAH structure*

FAAH (Fatty Acid Amide Hydrolase) is a member of the amidase signature sequence enzymes[173] and a key actor among the ECB system, being involved in the deactivation of AEA and of other members of the fatty acid ethanolamide (FAE) family, including palmitoylethanolamide (PEA) and oleoylethanolamide (OEA)[180–184].

To date, a great deal of effort has gone into the characterisation of FAAH structure, leading to the determination of a substantial number of crystal structures that shed light on the architecture of the enzyme.

The first crystal structure of rFAAH (PDB: 1MT5)[185] gave a fundamental contribution to the elucidation of the catalytic site architecture, being co-crystallised with the site-directed covalent inhibitor methoxy arachidonoyl fluorophosphonate (MAFP). FAAH is characterised by a serine-serine-lysine catalytic triad (S241-S217-K142), which in 1MT5 is involved in the formation of a covalent adduct with phosphate group of MAFP (Figure 31).

The enzyme is organised as a dimer, presenting a β-sheet core with 11 strands, enclosed by 24 α helices. Among the helices surrounding the protein core, α18 and α19 form a helix-turn-helix motif that serves as an anchoring domain to the inner side of the cellular membrane, from which FAAH engages its substrate (Figure 31). Notably, the $NH_2$-terminus, which was predicted to form a transmembrane α helix consisting of residues 7-29, but is not present in the crystal structure, would be situated in close contact with helices α18 and α19, providing an additional membrane-interacting domain. A tight hole, which would serve as the entrance for the substrate, is placed near the membrane-binding domain, and represents an amphipathic region, being profiled by lipophilic residues and the charged residues R486 and D403. Following these observation, it has been proposed that the amphipathic aperture might help the recruitment AEA by facilitating the correct orientation of its polar head and, at the same time, provide a privileged interaction site with the phospholipid bilayer.

### *3.1.3 Characterisation of the binding site*

An exhaustive overview of the three-dimensional features of FAAH binding site has been provided by the determination of several crystal structures of the enzyme inhibited by different classes of inhibitors.

In 1MT5, the arachidonic tail of the inhibitor fits a narrowed channel, also named acyl chain-binding pocket (ABP), delimited by the side chain of aromatic and aliphatic residues, and terminating in correspondence of the aperture at the interface with the membrane (Figure 31). Notably, the membrane-facing extremity of the channel is gated by a flexible phenylalanine residue (F432), situated on the helix α18 of the cap domain interacting with membrane. To date, two distinct conformations have been determined by X-ray experiments; in the first conformation (which has been evidenced in 1MT5) the side chain of F432 partially overlaps the aperture towards the membrane, while the lipophilic tail of MAFP occupies the ABP, providing a feasible prediction of the substrate apolar portion binding mode. In the second conformation, which has firstly disclosed in 4HBP[186], F432 is oriented in the opposite direction, allowing the accommodation of inhibitors bearing different and more rigid groups.

While the ABP presents different conformations, limited to the orientation of F432, the binding pocket in proximity of the active site is highly conserved among the different crystal structures. As revealed by X-ray experiments, the catalytic triad residues are oriented in order to maximise the nucleophilic character of the catalytic serine 241. On the other hand, this region is also characterised by an oxyanion hole, lined by the nitrogen atoms of I238 and G239 backbone, which stabilises the negatively charged intermediate generated during the hydrolytic deactivation of the substrate.

From the active site binding pocket, a second channel departs, dividing into two branches.

The first ramification consists of a tight tunnel, delimited at its lower tip by W445. Notably, this cavity has been found to be the binding site accommodating the substituted heteroaromatic portion of several α-keto-heterocycle derivatives co-crystallised with humanised forms of rFAAH[187–191], and has been described as the cleft occupied by the biphenyl portion of the reference FAAH inhibitor URB597[192]. The second branch consists of a larger channel pointing towards the dimerization surface. The hydrophilic character of

this cavity and its aperture towards the cytosol have earned it the name of “cytosolic port”, and suggested the hypothesis that this tunnel might represent an exit route for the ethanolamide after the substrate cleavage and, at same time, an entrance path for water molecules involved in the hydrolytic reaction. The cytosolic port consists of a large tunnel delimited by hydrophilic residues situated on the helix α20 of the second monomer (Figure 31). At the interface between the two monomers, a small aperture provide the entrance/exit path water molecules from the cytosol and the ethanolamide. To date, none of the available crystal structures of rFAAH or humanised rFAAH provides information about the accommodation of ligands within this cavity. On the other hand, targeting this cleft may represent a feasible strategy to design new FAAH inhibitors endowed with higher selectivity.

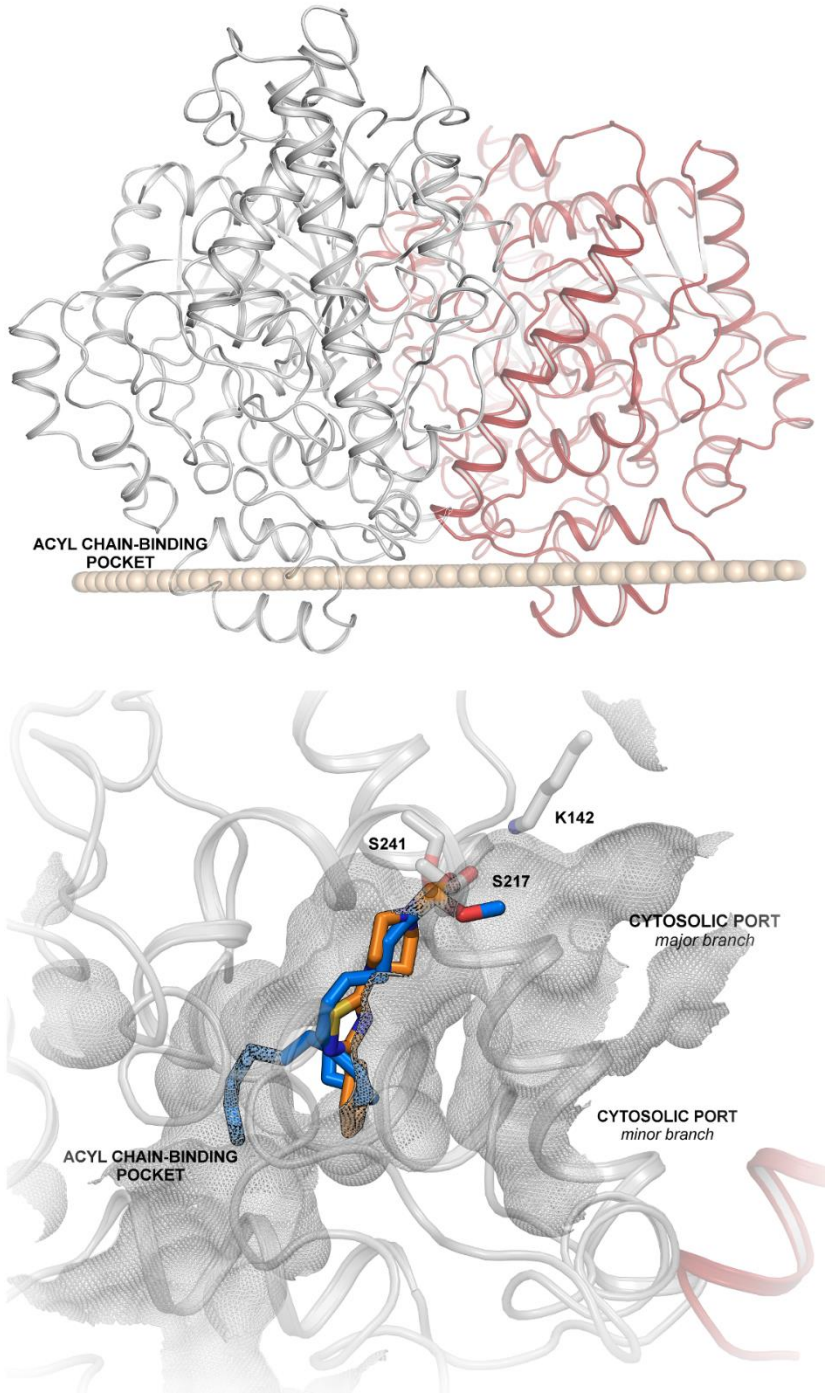


*Figure 31 Upper panel: representation of the FAAH dimer (monomer B, grey cartoon; monomer A, dark red cartoon); the cap domain (helix α18 and α19) is embedded in the membrane (represented in spheres) and is in close contact with the entranced of the acyl chain-binding pocket. Lower panel: detail of the binding site of FAAH in complex with the irreversible inhibitor methoxy arachidonoyl fluorophosphonate (blue carbons) and with a piperazine urea derivative (orange carbons).*

### *3.1.4 FAAH as a pharmacological target: known inhibitors*

The great deal of effort that has been put into the research of novel FAAH inhibitors has provided fundamental information about its role as pharmacological target within the ECB system. Evidences showing that AEA and the other members of FAE compounds mediate anti-inflammatory and analgesic effects strongly encourage the research of novel FAAH inhibitors, endowed with higher selectivity and improved pharmacokinetics and pharmacodynamics profiles.

*Irreversible carbamate-based inhibitors: URB524 and URB597 derivatives*

Starting from the hypothesis that carbamate-based compounds might block FAAH by interacting with the catalytic residue S241, a series of *O*-aryl-*N*-alkylcarbamic acid esters were developed. The first compound disclosed was the *N*-cyclohexylcarbamic acid biphenyl-3-yl ester URB524[193] ($IC_{50}$=63 nM). Experiments, aiming at the evaluation of the effect of substitutions at the meta and para position of the distal phenyl ring, led to the discovery of the reference compound URB597[192]. The introduction of a carbamoyl group at the *meta* position of the distal pehnyl ring led to a relevant increase of inhibitory potency ($IC_{50}$= 4.6 nM), allowing the formation of further polar contacts within the enzyme binding pocket. Notably, X-ray experiments have also provided information about the binding mode of URB597[194], which is covalently bound to S241, with the *N*-cyclohexyl group accommodating within the inner portion of the ABP. URB597 has been proven to be an effective and selective FAAH inhibitor[195], mediating several effects, including the reduction of neuropathic pain[196,197], anxiolytic-like and antidepressant-like effects[198–200], without eliciting the typical cannabinoid-like effects. On the other hand, URB597 is affected by a short *in vivo* half-life, and by an undesired interaction with plasma carboxylesterases. In order to overcome these issues, a second generation of carbamate-based FAAH inhibitors has been developed. This study led to the identification URB694, a para-hydroxyphenyl derivative showing a decreased cross-reactivity towards plasma carboxylesterases and an increased *in vivo* half-life compared to URB597, while maintaining a comparable *in vivo* potency in rats ($ID_{50}$= 0.19 mg/kg for URB597 and 0.16 mg/kg for URB694)[201].

Another *N*-cyclohexyl-carbamate derivative, combining the introduction of a hydroxyl group on the proximal phenyl ring, and of an amide group on the distal ring, URB937, has been developed as a peripherally restricted FAAH inhibitor, in order elucidate the role of peripheral ECB system in the control over pain initiation[202]. URB937 efficaciously inhibits FAAH, and mediates the enhancement of AEA levels related to the attenuation of nociception in several models of rodent models of peripheral nerve injury and inflammation, providing evidences for a promising

alternative approach to the treatment of pain, which would allow to exert antinociceptive effects, while avoiding psychotropic effects related to the central adiministration.

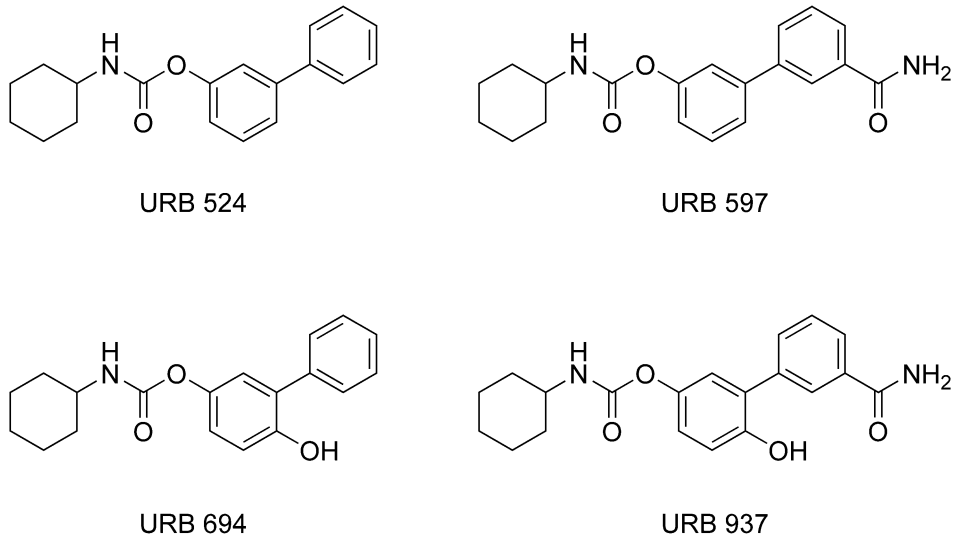


*Figure 32 Chemical structures of carbamate-based FAAH inhibitors.*

*Irreversible inhibitors: aryl urea-based compounds*

Urea-containing compounds were investigated as FAAH inhibitors by several pharma industries; the first ligand belonging to this class was reported by Lilly, showing a good potency ($IC_{50}$=12 nM) and inhibiting FAAH through the formation of a covalent adduct at S241[203]. Despite the high potency, LY-2183240 is characterised by low selectivity over other hydrolases.

Other urea-based compounds have been developed by Sanofi-Aventis, which developed triazolopyridine ureas[204,205]; Takeda[206] and Johnson &Johnson[207] that disclosed piperazine aryl ureas, and Pfizer, that reported piperidine/piperazine urea based compounds[208].

*Reversible inhibitors: α-ketoheterocycles*

The first class of reversible FAAH inhibitors consists of α-ketoheterocycle-based compounds, targeting the catalytic serine 241 and blocking the enzyme activity through the formation of a hemiketal adduct.

Starting from α-ketoxazole-based ligands, different compounds characterised by a α-ketoheterocycle function have been developed as potent and selective FAAH inhibitors, by exploring a series of five- and six-membered monocyclic and bicyclic oleoyl α-ketoheterocycles. Notably, the substitution of the benzoxazole functionality with oxazolopyridines with a fused

increased the potency of this class of compounds, as a consequence of the enhanced electron-withdrawing character. On the other hand, the incorporation of a 2-pyridyl group at the position C4 or C5 of the oxazole ring led to the discovery of potent compounds, including the reference compound OL-135[209,210] ($IC_{50}$=4.7 nM), a potent, selective competitive inhibitor, exerting antinociceptive and anti-inflammatory effects in different preclinical animal models.

Starting from OL-135, a series of structure-activity relationship (SAR) studies were prompted, exploring the effects of modifications of the lipophilic tail[211–213] or of the substituents on the central oxazole ring[214–216]. These SAR studies revealed that lipophilic tail plays is a required feature for potent FAAH inhibitors. Janssen reported a series of OL-135 derivatives characterised by alkylated or acylated *N*-substituted 4-piperidines or 4-propylpiperidines replacing the phenexyl group of OL-135, showing improved enhanced solubility[217]. The fundamental role for the ketone-activating heterocycle was confirmed. Interestingly, compounds bearing a 2-pyridyl-6-carboxylic acid at the C5 position of the oxazole were characterised by increased solubility and potency, related to the presence of the carboxylic group establishing additional polar interactions[218].

Notably, the crystal structure of rFAAH covalently inhibited by OL-135 has been determined, providing the first three-dimensional description of FAAH inhibited by the formation of a stable adduct, mimicking the enzymatic tetrahedral intermediate.

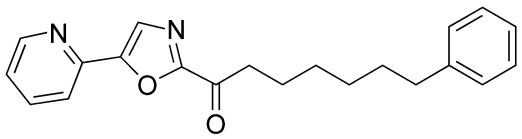


OL-135

*Figure 33 Chemical structure of OL-135*

## *Other reversible inhibitors*

Additional reversible FAAH inhibitors include boronic acids, which may act as transition state analogs, or may inhibit FAAH through the formation of a reversible adduct at S241[219,220].

B-lactams-based scaffolds have also showed activity as FAAH inhibitors, blocking the enzyme through a competitive reversible mechanism[221], and showing selectivity for FAAH over other hydrolases[222].

## *3.2 BuChE as a target for AD treatment*

### *3.2.1 BuChE functions*

Butyrylcholinesterase (BuChE) is a serine hydrolase responsible for the degradation of different choline esters. Despite the existence of this enzyme, which flanks acetylcholinesterase (AChE) in the catalytic deactivation of acetylcholine, has been known for decades[223], the interest for BuChE as a potential target for neural disorders treatment has raised only recently. The reasons of lack of interest that has been characterising this target are to be searched in the wider range of substrates of BuChE compared to AChE, which conversely shows high selectivity for acetylcholine (ACh), and in the high levels of BuChE outside the CNS.

On the other hand, more recent findings have outlined that BuChE is expressed in specific CNS areas and in distinct populations of neurons[224–226], where it plays a role as a regulator of the cholinergic neurotransmission along with AChE[227], and that this enzyme is a key actor in the CNS development[228–230]. Moreover, evidences showing that BuChE activity is altered in several neurological disorders, including AD, have raised BuChE as an interesting target for the treatment of AD symptoms.

Going to details, recent results from histochemical assays revealed that BuChE is primarily expressed in the proximal dendrites of neurons localised in the amygdala and hippocampus, in the thalamus and in the temporal neocortical areas[231]. Notably, in these areas BuChE is able to catalyse the hydrolysis of the ACh surrogate acethylthiocholine. Taken together, all these evidences suggest that BuChE plays a key role in the cholinergic transmission, which is complementary to the actions exerted by AChE. Although BuChE catalyses the hydrolysis of ACh with less efficiency than AChE, it has been proven that ACh levels are increased by the inhibition of BuChE in a dose-dependent manner. Moreover, in the absence of AChE, BuChE compensates for several functions of AChE, including the modulation of the cholinergic system[232]. Recently, it has been found that cortical levels of BuChE are remarkably higher in individuals affected by full-blown AD, and that the expression of the enzyme is associated with neuritic placques and neurofibrillary tangles. Notably, BuChE activity is mainly related to compact and mature placques, suggesting that BuChE has a more relevant role in the events leading to the evolution towards an aggravated form of the

disorder. These lines of evidences suggest that BuChE is a key target in the treatment of AD, especially of the aggravated forms, in which the pool of cholinergic neurons has been severely affected.

### *3.2.2 BuChE structure and structural elements for AChE/BuChE selectivity*

In the last decade, several successful X-ray experiments have elucidated the three-dimensional structure the enzymes responsible for the degradation of acetylcholine, and specifically of human BuChE. BuChE is a member of the α/β hydrolase family, being characterised by a β-sheet core surrounded by α-helices. As revealed by the crystal structure of hBuChe co-crystallised in presence of a molecule of the cholinesterases inhibitor tacrine, the three-dimensional structure of hBuChe highly overlaps the architecture of hAChE[233] (Figure 34). Both the enzymes present an active site characterised by a catalytic triad and a choline-binding pocket placed at the bottom of a narrowed tunnel. As for AChE, hBuChE catalytic triad consists of a nucleophile serine, a histidine and a glutamate residue (S198, H438 and E325, respectively). In close contact with the catalytic serine, the nitrogen atoms of G116 and G117 backbone form the oxyanion hole, which stabilises the negatively charged intermediate during the catalytic cycle.

Similarly to AChE, BuChE is characterised by the presence of a highly conserved choline-binding pocket, buried at the bottom of the active gorge. This portion is occupied by a molecule of tacrine in the crystal structure of hBuChE 4BDS[233], and by a residual choline group in 1P0M[234]. As revealed by the crystal structure of hAChE in complex with donepezil (PDB: 4EY7)[235], the benzylpiperidine head of donepezil perfectly overlaps the tetrahydroacridin system of tacrine in hBuChE. This cleft is lined by W82 (W86 in hAChE), which interacts with the choline ammonium group through a π-cation interaction[234], and W430 and Y440 (W439 and Y449 in hAChE). On the other hand, while the residues involved in the interaction with the choline portion are highly conserved in both the ChEs, the volume of the binding site is reduced in hAChE by the bulky side chain of Y337, which is replaced by A328 in BuChe (Figure 34).

On the other hand, hBuChE presents remarkable differences, limited to the peripheral anionic site (PAS), and to the acyl-binding pocket, which may account for the different selectivity of BuChE towards diverse choline esters[236,234].

The PAS of ChE represents the entrance gate to the active gorge[237], and consists of aromatic and charged residues allowing the interaction with positively charged entities and aromatic portions of known inhibitors such as donepezil, coumarin derivatives, and quaternary inhibitors, icluding gallamine. In hAChE, the PAS consists of Y72, Y124, W279 and W341; the negatively charged D74 occupies a position that is of crucial importance in the binding of charged substrates[238,239] and plays a critical role in the catalytic activity[240]. Notably, the PAS of hBuChE is characterised by a wider aperture, as a consequence of the substitution of Y72, Y124 and W286 with N68, Q119 and A277, respectively (Figure 34).

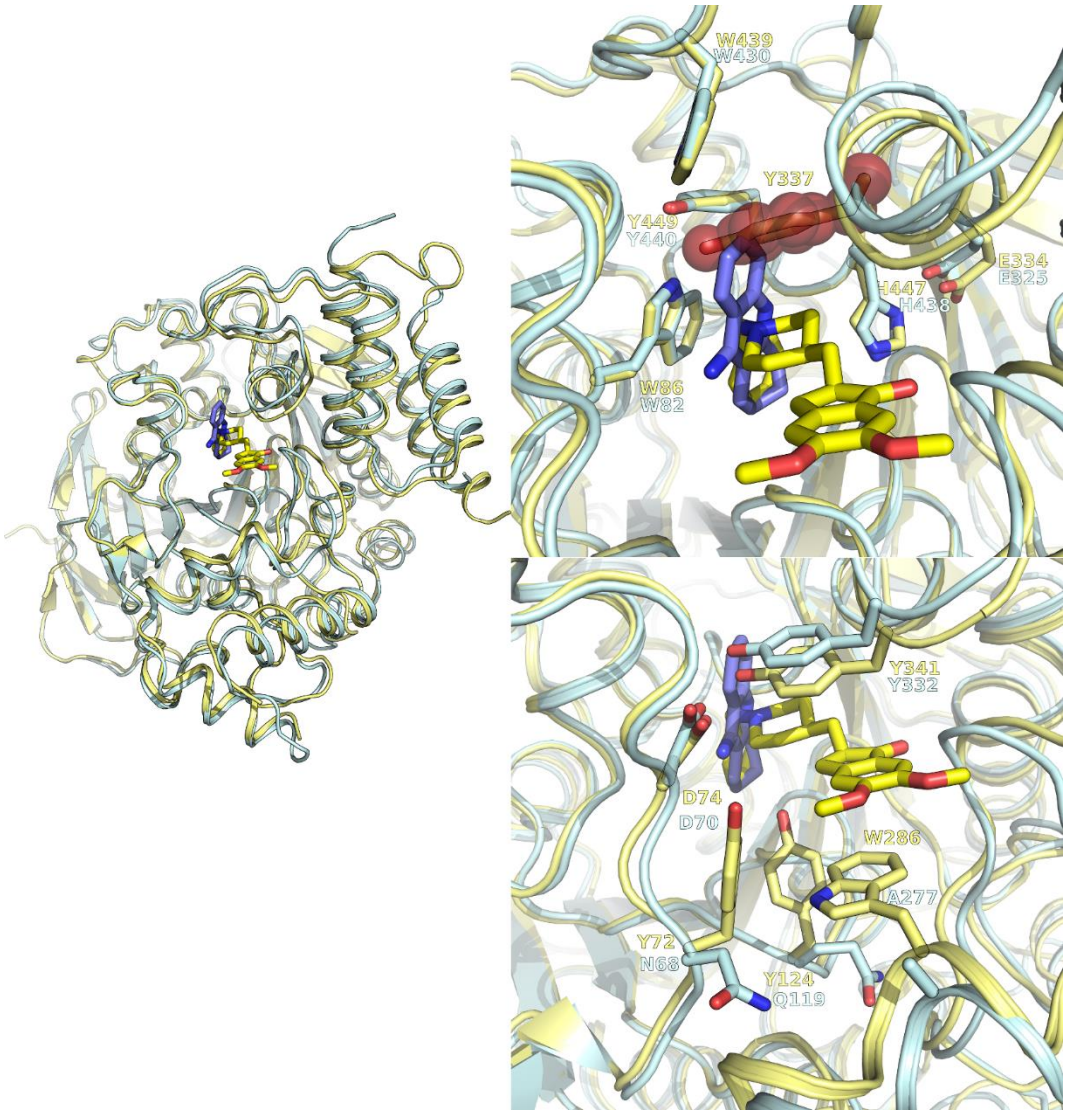


*Figure 34 Comparison of hAChE (light yellow cartoon) and hBuChE (light cyan cartoon) in complex with donepezil (yellow carbons) and tacrine (violet carbons), respectively. Left: overall structure. Right, upper panel: detail of choline-binding pocket of hAChE (light yellow carbons) and hBuChE (light cyan carbons). The side chain of Y337 in hAChE reduces the volume of this cleft (red spheres). Lower panel: detail of PAS of AChE and BuChE.*

The acyl-binding pocket is a hydrophobic cleft accommodating the acyl chain within the binding site. In hAChE bulky residues delimit this portion; W236 (W231 in hBuChE) represents a lower wall of the pocket, while the side chains of F295 and F297 points inside the cavity, reducing the space for the acyl chain. In hBuChE L286 and V288 replace F295

and F297, respectively, providing a wider cleft which may accommodate bulkier ligands and substrates (Figure 35). Notably, the crystal structure of hBuChE inhibited by a selective inhibitor has been recently determined[241] (PDB: 4TPK). The ligand, showing nanomolar potency against hBuChE ($IC_{50}$=2.7 nM), is characterised by an amidic group, targeting the nucleophile S198, decorated with an 1-(2,3-dihydro-1*H*-inden-2-yl)piperidine group, linked to the amide nitrogen atom, and by a naphthalene group. As revealed by the crystal structure, while the indenyl portion and the piperidine ring occupy the lower bottom of the active gorge, where the positively charged nitrogen atom of the piperidine ring may interact with Y332, the rigid naphthalene portion fits the wide BuChE acyl chain-binding pocket, making a perpendicular stacking interaction with W231 (Figure 35). That this cleft is significantly smaller in hAChE provides a plausible explanation for the selectivity of the co-crystallised inhibitor for BuChE and, at the same time, affords important information for the design of selective BuChE inhibitors.

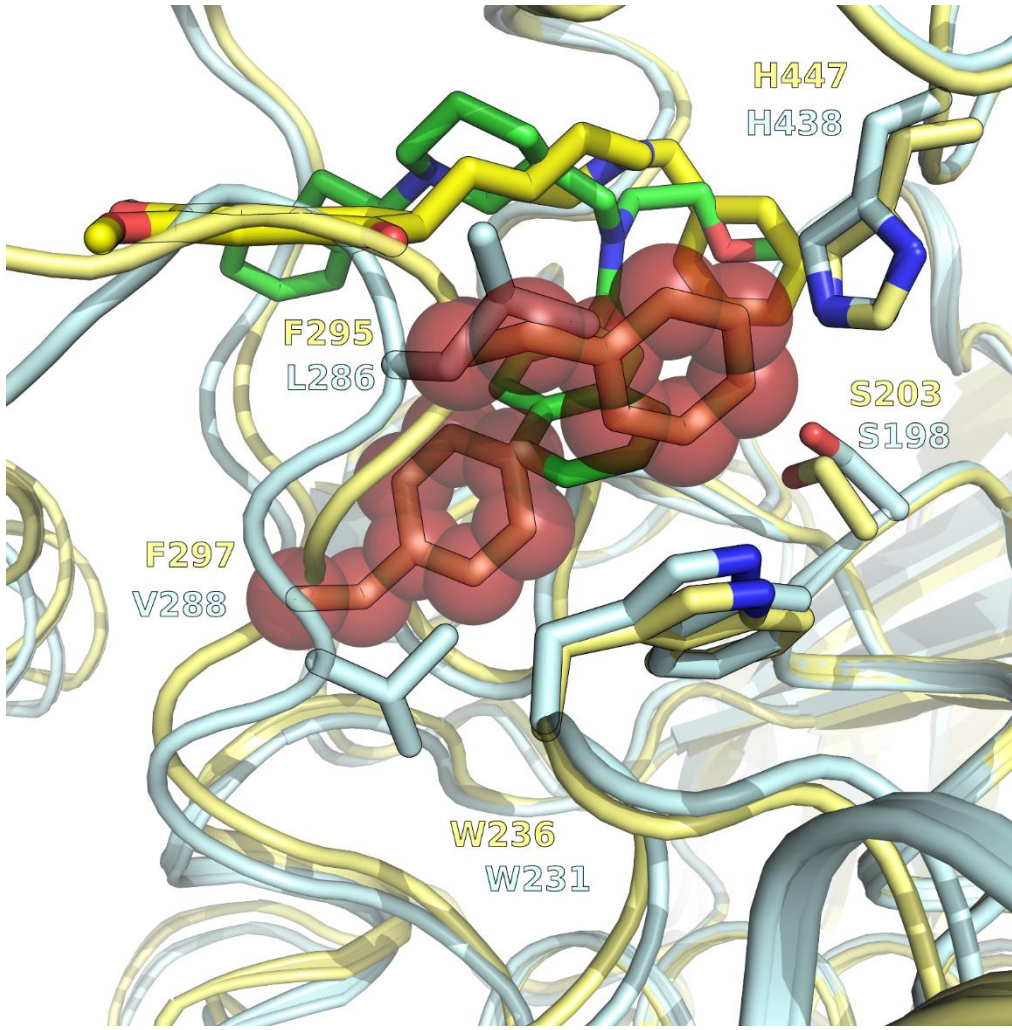


*Figure 35 Detail of the acyl chain-binding pocket of hBuChE (pale cyan carbons) in complex with a selective and reversible inhibitor (4TPK; green carbons) and hAChE (light yellow carbons).*

### *3.2.3 Known ChE inhibitors*

The central role of the cholinergic transmission in the cognitive processes, and evidences outlining that a subnormal cholinergic activity is a hallmark of AD, have raised AChE and, more recently, BuChE as promising target for the AD symptoms attenuation. To date, few ChE inhibitors have been employed in clinical treatment, including tacrine, rivastigmine, galantamine and donepezil. However, the limited efficacy of these compounds and, in certain cases, the observation of severe side effects question their use. On the other hand,

known inhibitors are characterised by low selectivity, or eventually have AChE as preferred target. Recently, a new strategy aiming at hitting different proteins involved in the AD insurgence and progress has been proposed in order to obtain new ChE inhibitors, endowed with improved efficacy and higher selectivity.

*Tacrine and derivatives*

Tacrine (9-amino-1,2,3,4-tetrahydroacridine) is a reversible, non-selective inhibitor of AChE and BuChE, targeting the choline-binding pocket of the enzyme and assuming a binding mode stabilised by an aromatic stacking network that involve the acridine ring and W82. Tacrine is the first approved pharmacological treatment of AD[242]. Nonetheless, the severe hepatotoxicity related to tacrine administration has led to its withdrawal from the market[243,244].

Different strategies have been proposed, in order to design novel compounds with a safer pharmacological profile. The bioisosteric substitution of the quinoline ring by a pyrazolo[3,4-b]pyridine group led to the identification characterised by a significant lower potency, suggesting that the tetrahydroacridine scaffold is required to maintain the inhibitory potency[245]. An alternative approach, aiming at the design of ligands combining a dual action on different binding sites on BuChE and AChE, led to the discovery of homo- and hetero-dimers, targeting both the active and the peripheral sites of the enzyme. Notably, variations in the length of the linker, in the presence and in the position of a protonable amino group or an amide group led to the identification of several inhibitors showing different selectivity and activity towards AChE and BuChE[246–249].

*Rivastigmine and carbamate derivatives*

Rivastigmine (trade name Exelon) is the first compound of the carbamate-based ChE inhibitors[250,251], which block the enzymatic activity through the formation of a covalent adduct between the carbamate group and the catalytic serine. Notably, rivastigmine selectively targets brain BuChE and AChE, limiting the side effects related to the blockade of peripheral acetylcholine degradation. The introduction of bulkier alkyl substituents at the carbamic nitrogen led to the identification of potent and selective inhibitors[252].

*Xanthostigmine and derivatives*

Starting from a xanthone pharmacophore, a novel class of carbamate-based ChE inhibitors has been developed, leading to the discovery of potent and AChE selective compounds[253,254].

*Coumarin derivatives*

Coumarins are naturally occurring compounds, bearing a 2*H*-chromen-2-one scaffold, which exert a wide variety of biological effects, such as anti-inflammatory, hepatoprotective, antioxidant, antitumor and antidepressant activities. Notably, both natural compounds and synthetic coumarin derivatives have been found to efficaciously block the ChE through the interaction with the PAS of the enzyme[255–257]. Following the design of multivalent ligands, different research groups have developed novel derivatives targeting additional binding sites on ChE and showing affinity for other targets.

The reference compound AP2238[258] is a coumarin derivative, characterised by the presence of a chromenonic scaffold endowed by the presence of a benzylamino group linked by a semi-rigid tether. The presence of two functional groups allows the ligand to interact with inner portion of the active gorge (benzylamino moiety) and with the external part of the PAS (coumarin head). While the presence of different portions, able to positively interact with the target, determined an increase in the inhibitory potency, the combination of different functional groups paved the way for the development of further derivatives. For example, the bioisosteric substitution of the chromenone moiety with an indanone core linked to the benzylamino group of AP2238 yielded a new series of derivatives showing a good potency profile and an improved inhibition of AChE-induced Aβ aggregation[259]. More recently, the decoration of the chromenone head with different alkyloxy groups, bearing a basic amino group, has led to the identification of novel coumarin derivatives endowed with a multipotent profile[260]. On the other hand, the insertion of halophenylakylamidic functions at positions 6 and 7 of the coumarin head[261] allowed to couple the anticholinesterase activity to the inhibition of BACE1 (β-site amyloid precursor protein cleavage enzyme), which plays a critical role in the production of the Aβ peptide.

## *3.3 Design, synthesis and biological evaluation of novel ChE/FAAH bivalent inhibitors*

The multifactorial and complex aetiology of Alzheimer's disease urges for the search of a combined therapy, based on compounds endowed with multivalent activity. To this aim, different classes of compounds have been recently developed, yielding compounds combining an inhibitory activity against ChE and BACE1[261], monoamine oxidases[262], serotoninergic receptors[263], NMDA receptors[264].

Recently, a novel class of coumarin and xanthostigmine derivatives, characterised by the presence of a carbamate group, have been developed[265]. Notably, these carbamate-based compounds have shown inhibitory activity against FAAH, which has been found to be overexpressed in specific brain areas of individuals affected by AD.

The results presented in this section are the outcome of a research project in collaboration with the research group of Prof. Rampa at University of Bologna that developed the first class of bivalent FAAH/BuChE inhibitors, aiming at the elucidation of the molecular mechanism of the BuChE selectivity and FAAH activity, and at the rational design of novel derivatives. The research group of Prof. Di Marzo at Institute of Biomolecular Chemistry, National Research Council-Naples has performed the biological evaluation of the compounds under investigation.

### *3.3.1 Characterisation of the first bivalent FAAH/ChE inhibitors*

The compounds taken into account in this study share a phenyl-carbamate group, adopted from the FAAH inhibitor URB597, with an alkyl-amino tether inserted at the *meta* position of the phenyl ring, linking the carbamate group to the xanthostigmine/coumarin head. At the opposite extremity of the bivalent ligands scaffold the carbamate nitrogen is decorated with different lipophilic chains (Figure 36)[265].

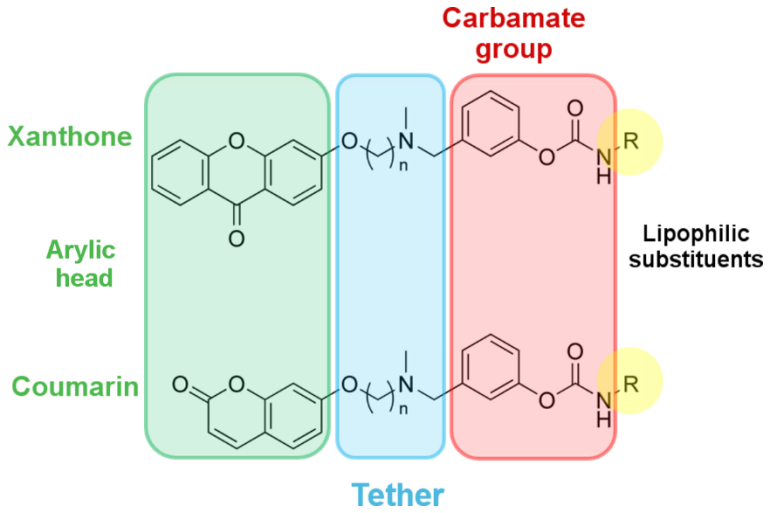


*Figure 36 General structure of carbamate-based xanthone/coumarin derivatives.*

A comprehensive SAR study have elucidated the role of each portion on the inhibitory potency against FAAH and ChE. Notably, among the different aryl groups considered as possible substituents of the arylic head portion, coumarin, xanthone and azaxanthone were preferred. The optimal chain length was of three methylene units; the tether is also characterised by the presence of a basic amino group, which lives in its protonated form at physiological pH. The length of the alkyl chain decorating the carbamate nitrogen atom proved to be of fundamental importance for the inhibitory activity of the compounds, with bulkier and longer chains promoting an enhanced potency against FAAH and ChE.

The biological assays performed to determine the inhibitory potencies against ChE revealed that all the compounds reported block AChE and BuChE in a time-dependent manner, through the formation of a carbamoylated adduct at the catalytic serine. All the compounds were characterised by an increased potency compared to the reference compound rivastigmine, showing potencies ranging from the low nanomolar range for hBuChE to the high nanomolar range for hAChE. Interestingly, all the compounds showed a marked selectivity for hBuChE over hAChE[265].

On the other hand, all the compounds showed FAAH inhibitory activity, with potencies in the submicromolar range improved to the nanomolar range after preincubation[265].

More specifically, compound **9** (Figure 37) was considered the most promising lead compound, showing high potency against hBuChE ($IC_{50}$=1.57 nM) and FAAH ($IC_{50}$=50 nM and 40 nM after preincubation, respectively).

Interestingly, additional biological assays have outlined that the inhibitory potency of this class of compounds strongly depends on the pH conditions. Going to details, the comparison of the data of the reference compound URB597 inhibition activity at pH 7.4 and pH 9 revealed that a decrease of the pH barely affects the potency of the compound. Several lines of evidences show that FAAH has an optimal hydrolytic activity at pH ≈ 8/9, and it is still active at pH 7.4. Reduction of pH makes the neutral inhibitor URB597 slightly (6-fold) less potent, which is probably due to the lower rate of enzyme carbamoylation. On the other hand, the reduction of the pH value was found to be detrimental for the activity of compound **9**, leading to a 22-fold loss of potency. Notably, compound **9** shares the same *O*-phenylcarbamic function of URB597, but presents an additional basic group inserted within the tether linking the carbamate to the coumarinic head (Table 2). The additional loss of potency could therefore be ascribed to higher protonation of this group at lower pH. Thus these data strongly suggest that the neutral form of the bivalent FAAH/ChE inhibitors considered in this study is responsible for the observed inhibitory activity against rFAAH.

Starting from these premises, molecular docking studies were performed on rFAAH and hBuChE, in order to elucidate the molecular mechanism of this class of compounds, and to provide the basis for the rational design of novel derivatives. A particular attention was reserved to the role of the flexible tether and to the neutral amino group inserted on the *meta* position of the phenyl carbamate portion.

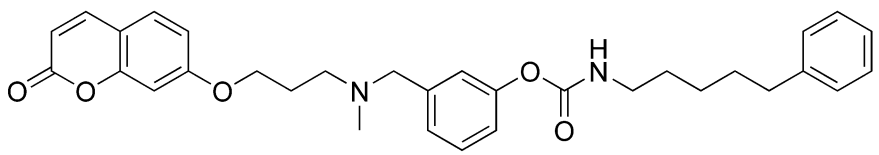


Compound **9**

*Figure 37 Chemical structures of compound **9**.*

| Compound | $IC_{50}$ (nM) | pH value |
|---|---|---|
| **URB597** | 23.51 | 9.0 |
| **URB597** | 140.78 | 7.4 |
| **9** | 183.08 | 9.0 |
| **9** | 4099.10 | 7.4 |

*Table 2 Effect of pH conditions on inhibitory potency of the reference compound URB597 and **9**.*

### *3.3.2 Docking studies on rFAAH*

As it has been already discussed, the binding site of FAAH can be divided in three main clefts. The ABP that in the crystal structure 1MT5 accommodates the lipophilic chain of the irreversible inhibitor MAFP, and, likely, the arachidonic tail of the substrate AEA. The active site, which is characterised by the catalytic triad S241, S217 and K142, modelled in its neutral form. Originating from the active site and extending towards the dimerization interface, the cytosolic port represents a wide cavity, characterised by a more hydrophilic character; notably, in proximity of the catalytic site, this cleft presents a smaller branch, which accommodates the biphenyl portion of the reference compound URB597. Besides, the cytosolic port is also characterised by the presence of threonine residue (T236), which is situated in close contact with the catalytic site and might represent a crucial element in the drug-target recognition mechanisms.

Taking into account the in house biological results providing strong evidences for the influence of pH conditions on the inhibitory potency of this class of bivalent ligands, in this docking study, both the protonated form (which is the most abundant specie at physiological pH) and the neutral form of the basic tether were considered.

#### *Docking of compound **9** reveals the existence of two alternative binding modes*

The docking studies performed of compound **9** in its protonated and neutral form reveal that, this class of compounds occupies the FAAH binding pocket by accommodating the *N*-phenylpentyl chain within the ABP. The lipophilic portion of **9** partially overlaps the space

occupied by the *N*-cyclohexyl moiety of URB597. The *O*-phenyl carbamate group is placed in close proximity to the catalytic triad, and assumes a conformation that favours the formation of hydrogen bonds between the carbamate oxygen and the backbone nitrogen atoms of the oxyanion hole, and between the carbamate nitrogen and the backbone of M191. The carbamate group position is comparable to that assumed by the reference compound URB597. On the other hand, the *O*-phenyl ring assumes different accommodations, determining different orientations of methylamino tether and of the coumarinic head in the cytosolic port. More specifically, the binding modes obtained can be divided in two main families, depending on the accommodation of the tether and of the coumarinic head within the cytosolic port. 1) The first family consists of complexes in which the methylamino tether partially occupies the secondary branch of the cytosolic port, which is occupied by the distal phenyl group of URB597. The coumarinic moiety is thus driven towards the lower part of the cytosolic port cleft. 2) The binding modes clustered in the second family assume an opposite conformation, with the tether and the coumarinic head occupying the upper part of the cleft. Interestingly, both the binding modes were observed for compound **9** in its neutral form and in its charged state. On the other hand, the occurrence of the two distinct binding modes and the docking scores obtained depended on the protonation state of the ligands. Specifically, compound **9** docked in its neutral form prefers the binding mode characterised in the second cluster of poses, with the neutral methylamino group interacting through a hydrogen bond with T236 side chain. Conversely, the protonated form tends to assume a conformation belonging to the first family of binding poses, with the charged methylamino tether partially fitting the minor branch of the cytosolic port and driving the coumarinic head in the lower part of the cleft (Figure 38 and 39).

These results, and the hypothesis that compound **9** binds FAAH in its neutral form, stimulated the design and synthesis of new compounds with an hydrogen bonds-acceptor function.

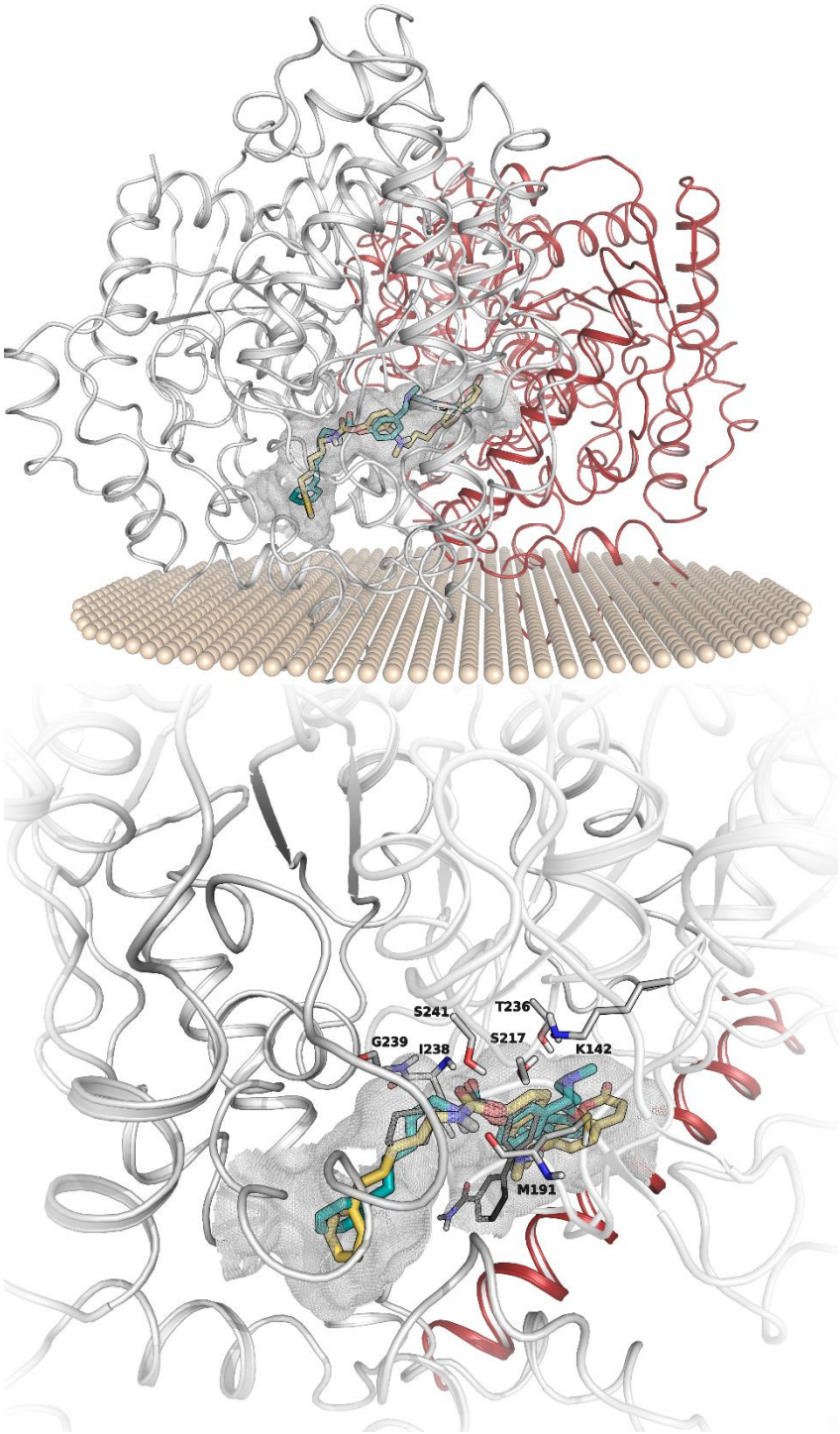


*Figure 38 Upper panel: representation of the rFAAH dimer in complex with compound **9** (chain B, grey ribbons, chain A, dark red ribbons); the profile of the membrane is represented with spheres. Lower panel: different docking poses obtained for compound **9**, docked in its neutral (green carbons) and protonated forms (yellow carbons) compared to the binding mode of the reference compound URB597 (dark grey carbons).*

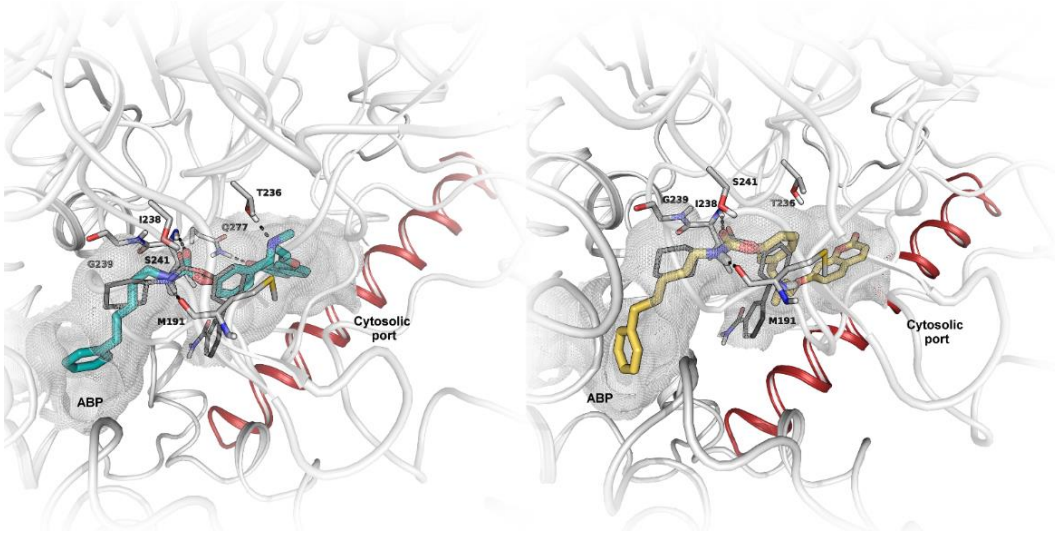


*Figure 39 Left: detailed representation of the binding mode of compound **9** in its neutral form (green carbons) compared to the pose of the reference compound URB597 (grey carbons). The methylamino tether and the coumarinic head occupy the upper part of the cytosolic port, making polar contacts with T236 and Q277. Right: compound **9** docked in the protonated state (yellow carbons) prefers an opposite binding mode, with the coumarinic portion accommodated in the lower part of the cytosolic cleft.*

## *Design of novel (1H-1,2,3-triazol-1-yl)phenyl carbamate derivatives*

In order to elucidate the role of the linker connecting the carbamate group and the coumarinic head, a novel series of 1*H*-1,2,3-triazol-1-yl derivatives was designed. The flexible and basic tether was thus replaced by a more rigid 4-(aryloxymethyl)-1*H*-1,2,3-triazole group, inserted directly or through a methyl spacer at the *meta* or *para* position of the phenylcarbamate group (Figure 40).

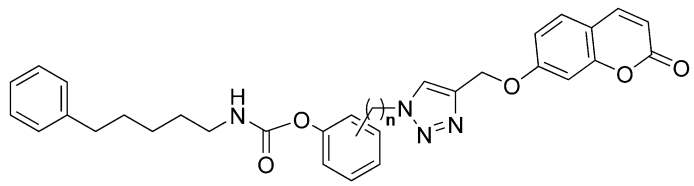


**n**=1, *para* position Compound **10**
**n**=1, *meta* position Compound **11**
**n**=0, *para* position Compound **12**
**n**=0, *meta* position Compound **13**

*Figure 40 General structure of the novel triazole derivatives.*

The docking studies performed for compounds **10-13** revealed the existence of alternative binding modes, comparable to the distinct clusters observed for compound **9**, depending on the position of the triazole linker and on the presence of the methyl group bridging the phenyl carbamate group to the triazole ring.

Compounds **10** and **11**, which are characterised by higher flexibility determined by the presence of a methyl linker between the phenylcarbamate group and the triazole ring assumes docking poses similar to the binding mode preferred by compound **9** in the protonated form. Specifically, the linker fits the minor branch of the cytosolic port, while the position of the triazole group influences the accommodation of the coumarinic head in the lower part of the cytosolic port (Figure 41).

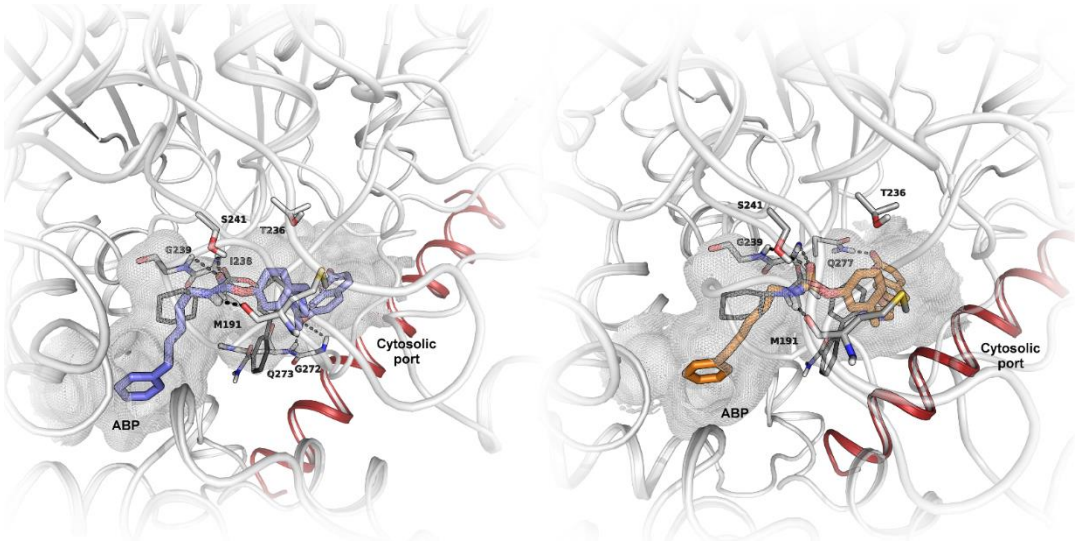


*Figure 41 Left: detailed representation of the binding mode of compound **10** (violet carbons) compared to the pose of the reference compound URB597 (grey carbons). The triazole tether and the coumarinic head occupy the upper part of the cytosolic port, making polar contacts with G272 and Q273 backbone. Right: compound **11** docked in the protonated state (orange carbons) prefers an opposite binding mode, with the coumarinic portion accommodated in the lower part of the cytosolic cleft.*

The reduction of the tether flexibility of compounds **12** and **13**, determined by the direct insertion of the triazole linker on the phenylcarbamate group, hamper the identification of alternative binding modes. The docking solutions obtained are comparable to the second binding modes of compound **9**, preferred in its neutral state, with the triazole tether and the

coumarinic portion occupying the upper portion of the cytosolic port. Notably, the insertion at the *meta* or at the *para* position discriminates binding modes strengthened by the formation of polar contacts between the ligand and the residues lining the binding site. Specifically, while compound **13** occupies the cytosolic port without making any interaction, compound **12** orients the triazole ring in close contact with the side chain of T236, and accommodates the coumarimic head within the cytosolic port making polar interactions (Figure 42).

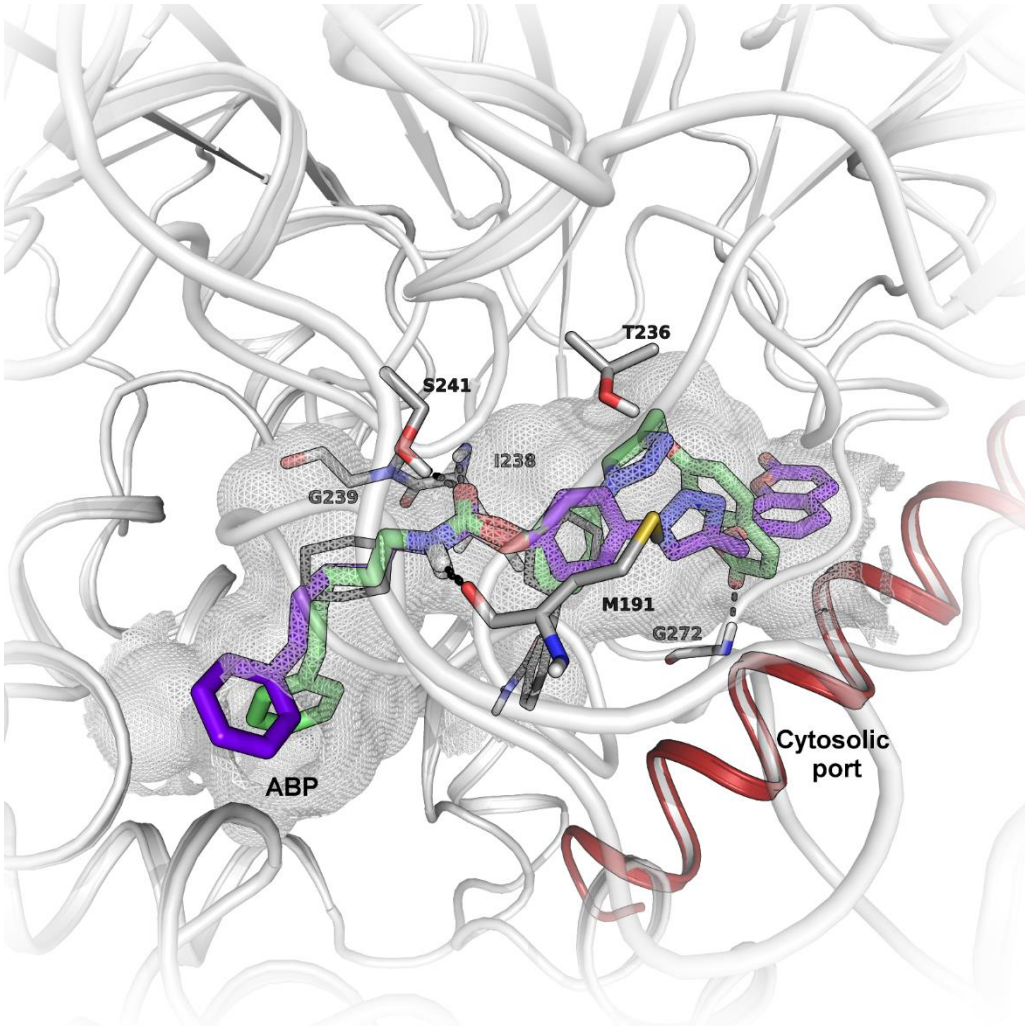


*Figure 42 Details of the binding mode of compound **12** (light green carbons) and **13** (purple carbons) compared to the docking pose of URB597 (grey carbons).*

The biological assays to investigate the biological activity against FAAH of these novel (1H-1,2,3-triazol-1-yl)phenyl carbamate derivatives are still to be completed. However, preliminary results from initial tests provide general information on the trend of this novel series. Notably, all the tested compounds show an improved FAAH inhibitory activity compared to the reference compound **9**, with $IC_{50}$ values ranging from ≈ 28 nM to ≈ 43 nM (results from experiments including the pre-incubation protocol). On the other hand, while the computational models discussed above suggest that the position and the flexibility of the triazole linker may represent elements able to discriminate more potent and promising FAAH inhibitors, the SAR data reveal that all the triazole derivatives inhibit the FAAH enzymatic activity with the same potency.

### *3.3.3 Docking studies on hBuChE*

In order to elucidate the molecular basis for the marked selectivity for hBuChE over hAChE that characterise the coumarin-based carbamate inhibitors discussed in this work, molecular docking studies of compound **9** and of the triazole derivatives (compounds **10**-**13**) were prompted. As it has been discussed above, BuChE and AChE three-dimensional structures share a highly similar architecture, while several differences circumscribed to the acyl chain-binding site and to the peripheral anionic site (PAS; see Figure 34 for details). Notably, as revealed by the available crystal structures, the major differences between the binding site architecture of the two enzymes are limited to the volume of the acyl chain-binding pocket, which smaller in AChE than BuChE, hampering the accommodation of bulky ligands.

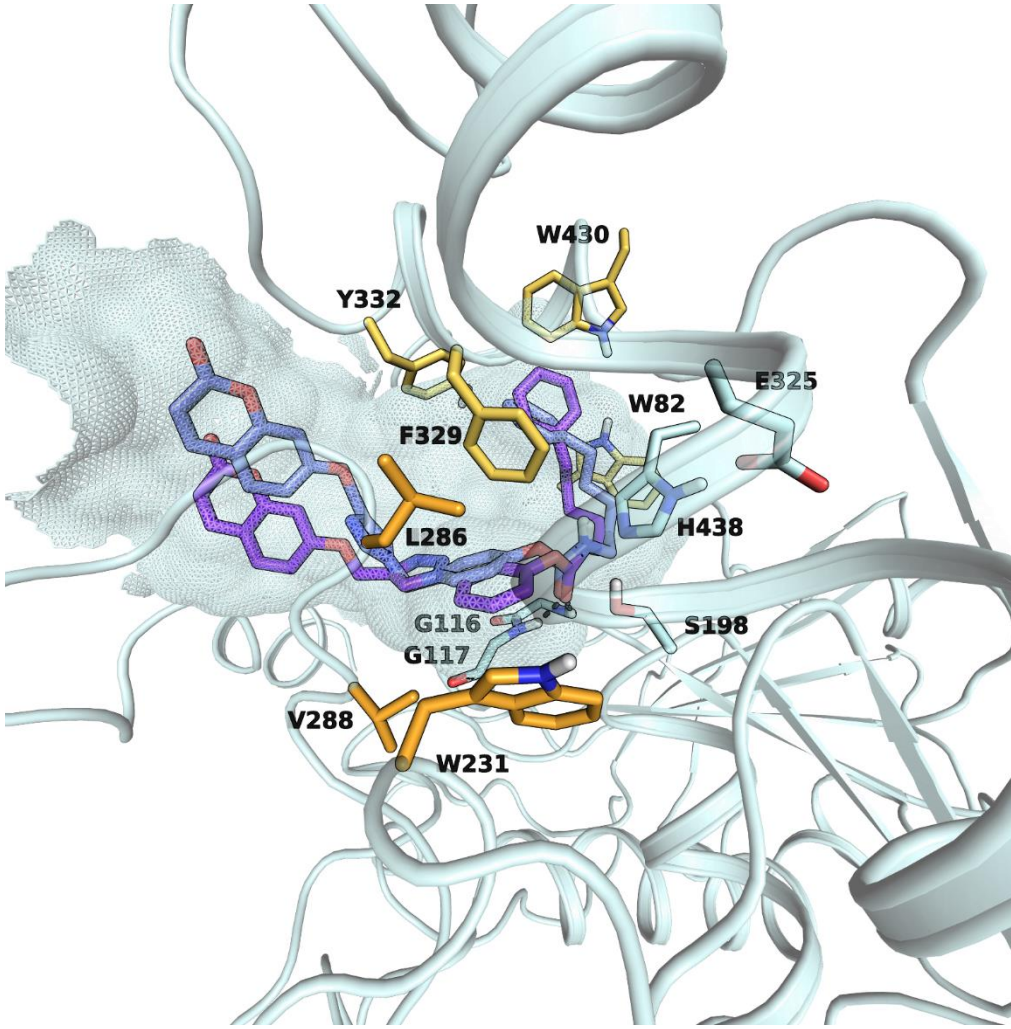


*Figure 43 Detail of the binding mode of compound **10** (violet carbons) and **13** (purple carbons) in the active gorge of hBuChE. The N-phenylpentyl moiety fits the choline-binding site (yellow carbons), while the carbamate function is placed in close contact with the active site residues (light cyan carbons) and makes polar interactions with the oxyanion hole (black dashes). The O-phenylcarbamate portion fits the acyl chain-binding pocket (orange carbons).*

The docking studies revealed that all the compounds under investigation assume a comparable binding mode within the active gorge of hBuChE. The carbamate group is placed in close proximity to active site, with the oxygen atom making hydrogen bonds with the backbone nitrogen of the oxyanion hole residues, assuming a binding mode consistent with the carbamoylating mechanism of action of this class of inhibitors. Following the orientation of the carbamate group, the *O*-phenyl ring fits the acyl-binding pocket, which is

delimited by W231, L286 and V288 of hBuChe. In AChE, F295 and F297 replace L286 and V288, reducing the extent of the cleft. The smaller volume of the AChE acyl chain-binding pocket would hamper the binding of the phenylcarbamate group. On the other hand, while compounds **9**, **10**, **11** and **13** assume binding modes that are perfectly comparable (Figure 43), for compound **12** it was not possible to collect docking poses with an orientation of the carbamate group consistent with the carbamoylating mechanism of action proposed for these compounds. Notably, the steric hindrance of the triazole ring directly inserted at the *para* position of the phenyl ring hampers the optimal accommodation of the phenylcarbamate group within the binding Interestingly, the biological data of the triazole derivatives potency against ChE reveal that compound **12** has no activity towards BuChE nor AChE (Table 3), validating the virtual protocol.

Taken together, these results provide a plausible explanation for the selectivity of these compounds for hBuChE over hAChE (Table 3).

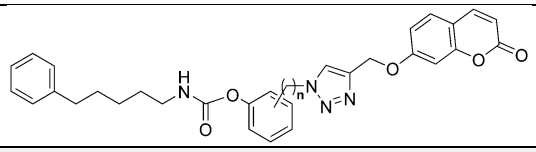

| Compound | Position | n | hAChE $IC_{50}$ (nM) | hBuChE $IC_{50}$ (nM) |
|---|---|---|---|---|
| **10** | *para* | 1 | 255 ± 12 | 1.17 ± 0.12 |
| **11** | *meta* | 1 | 941 ± 106 | 42.7 ± 1.5 |
| **12** | *para* | 0 | 47900 ± 1400 | 1230 ± 90 |
| **13** | *meta* | 0 | 1175 ± 145 | 15.2 ± 1.2 |

*Table 3 Inhibitory activity of triazole derivatives on hAChE and hBuChE.*

The *N*-phenylpentyl moiety completely occupies the choline-binding site that in hBuChE is lined by W82, F329, Y332 and W430. The results of this study are consistent with previously reported data in the literature[266,267] related to ChE inhibition mediated by carbamate based compounds. At the opposite side of the active gorge, the triazole tether and the coumarinic head lay on the surface of the active site gorge wide entrance, partially overlapping the position of donepezil within AChE active gorge (Figure 44).

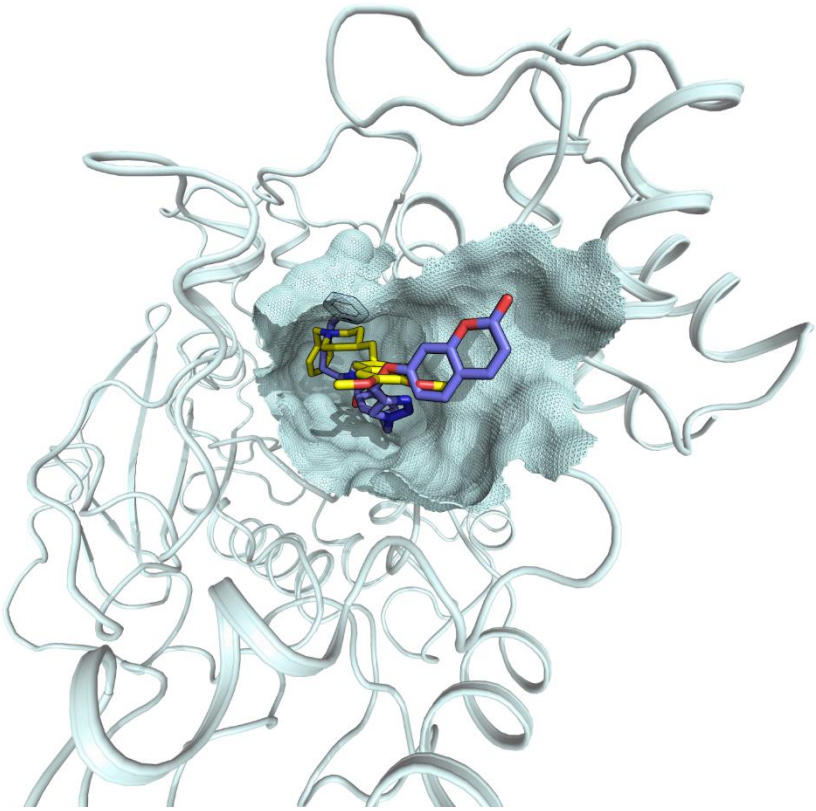

*Figure 44 Binding mode of compound **10** (violet carbons) compared to donepezil (yellow carbons).*

## *Conclusions*

The multifactorial nature of Alzheimer's disease urges for the identification of novel, efficient strategies combining the simultaneous modulation of different targets involved in the pathology progression. To date, several successful examples have been presented in the literature. On the other hand, recent evidences revealed that the endocannabinoid system, and specifically, FAAH and $CB_2$ receptors, play an important role in the neuroinflammation events related to AD. Furthermore, following decades of research devoted to the identification of compounds targeting acetylcholinesterase, the second acetylcholine degrading enzyme, butyrylcholinesterase has been found to exert a fundamental role in the cholinergic transmission during the late stages of the AD progression. In this perspective, the recent identification of carbamate-based coumarinic derivatives, selectively targeting BuChE and FAAH, represents an important step forward in the design of novel multivalent

ligands. In this research project, developed in collaboration with the University of Bologna and the National Research Council of Naples, an extensive study of these new compounds structure-activity relationships has been performed. Computational models provided an explanation for the marked selectivity for BuChE over AChE, and led to the design of novel triazole derivatives, endowed with higher potency against FAAH and increased selectivity for BuChE. Specifically, compound **10**, showing an optimal profile as a bivalent FAAH/BuChE inhibitor, has been found to be a promising scaffold for further optimisation. Finally, while biological data on the inhibitory activity against FAAH are still to be completed, the outcomes of these computational studies disclosed important information on the pharmacophoric space of chemical entities targeting the cytosolic port, providing the basis for the rational design of novel and more selective inhibitors.

## *Computational protocol*

### *Protein Preparation of rFAAH*

The crystal structure of rFAAH covalently bound to the irreversible inhibitor methylarachidonoyl phosphonate (MAP; PDB 1MT5, chain A and B) was prepared using the Protein Preparation Wizard tool provided with the Schrödinger 2014-2 software suite[r]. The homodimer C- and N-*termini* were capped with acetyl and methylamino groups, respectively. The inhibitor molecule was removed, and the missing hydrogen atoms were added. The orientation of hydroxyl groups, thiols, and the conformation of histidine residues were modelled in order to maximise the overall hydrogen-bonding network. Basic and acid residues were modelled in their charged form, with the only exception of K142, included in the catalytic triad, which was maintained neutral. The dimer structure was minimised with the OPLS2005 force field through a first minimisation with constrained heavy atoms, and a second minimisation run with heavy atoms position restrained to a RMSD value of 0.3 Å.

### *Protein Preparation of hBuChE*

The crystal structure of hBuChE in complex with a selective non-covalente BuChE inhibitor (PDB: 4TPK, chain A) was prepared using the Protein Preparation Wizard tool provided with the

[r] Schrödinger Release 2014-2: Schrödinger Suite 2014-2 Protein Preparation Wizard; Epik version 2.8, Schrödinger, LLC, New York, NY, 2014; Impact version 6.3, Schrödinger, LLC, New York, NY, 2014; Prime version 3.6, Schrödinger, LLC, New York, NY, 2014.

Schrödinger 2014-2 software suite[m]. The inhibitor molecule was removed, and the protein was prepared following the procedure described above.

*Induced Fit Docking studies on rFAAH*

The structures of compounds **9**-**13** were built with Maestro 9.8[s] and prepared with LigPrep 3.0[t]. In order to take into account both the protein and the ligands flexibility, the Induced Fit Docking (IFD) protocol within Glide 6.3[u] was applied. The IFD procedure works through the following steps:

1. A softened-potential docking run is performed by reducing the van der Waals radii of both the protein and the ligand. The side chain of selected residues are temporarily mutated to alanine.
2. The resulting complexes are submitted to a protein refinement step, during which the temporarily removed side chains are re-introduced, the side chains of selected residues around the ligand are refined through a conformational search and the overall complexes are minimised.
3. A final docking step is performed, in order to optimise the ligand conformation in the field of the receptor.
4. The complexes are ranked according to the IFD score, which accounts for the ligand-receptor interaction energy, the solvation terms and the receptor strain.

In this work, the grid docking was characterised by a cubic inner box of 20 Å, which defines the dimensions of the search space. In order to extensively sample the space of the binding site, the grid was centred on the position of the co-crystallised inhibitor MAP. The van der Waals radii of the protein and of the ligands non-polar atoms were reduced of a 0.7 and 0.5 factor, respectively. The side chain of L278, which hinders the accommodation of the tether, was temporarily mutated to alanine. Hydrogen bonds constraints were imposed between the carbamate oxygen of the ligands and the backbone nitrogen of I238 and G239, and between the carbamate nitrogen atom and the M191 backbone. The complexes obtained were submitted to the refinement step; the L278 side chain was re-introduced, and the side chains in a shell within 5 Å within each ligand, excluding the residues of the catalytic triad, were sampled. In the last step, van der Waals radii

[s] Schrödinger Release 2014-2: Maestro, version 9.8, Schrödinger, LLC, New York, NY, 2014.
[t] Schrödinger Release 2014-2: LigPrep, version 3.0, Schrödinger, LLC, New York, NY, 2014.
[u] Small-Molecule Drug Discovery Suite 2014-2: Schrödinger Suite 2014-2 Induced Fit Docking protocol; Glide version 6.3, Schrödinger, LLC, New York, NY, 2014; Prime version 3.6, Schrödinger, LLC, New York, NY, 2014.

were reinstated to the original value, and the ligands were optimised within the complex. The top-ranked complexes according to the IFD score were finally minimised with the OPLS2005 force field implemented in Macromodel 10.4[v], applying the Polak-Ribiere conjugate gradient method to a convergence threshold of 0.05 kJ $mol^{-1}Å^{-1}$. During the minimisation, the ligands and residues within 10 Å from them were free to move, while the backbone of other residues was kept fixed.

*Docking studies on hBuChE*

All the compounds structures were built in Maestro 9.8[n] and optimised using LigPrep 3.0[o].

The docking studies were performed using Glide 6.3[p]. The docking grid was characterised by a cubic inner box of 16 Å, centred on the position of the co-crystallised inhibitor. Other settings, including the van der Waals radii, were maintained to their default value. The complexes obtained were then ranked according to the Emodel scoring function, which accounts for the internal strain energy of the model, the energy grid score and the binding affinity predicted by the GlideScore[268,269]. The top-ranked poses were then submitted to minimisation using the OPLS2005 force field within MacroModel 10.4[q] applying the Polak-Ribiere conjugate gradient method to a covergence treshold of 0.05 0.05 kJ $mol^{-1}Å^{-1}$. During the minimisation, the ligands and residues within 8 Å from them were free to move, while the backbone of other residues was kept fixed.

[v] Schrödinger Release 2014-2: MacroModel, version 10.4, Schrödinger, LLC, New York, NY, 2014.

# APPLICATION OF MOLECULAR MODELLING STUDIES TO THE SEARCH OF NOVEL PROTEIN-PROTEIN INTERACTION INHIBITORS FOR ANTICANCER TREATMENT AND STEM CELLS APPLICATIONS

# 4. The Hippo pathway

In the last decades, a growing interest has been raising on the search of pharmacological tools for the control of stem cells proliferation and differentiation, looking for the identification of potential chemical modulators promoting tissue repair and regeneration events, to be introduced in the innovative field of regenerative medicine. The identification of cellular signalling pathways and the characterisation of the proteins involved in the regulation of genic transcription is thus of straightforward importance in this perspective. Signalling pathways regulating the cellular proliferation and, more specifically, their deregulated or altered mechanisms, might also represent a critical target for the treatment of cancer.

The Hippo pathway is an emerging growth-regulating and tumour suppression signalling pathway, which is also implicated in the regulation of stem cell functions and in the differentiation of different progenitor cell types. Evidences showing that the deregulation of mechanisms governing the transmission of the signals is implicated in the onset of several human malignancies have recently disclosed this pathway as promising target for cancer treatment.

## *4.1 Overview of the Hippo pathway*

The principal role of the Hippo pathway is to negatively regulate the genic transcription by controlling the nuclear translocation of its downstream effectors, that is, the transcriptional co-activators YAP (Yes-associated protein) and TAZ (transcriptional co-activator with PDZ-binding motif)[270]. If activated, the Hippo pathway works through a cascade of phosphorylating events, which has, as a final effect, the blockade of YAP and TAZ. Conversely, the turning off the pathway allows the nuclear translocation of YAP and TAZ that promote the genic transcription through the formation of a protein-protein complex with the transcription factor TEAD (Figure 45).

The Hippo pathway functions thus consist in transmitting signals from the cell membrane to the nucleus, *via* the mutual interaction and activation of several components, including serine/threonine kinases and scaffolding proteins[271].

### *4.1.1 Components of the Hippo pathway*

The Hippo pathway was first characterised in *Drosophila melanogaster* as a complex pathway regulating the cellular growth and proliferation[272–274]. Since the discovery of the Hpo kinase, which earned the name of "Hippo" to this signals-transmitting system[273], the identification of several additional components of both the *D. melanogaster* and the mammals pathways has shed light on the architecture of this complex signalling network, which integrates different upstream inputs from the membrane to the nucleus.

Going to details, the core of the Hippo pathway comprises two highly conserved serine/threonine kinases, known as MST1 and MST2 (mammalian STE20-like protein kinase 1 and 2)[272,275], which represent the first intermediary in the signalling transduction. Notably, MST1 and MST2 co-localise with filamentous actin structures[276], which is suggestive of a reciprocal influence between the upstream regulator of the hippo pathway and the elements characterising the cellular architecture. Active MST kinases phosphorylate SAV1 and MOB1A/B, which play a key role in the engagement of LATS1/2 by MST[277]. Interestingly, external factors, such as NF2/Merlin, interact with LATS, promoting its MST-mediated phosphorylation and activation[278], suggesting that the Hippo pathway is highly sensitive to the modulation mediated by different upstream regulators. As a further proof of the intensive exchange of regulatory signals between Hippo and other signalling pathways, LATS1/2 phosphorylation can also be mediated by two groups of MAP4Ks (mitogen-activated protein kinase)[279,280]. The Phosphorylated LATS1/2 subsequently undergo an autophosphorylation-dependent activation which finally determines the phosphorylation of the transcriptional co-activators YAP and TAZ. These events lead to the cytoplasmic retention, which is mediated by the interaction with 14-3-3σ[281–283], or the ubiquitination and β-TRCP-dependent degradation of YAP/TAZ[284–286]. This cascade of events thus determines the blockade of YAP and TAZ, hampering their translocation in the nucleus. At the same time, when the Hippo pathway is activated, TEADs form protein-protein complexes with transcription cofactor VGL4 (vestigial-like protein 4) that suppresses the expression of genes regulated by TEAD[287,288] (Figure 45). The Hippo pathway-upstream effectors are thus to be considered negative regulators of genic transcription, blocking the nuclear function of the YAP/TAZ-TEAD complex and promoting the cytoplasmic deactivation of the transcriptional cofactors.

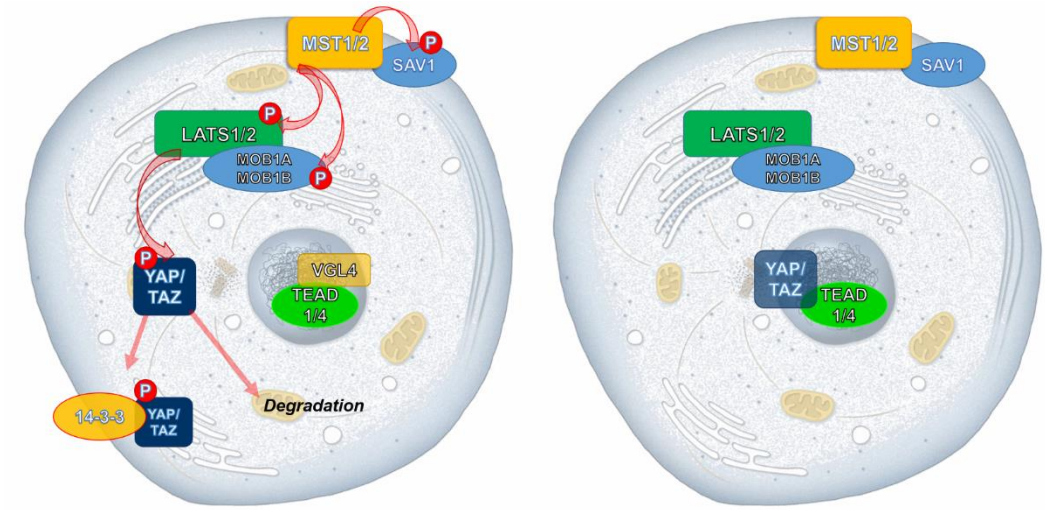


*Figure 45 Left: the activated Hippo pathway promotes a phosphorylation cascade (red arrows) that determines the cytoplasmic retention (mediated by the interaction with 14-3-3σ) or the ubiquitination-dependent degradation of YAP and TAZ. Right: the suppressed Hippo pathway allows the nucleus translocation of YAP and TAZ and their interaction with the transcription factor TEAD.*

### *4.1.2 Regulation of the Hippo pathway activity*

While the activity of each component is rigidly and mutually regulated within the Hippo cascade, this signalling pathway is also controlled by several upstream mechanisms that operate in an interconnected way. In mammals, structural elements (i.e. the actin cytoskeleton, protein complexes that rules the cellular polarity and the adherens junctions) play a crucial role in the regulation of Hippo activity. Being involved in the cellular growth control, the Hippo pathway functions are strongly affected by the physical and mechanical properties of the cell-surrounding environment. For example, the high cell density and the cell-cell contacts limit the proliferation and cell growth *via* Hippo-mediated mechanisms[289–291]. Rho-GTPases-mediated actions and the effects of cytoskeleton are known to play a critical role on YAP and TAZ regulation, although controversial data have not elucidated yet to what extent the kinases-cascade of the Hippo pathway is involved in this event.

As revealed by recent studies, the Hippo pathway is affected by several hormonal cues, which regulate YAP/TAZ-mediated effects by interacting with G protein-coupled receptors. In this perspective, the discovery that lysophosphatidic acid (LPA) and sphingosine-1-

phosphate (S1P) activate and promote YAP and TAZ activity through the interaction with GPCRs (i.e. LPAR and S1PR) represented a milestone in the comprehension of the upstream regulation of Hippo. More specifically, it has been outlined that Rho-GTPases-mediated responses determine an inactivation of LATS, and thus promote the nuclear translocation of YAP/TAZ *via* the modulation of actin cytoskeleton. On the other hand, glucagon and epinephrine activate $G\alpha_S$-coupled GPCRs, promoting the LATS-dependent YAP inactivation. Interestingly, the Frizzled GPCRs (class F GPCRs) and their ligands, including Wnt proteins such as Wnt5a/b, have been recognised as partners of Hippo in the regulation of cell differentiation and migration, unveiling a cross talk between the two pathways. Notably, the Wnt signalling pathways consist of different signal-transducing pathways, also known as canonical and non-canonical. More specifically, Wnt5a/b are involved in the non-canonical Wnt signalling pathway, which promotes the activation of YAP and TAZ while antagonizing the canonical Wnt/β-catenin activation.

### *4.1.3 Hippo pathway deregulation in cancer*

Several lines of evidences correlate a sub-normal Hippo pathway activity, that is, a hyperactivation of YAP/TAZ with tissue overgrowth and development of different types of malignancies. In several animal models, the overexpression of YAP or the loss of the control exerted by MST and LATS determine an abnormal tissue growth in liver and heart, as a consequence of an uncontrolled cellular proliferation[292–297]. On the other hand, in skin and intestine active YAP promote an expansion of the stem cells pool, blocking the differentiation processes while avoiding the uncontrolled tissue growth[298–300]. Furthermore, among the genes, whose expression is started by the transcriptional complex TEAD-YAP, cyclins, growth factors and inhibitors of apoptosis play a critical role in cellular proliferation and tissue expansion.

These evidences support the role of YAP and TAZ as key actors in the onset and progression of specific tumours. Abnormally increased nuclear levels of YAP and, at a lower extent, of TAZ have been described as a hallmark of different human cancers, such as liver, lung, breast, skin, colon and ovarian cancer[301–305]. While a complete comprehension of the mechanisms laying behind the YAP-dependent tumorigenesis still has to be achieved, it has

been proposed that YAP and TAZ deregulation might promote cell proliferation and survival, and the achievement of specific cancer cells characteristics, including the inhibition of senescence, drug resistance and cancer stem cells properties. Notably, this latter aspect has emerged from studies revealing that the specific over-activation of TAZ stimulates the proliferation of stem cells *in vitro*, and promotes the growth of stem-like cell populations in breast cancer models[306]. Interestingly, the participation of YAP/TAZ in tumorigenesis may also involve the promotion of the epithelial to mesenchymal transition (EMT) and the loss of cell polarity, which represent a typical hallmark of the main high-grade tumours and of metastases[306,307].

YAP/TAZ and more specifically their complexes with the transcriptional factor TEAD, which is required for the initiation of genic expression, represent thus a critical target for the treatment of cancer. Evidences form *in vivo* and *in vitro* animal models show that the control of YAP activity is a key step in limiting the tumour progression and in the prevention of malignancies onset. For example, the genic ablation of NF2, which is known to promote the LATS-dependent YAP/TAZ deactivation, is sufficient to induce liver cancer formation. On the other hand, the simultaneous deletion of the gene encoding for YAP completely suppresses the tumour formation[308]. Moreover, the expression of a dominant negative form of TEAD, lacking the DNA binding domain, counteracts the tumour formation in $NF2^{-/-}$ mice[309]. The reduction of human YAP levels mediated by siRNA or shRNA is related the slowing and arresting of cancer cells proliferation *in vitro* and in xenograft assays[310–314]. On the other hand, while the suppression of YAP/TAZ activity has been proven to be an effective way to reduce the cancer cells metastatic potential and to inhibit the proliferation of cancer stem cells, the complete suppression of YAP/TAZ functionalities may produce severe side effects, such as the sensitisation to WNT-mediated hyperplasia[315,316]. In this perspective, the protein-protein complex TEAD-YAP represents a more attractive target in order to exert an effective counteraction to the uncontrolled tumour cell proliferation.

### *4.1.4 Hippo pathway and regenerative medicine*

The Hippo pathway functions have been related to the stem cell activation and progenitor cell expansion mechanisms, and to the regulation of the equilibrium between progenitor and stem cells, raising YAP and TAZ as possible promotor of tissue repair and regeneration.

Recent studies outlined that YAP directly activates the expression of genes that promote pluripotency in murine embryonic stem cells[317]. Moreover, YAP and TAZ enhance progenitor cells expansion, while inhibiting the differentiation mechanisms, in liver, intestine, pancreas, heart, skin and CNS[296–300,318,319]. Nonetheless, it still has to be elucidated whether these effects, observed *in vitro*, can be generalized to tissue-specific stem cell populations *in vivo*, and other crucial elements need further investigation in order to achieve a full comprehension of the Hippo pathway role in tissue repair. For example, it is not clear whether progenitor cell expansion is related to the inhibition of differentiation processes or to a return to a more primitive and undifferentiated state of specific cell populations[317].

YAP and TAZ thus hold the balance of power in the regulation of stem cell fate, while negative regulators within the Hippo pathway (i.e. MST and LATS) act as a barrier against the maintenance of the pluripotency condition[320].

## *4.2 Therapeutically relevant targets among the Hippo pathway and known inhibitors*

In the last decade, the Hippo pathway has been described as a complex signals-transmitting machinery, able to regulate crucial events in tissue regeneration and, on the other hand on the uncontrolled growth of cancer cells. The suppression of YAP/TAZ activity is a promising strategy for the treatment of cancer, while pharmacological tools inhibiting the Hippo pathway may represent a fundamental milestone in the regenerative medicine field.

*Kinases as a target for YAP/TAZ activity regulation*

Small molecules targeting MST and LATS, which restrain YAP/TAZ in their cytosolic inactive form, might represent useful compounds for the enhancement of YAP/TAZ-TEAD-dependent effects. MST and LATS inhibitors would have an important role in regenerative medicine, and may be used for *ex vivo* stem cells expansion and *in vivo* tissue repair. Although an organoruthenium derivative has been recently presented as the first potent MST1 inhibitor[321],

whose effects on YAP/TAZ activity are still to be investigated, the development of Hippo kinases inhibitors is hindered by selectivity issues, and by the absence of crystallographic structures, which would help the rational design of selective MST or LATS inhibitors.

*GPCRs-mediated upstream regulation*

Lysophosphatidic acid (LPA) and sphingosine-1-phosphate (S1P) are known to exert an upstream controlling function on Hippo by activating $G\alpha_{12/13}$-coupled GPCRs, and promoting the nuclear localisation of YAP and TAZ. Notably, while $G\alpha_{q/11}$, $G\alpha_{12/13}$ and $G\alpha_{i/o}$ mediate a positive effect on YAP, $G\alpha_s$ coupled receptors mediate an inhibitory modulation on YAP. $G\alpha_s$ agonists may thus promote YAP inactivation. Notably, dopamine receptors agonists, including epinephrine and glucagon, promote the activation of the Rho-GTPase-mediated control of LATS, involving the actin cytoskeleton[322,323]. Evidences showing that adrenaline increases YAP phosphorylation in a mouse model *in vivo* further support that GPCRs modulators might be used in therapeutic applications.

*YAP/TAZ-TEAD protein-protein complex*

Being directly involved in the genic expression mechanisms, the YAP/TAZ-TEAD complex is an attractive anticancer target. Evidences showing that single point mutations of specific residues, that are critical for the formation of the protein-protein complex, completely abolish the YAP/TAZ-mediated cell proliferation strongly support the search of small molecules targeting the YAP-TEAD complex[324]. A recent HTS campaign coupled to a luciferase reporter/Gal4-fused TEAD system led to the discovery of an inhibitor of TEAD-mediated genic expression. The lead compound is an oxime derivative characterised by a 9*H*-fluoren-9-one scaffold, bearing two symmetric piperidinyl-sulfonyl moieties (C108, Figure 46)[325]. While the mechanism laying behind C108-mediated effects is still to be elucidated, it has been hypothesised that this compound promotes YAP ubiquitination. Notably, cells treated with different doses of C108 in presence of the proteasome inhibitor MG132 maintain the levels of endogenous YAP, providing evidences for a C108-dependent induction of YAP degradation. C108 moreover blocks melanoma and lung adenocarcinoma progression in xenograft mouse model by inducing cancer cells apoptosis.

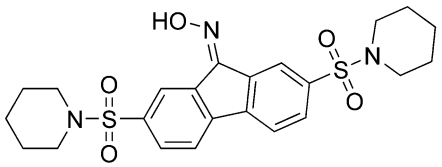


**C108**

*Figure 46 Chemical structure of compound C108.*

Verteporfin (VP, tradename Visudyne, by Novartis) and protoporphyrin IX (PPIX) (Figure 47) have been identified as inhibitors of the YAP-TEAD-mediated gene expression[309]. VP and PPIX are porphyrin derivatives, characterised by aromatic heterocyclic molecules bearing four modified pyrrole units, connected through methine bridges at their α-carbon sites. As revealed by co-immunoprecipitation assays, VP and PPIX block the formation of the YAP-TEAD complex, with VP showing > 50% protein-protein interaction inhibition at 2.5 μM. Notably, VP has been marketed as a photosensitizer in photodynamic therapy of neovascular macular degeneration, activated by laser light and generating reactive oxygen radicals that eliminate abnormal blood vessels. On the other hand, light activation is not required in the events leading to the YAP-TEAD inhibition. Co-immunoprecipitation assays also revealed that VP selectively binds YAP; while the mechanism of VP-mediated blockade is not elucidated yet, it has been proposed that a VP-induced alteration of YAP conformation inhibits the formation of a stable protein-protein complex *in vitro*. VP effects without light activation have been evaluated on human retinoblastoma cells[326]. This study reveals that VP affects cancer cells growth and viability, encouraging the further development of VP as YAP-TEAD interaction inhibitor. On the other hand, fundamental information about the binding mode of VP is still lacking, hampering a full comprehension of the inhibition mechanism and the design of novel compounds mimicking VP interaction with YAP.

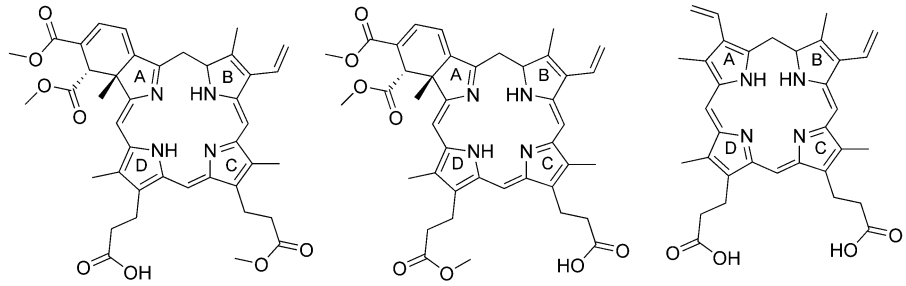


*Figure 47 Chemical structures of VP (left) and PPIXP (right).*

## *4.3 Targeting the YAP-TEAD complex*

Several lines of evidence have revealed in the last decade that the Hippo pathway, and specifically the downstream effectors YAP/TAZ and TEAD, represent a critical element to achieve a full comprehension of the mechanisms ruling the stem cells fate, and of the events leading to the transformation of normal cell populations into tumour cells and cancer stem cells. In this perspective, the recent determination of the three-dimensional structure of the YAP-TEAD complex and mutagenesis studies aiming at the identification of the fundamental interaction site on TEAD and YAP have provided information of extraordinary importance, which also provide the basis for the rational design of selective YAP-TEAD inhibitors.

### *4.3.1 Insight into the YAP-TEAD complex*

TEAD represents the main transcriptional factor mediating the biological effects of YAP and TAZ. In mammals, four members of TEAD family (TEAD1-4) have been identified sharing an sequence identity ranging from 61% to 73%[327]. TEADs N-terminal domain contains a conserved TEA domain, mediating the recognition and interaction with DNA elements in the promoter region of target genes. NMR experiments have revealed that the TEA domain is characterised by a three-helix bundle fold, bearing a bipartite nuclear localisation signal (NLS)[328]. The C-terminal region of TEADs comprises the structural elements involved in the recognition of YAP and TAZ, and in the formation of the protein-

protein complex. Mutagenesis studies have revealed that the mutation of specific residues on TEAD and YAP interacting surfaces are sufficient to abolish completely the formation of a stable protein-protein complex. Moreover, luciferase reporter assays have shown that the formation of the YAP-TEAD complex is required for YAP-dependent gene transcription (13-71). A similar functional relationship involving TAZ and TEAD has been outlined, and interestingly, amino acid residues that have been proven to be critical for YAP interaction with TEAD are conserved in TAZ.

The three-dimensional structures of human TEADs in complex with YAP (TEAD1; PDB 3KYS)[329] and in its unbound form (TEAD2; PDB 3L15)[330] reveal that the YAP-binding domain (YBD) is characterised by two β-sheets packing against each-other. This compact structure, representing the core of the TEADs YBD, is enclosed by two distinct helix-turn-helix motifs, consisting of helices α1/2 and of α3/4, respectively, situated on perpendicular planes in TEADs surface. Notably, helices α3 and α4 form a hydrophobic cleft, which interacts with a helix portion of YAP (helix α1 in 3KYS), through the formation of hydrophobic contacts. TEAD-YBD is characterised by several highly conserved residues, which comprise amino acids forming a hydrophobic cleft on helices α3/4 and residues localised on a solvent-exposed region of the apo TEAD2 (PDB 3L15). Notably, among these set of conserved residues, Y421, situated on the β-core of TEAD1 (PDB 3KYS) and corresponding to Y442 of TEAD2, is mutated to histidine in individuals affected by a rare eye disorder, known as Sveinsson's chorioretinal aptrophy[331]. The mutation of Y421 is sufficient to disrupt the YAP-TEAD complex, thus hampering the YAP mediated cell proliferation.

The crystal structure of TEAD in complex with its partner YAP provides fundamental information on the nature of this particular protein-protein interaction. As revealed by X-ray experiments, YAP surrounds the TEAD YBD, interacting with it through three distinct binding motifs. A β strand, consisting of YAP residues 52-57, represents the first binding element, interacting with TEAD1 β7 through the formation of hydrogen bonds (Figure 48). A series of conserved hydrophobic residues form YAP helix α1 (residues 61-73), which is responsible for the second major network of interactions stabilising the protein-protein complex. Conserved L65, L68 and F69 of YAP, forming the LXXLF motif, fit the hydrophobic cleft delimited by F329, Y361, F365, K368, L369, L372, V381 and F385 of

TEAD1 α3 and α4 creating a network of van der Waals interactions that stabilise the YAP-TEAD complex (Figure 48). A short, flexible linker comprising residues 81-85 and characterised by a PXXΦP motif connects the YAP helix α1 to the third binding element. This region is characterised by a twisted-coil structure, also named Ω-loop motif, which tightly binds the TEAD surface. The three YAP interacting motifs thus bind TEAD in a concerted way. Moreover, while the PXXΦP motif does not directly interact with TEAD surface, evidences showing that the mutation of a proline residue abolishes the formation of the protein-protein complex in *D. melanogaster* suggest that this loop may play a crucial role in maintaining an optimal Ω-loop conformation, promoting an effective binding. On the other hand, while TAZ lacks the PPXXΦP-containing loop, a computational model of its structure suggests that TAZ residues 24-56 form a Ω-loop[327,332], comparable to that observed in the crystal structure of YAP. On TEAD surface, the third interaction surface is represented by a wide and flat cavity, characterised by hydrophobic residues, which line the most part of the cleft wall. Residues E254, D264 and Y421 on TEAD surface form two polar sites, delimiting the two opposite border of TEAD binding site, providing a fundamental binding site, which strengthen the protein-protein complex by interacting with R89 and S94 of YAP, respectively (Figure 48).

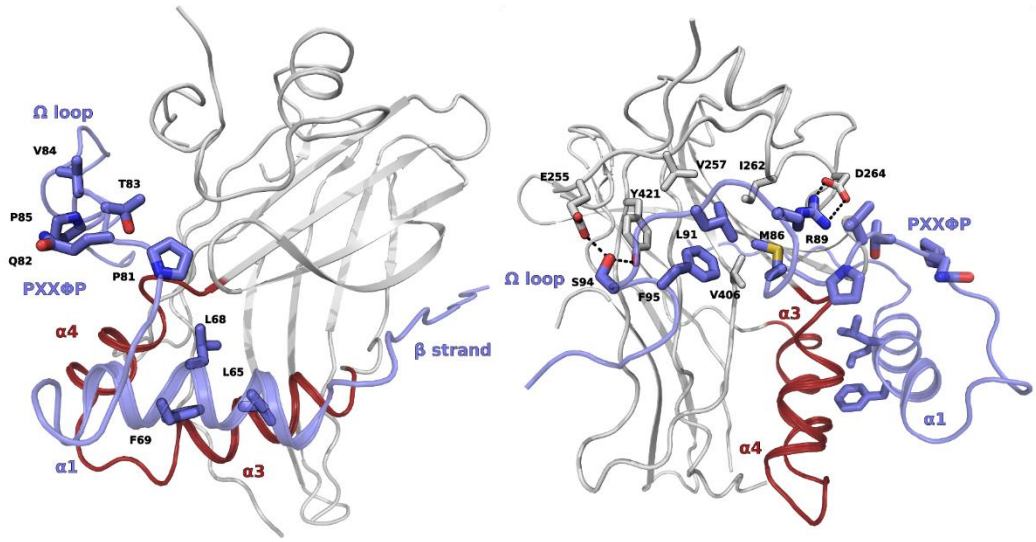


*Figure 48 Left: Crystal structure of the hYAP-TEAD complex (PDB 3KYS); the β strand, the helix α1 and the PXXΦP motif of YAP (light blue cartoon) are represented (light blue carbons). Residues L65, L68 and F69 of YAP mediate the hydrophobic interactions with an apolar cleft on TEAD surface, delimited by α3 and α4 (dark*

*red cartoon). Right: detail of the interaction between the YAP Ω-loop (light blue cartoon and carbons) and the surface of TEAD (grey cartoon and carbons).*

### *4.3.2 The YAP Ω-loop is a key actor in YAP-TEAD complex*

While the analysis of the three-dimensional structure of the YAP-TEAD complex have disclosed three different binding sites involved in the protein-protein interaction, mutagenesis studies, including GST pull-down assays on individual YAP mutants have prompted fundamental information about the different role of the three binding motifs in YAP. Going to details, the complete ablation of β1 (residues 50-59) has a barely effect on its binding to TEAD, suggesting that this portion has a minor role in the formation of the protein-protein complex. Similarly to what observed for the binding motif 1, mutation of interacting surface 2 residues (i.e. L68A and F69A) scarcely influences the affinity of YAP for TEAD.

On the other hand, mutagenesis studies unveiled a more detailed picture of the binding interaction mediated by Ω-loop of YAP. This portion fits a shallow pocket, lined by I262, V257 and V406, which make multiple van der Waals contacts with YAP M86, L91 and F95 side chains. This interaction is strengthened by the formation of hydrogen bonds between YAP R989 and TEAD D264, and by interaction between YAP S94 and TEAD Y421 and E255. Notably, the YAP mutants S94A, F96A, M86A, R89A, L91A and F95A show a significant decrease of binding affinity for TEAD, hampering the formation of a stable complex[329]. As a further proof of the prevalent role exerted by Ω-loop in the formation of the YAP-TEAD complex, functional assays evaluating the ability of the YAP-TEAD complex to bind to a luciferase reporter revealed that single mutations of YAP Ω-loop residues abolish the formation of a functional YAP-TEAD complex[329]. Taken together, these results strongly outline that, while the concurrent binding of the three YAP interaction surfaces is required for the formation of a stable protein-protein complex, the specific interaction between the YAP Ω-loop and the hydrophobic cleft of TEAD surface has a key role in the binding process. This particular protein-protein complex thus represents a promising target for the rational design of selective YAP-TEAD interaction inhibitors.

In this perspective, the recent discovery of a potent cyclic peptide mimicking the Ω-loop able to inhibit the YAP-TEAD complex[333] is a fundamental breakthrough for the

identification of important pharmacophoric elements. Truncation studies coupled to alanine scan performed on the TEAD-binding domain of YAP provided information about the optimal length of the synthetic macro-peptide. Different mutations were also evaluated, in order to obtain active parent peptides of YAP, endowed with higher affinity. Interestingly, a key element in the identification of a potent inhibitor was the constraining of the peptide structure in a locked closed conformation, able to mimic the Ω-loop of YAP. Notably, R87 and F96 are in close contact, allowing the formation of a cation-π interaction stabilising the Ω-loop. Mutagenesis studies revealed that although R87 and F96 are not directly involved in the protein-protein interaction, the single mutation of these residues is sufficient to reduce YAP affinity for TEAD. This suggested that R87 and F96 might have a role in stabilising YAP in its active conformation. A macro-cyclisation synthetic strategy led to the identification of a closed peptide, in which a homocysteine and a cysteine residue, involved in the formation of disulfide bond, replace R87 and F96. In order to enhance the peptide affinity, several mutations were performed, including the substitution of M86 with a *meta*-chlorophenylalanine, the mutation of L91 to a norleucine and of D93 to alanine, leading to a 1500-fold increase of potency with respect to the parent $YAP^{84\text{-}100}$ peptide fragment (Figure 49).

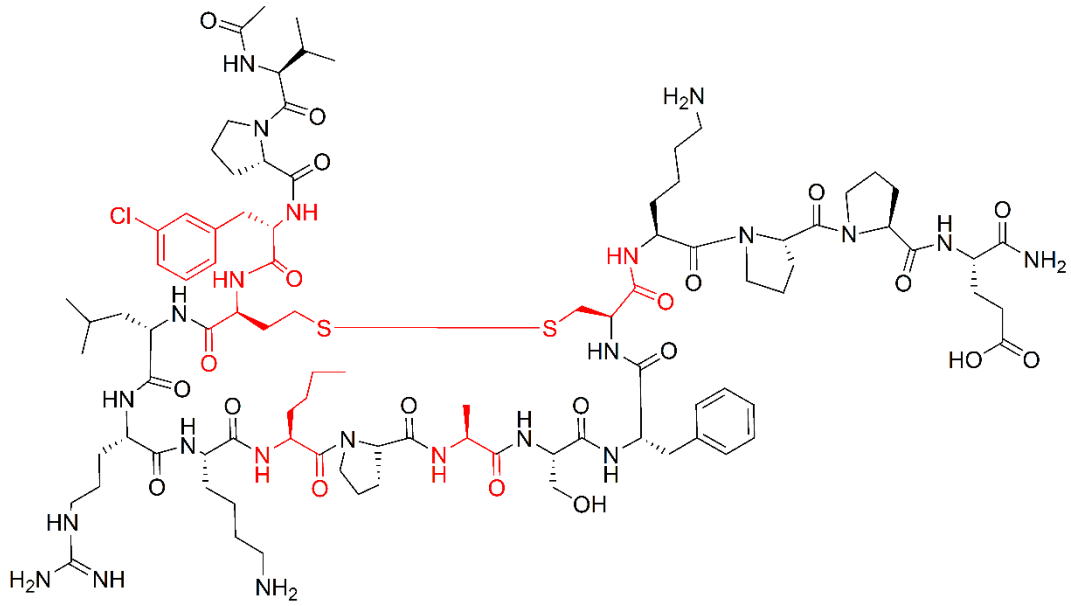

*Figure 49 Chemical structure of the synthetic macro-peptide mimicking the Ω-loop of YAP (residues 84-100), locked in a closed conformation by the formation of an internal disulfide bond between R87 and F96, respectively mutated to cysteine and homocysteine. Additional mutations were introduced in order to improve the binding affinity to TEAD. Mutated residues are depicted in red.*

X-ray crystallographic experiments were performed, in order to evaluate the conformation of engineered YAP mutants characterised by a "locked" Ω-loop, stabilised by a disulfide bond across mutated R87 and F96 (Figure 50).

Interestingly, the designed peptide reported and other derivatives have been proven to be effective YAP-TEAD inhibitors *in vivo* in a xenograft mouse model[334].

Taken together, these results provide critical information for the rational design of small molecules, able to reproduce the fundamental interactions required for the formation of the YAP-TEAD complex.

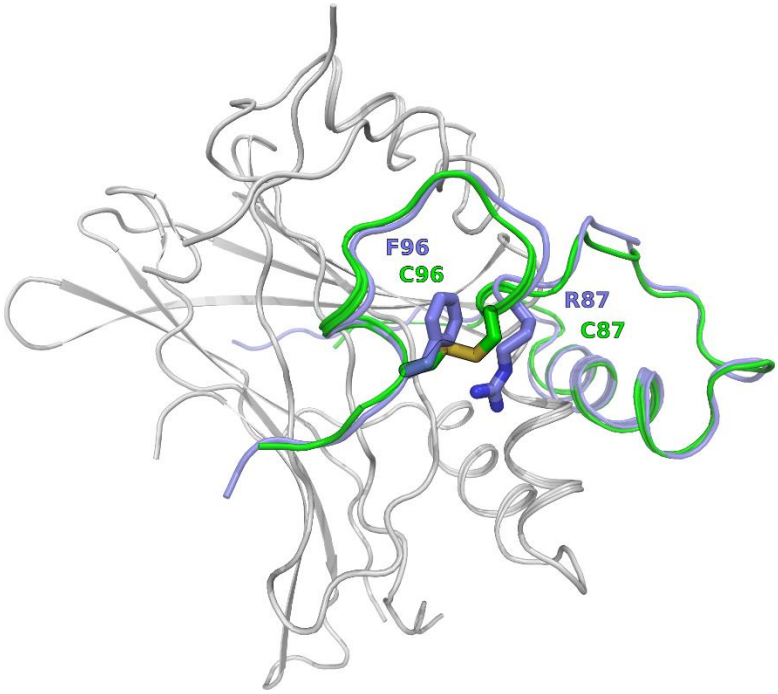


*Figure 50 Comparison of the crystal structure of TEAD (grey cartoon, PDB 3KYS) in complex with hYAP (light blue cartoon, PDB 3KYS) and with engineered hYAP (green cartoon, PDB 4RE1). The substitution of hYAP F96 and R87 (light blue carbons) with two cysteine residues (green carbons) stabilises the restrained conformation of the Ω-loop.*

## *4.4 Virtual screening study of potential YAP-TEAD inhibitors*

In the last decade, a great deal of effort has been put into the comprehension of the mechanisms ruling the growth-control pathway Hippo. Specifically, a clearer picture of the role of the downstream effectors YAP/TAZ and of their complexes with the transcriptional factor TEAD has emerged, providing the basis for the understanding of the molecular mechanisms laying behind the YAP-mediated stem/cancer cell fate control. In this perspective, the recent determination of the crystallographic structures of the YAP-TEAD complex, and the identification of cyclopeptide compounds as potent inhibitors of this interaction, have prompted the basis for the search of new small molecules inhibiting the YAP-TEAD activity. The identification of novel molecules endowed with higher affinity and selectivity for the protein-protein interaction, coupled to an improved drug-like pharmacokinetic profile, would represent a significant milestone in the field of cancer treatment and, at the same time, would represent an important pharmacological tool useful for the evaluation of YAP-mediated activity on different stem cell populations.

In this project, a virtual screening campaign, aiming at the identification of novel leads as potential YAP-TEAD inhibitors, has been performed. The absence of small molecules selectively targeting the YAP-TEAD interaction, and the lack of information about the molecular mechanism laying behind the modulatory activity exerted by known inhibitors prevented the application of a traditional approach, based on the search of novel lead compounds starting from a pharmacophore model built on known active molecules. On the other hand, the combination of different information, obtained from mutagenesis studies, X-ray crystallographic experiments and biological data allowed to set up a computational protocol that has been used to screen a commercially available library of compounds.

### *4.4.1 Evaluation of the interaction between TEAD and a known macro-peptide inhibitor*

As already discussed, a cyclic macro-peptide, derived from the truncation of YAP Ω-loop and from the mutation of specific residues, has been presented as the first potent and selective YAP-TEAD interaction inhibitor.

In this work, docking studies and MD simulations have been coupled, in order to evaluate the structural features of the TEAD-peptide complex.

*Building the TEAD-peptide complex*

A model of a truncated YAP peptide, comprising the residues of the Ω-loop (residues 84-100), was built. R87 and F96 were replaced with a homocysteine and a cysteine residue, respectively, which were modelled as involved in the formation of an internal disulfide bond, leading to the formation of a cyclic peptide (Ω-peptide). Moreover, M86, L91 and D93 were mutated to norlecucine (Nle), *meta*-chlorophenylalanine (3-Cl-Phe) and alanine, respectively, in order to reproduce the specific single point mutations related to the increased binding affinity.

Notably, the computational model obtained unveiled that bulkier and more hydrophobic substituents, such as Nle91 and 3-Cl-Phe86, occupy the wide hydrophobic cleft on TEAD surface. More specifically, 3-Cl-Phe86 accommodate within a small and deeper sub-pocket lined by residues K265 and E383 on one side and by residues K289 and E408 on the opposite side. Notably, the binding mode is strengthened by a double cation-π interaction between residues K265 and K289, and the aromatic ring of 3-Cl-Phe86 (Figure 51). On the other hand, the binding mode reproduced the polar interactions between S94 of YAP and Y421 and E255 of TEAD, and between R89 of the YAP and D264 of TEAD, which are known to be crucial for the formation of the protein-protein complex (Figure 51).

In order to evaluate the dynamical stability of the TEAD- Ω-peptide complex, a Molecular Dynamics simulation of 50 ns was performed. Notably, the analysis of the RMSD measured throughout all the simulation time revealed that the complex TEAD-peptide is characterised by a high conformational stability. The fundamental hydrophobic and polar interactions were maintained throughout all the simulation, further confirming the high stability of the complex. Specifically, the hydrogen bonds between S94 and Y421, and between R89 and D264 were stable during the MD simulation. On the other hand, the 3-Cl-Phe86 residue preserved its initial conformation, maintaining the hydrophobic interactions with I262 and V406, as well as the cation-π contact with K265 and K289 on TEAD surface.

Taken together, the results of this preliminary study offer a plausible computational model explaining the molecular basis for the enhanced binding affinity that characterises the reference macro-peptide inhibitor. On the other hand, the dynamical stability of the key elements in the complex formation provides further information that have been used for the identification of the pharmacophore model.

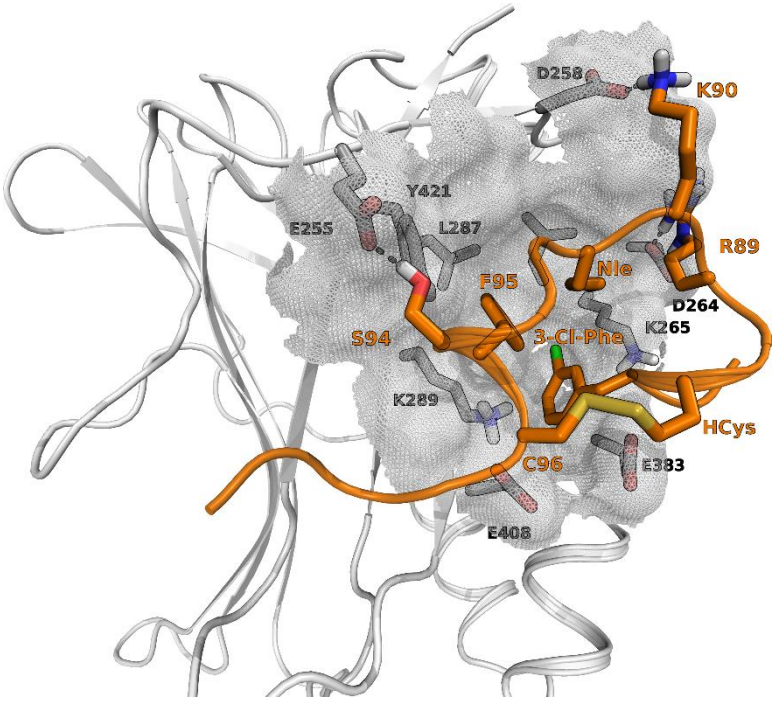


*Figure 51 Detail of the binding mode of the Ω-peptide (orange cartoon and carbons) on TEAD surface (grey cartoon and carbons). S94 makes hydrogen bonds with Y241 and E255, while a saline bridge is formed between R89 and D264. The apolar side chains of F95, Nle and 3-Cl-Phe point towards the hydrophobic cleft on TEAD surface. The interaction of 3-Cl-Phe with TEAD is further strengthened by cation-π interactions with K265 and K289.*

### *4.4.2 Virtual screening study for the search of potential YAP-TEAD interaction inhibitors*

The complexity of the protein-protein interactions chemical space makes the search and the development of small molecules targeting protein complexes a major challenge in medicinal chemistry. To date, the most PPI inhibitors used in clinic are biologics, comprising humanised monoclonal antibodies and synthetic peptides characterised by various length

and size. On the other hand, the use of biologics involve serious drawbacks, including the complex production procedures, the low bioavailability, and the high costs of manufacture. In this perspective, the identification of small, non-peptide molecules targeting PPI is a compelling need.

A major issue concerning the design of PPI inhibitors rises from the existence of a shift between the specific chemical features required to match the inherent topological characteristics of PPI and the chemical space delimited by traditional chemistry rules, including the Lipinski's rule of five[335], the Pfizer's 3/75[336] or the GSK's 4/400[337]. An efficient binding to a protein-protein surface interaction indeed demands ligands endowed with a marked lipophilic character, high molecular weight, higher number of aromatic features as well as of hydrogen bonds-donor/acceptor groups, enhanced number of rotatable bonds and an extended topological polar surface area[338,339].

### *Preparation of selected chemical libraries*

In this work, two libraries of commercially available compounds have been submitted to a virtual screening campaign aiming at the identification of novel small molecules targeting the YAP-TEAD protein-protein interaction. The ChemDiv-PPI and the eMolcules libraries were selected as chemical collections endowed with medium-high molecular weight molecules, bearing chemical features that have been reported as critical for an efficient binding to protein complexes. The libraries were filtered according to molecular weight and presence of hydrogen bonds-donor/acceptors. Moreover, in order to eliminate compounds characterised by an inherent reactivity, and showing a non-specific activity in different assays (Pan Assay Interference Compounds-PAINS)[340,341], molecules presenting highly reactive groups were filtered out.

The ligands surviving the preliminary filter were prepared, in order to generate three-dimensional conformations and to generate the plausible protonation state at physiological pH.

*Pharmacophore-based screening of chemical libraries*

In order to identify small molecules able to target the TEAD surface, hindering the interaction between the YAP Ω-loop and its hydrophobic counterpart on TEAD, the prepared compounds were submitted to a pharmacophore-based screening, aiming at the retention of ligands matching the features that are predicted to be beneficial for the binding.

Following the results of the MD simulation on the TEAD-peptide complex, and considering the mutagenesis data from the literature, different pharmacophore models, built on the Ω-loop of the modelled peptide, were evaluated. More specifically, two distinct pharmacophore models were hypothesised, combining different features from the Ω-peptide structure.

The first pharmacophore model comprises a hydrogen bond-acceptor, corresponding to the hydroxyl group of S94 of YAP/Ω-peptide, the aromatic ring and the hydrophobic group represented by the chlorine atom of 3-Cl-Phe96 of the Ω-peptide. This pharmacophore model privileges the identification of compounds able to interact with the polar button of Y421 and, at the same time, to overlap the accommodation of 3-Cl-Phe within the small cleft delimited by K265 and K289 on TEAD surface (Figure 52).

The second pharmacophore model consists of the same hydrogen bond-acceptor feature characterising the first model, a hydrophobic group for the side chain of Nle and a hydrogen bond-donor feature on the guanidinium group of R89. This pharmacophore model privileges the identification of wider compounds, presumably characterised by a higher molecular weight, able to match pharmacophoric features spanning within the volume of interest (Figure 52).

The first pharmacophore model has been applied to screen the ChemDiv-PPI library, which after the preliminary filtering comprises ligands with a molecular weight ranging from 100 to 900.

Conversely, the second pharmacophore model was used to filter the eMolecules library.

The filtered structures were finally submitted to a docking run on TEAD surface, and the obtained poses were ranked according to their predicted binding affinity, as calculated by the Glide GScore[268,269] scoring function.

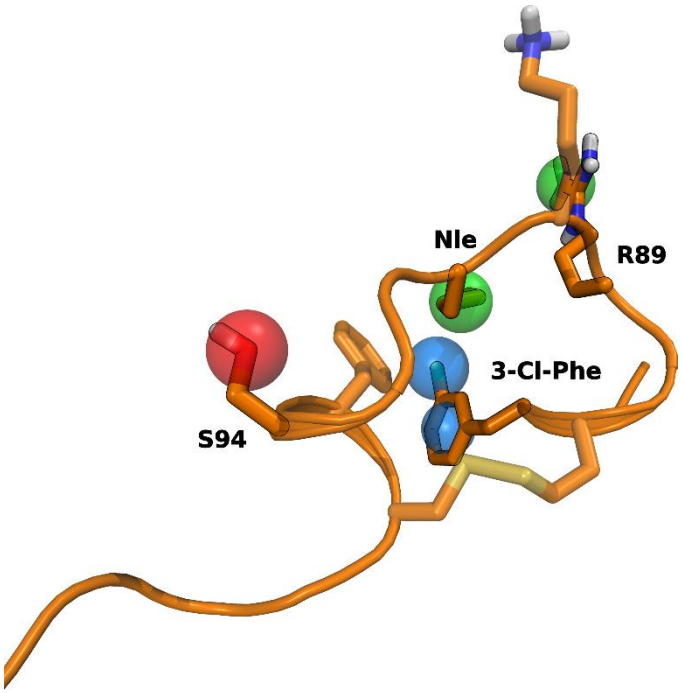


*Figure 512 Pharmacophore model built on the Ω-peptide modelled in complex with TEAD. The first pharmacophore model comprises the aromatic group and the hydrophobic feature of the chlorine atom of 3-Cl-phe (blue spheres). The second pharmacophore model comprises the hydrophobic side chain of Nle and the hydrogen bond-donor of the guanidinium group of R89 (green spheres). Both the pharmacophore models share the hydrogen bond-acceptor feature of the S94 hydroxyl group (red sphere).*

## *Shape similarity-based filtering*

In an attempt to identify potential leads endowed with the highest predicted affinity and characterised by an optimal similarity with the stereo-electronic features of the crystallised YAP Ω-loop, the compounds screened through the pharmacophore-based search were submitted to a shape similarity screening. In order to privilege compounds able to mimic the particular conformation of the YAP Ω-loop, and to reproduce the arrangement of the hydrophobic residues pointing towards the TEAD surface, a portion of the YAP Ω-loop was used as template for the similarity search.

*Definition of a Consensus score and cluster analysis of the virtual screening results: selection of potential YAP-TEAD inhibitors*

In order to select a reasonable number of compounds for the subsequent biological evaluation, a customised scoring function, combining both a physical term (i.e. the molecular weight) and similarity/adherence to the pharmacophore model terms, was used.

More specifically, the calculated consensus score takes into account the adherence to pharmacophore model, the similarity to the YAP Ω-loop and the predicted binding affinity. A term considering the molecular weight of the compounds was also included in the scoring function, in order to privilege compounds characterised by a medium-high molecular weight, consistently to the known protein-protein interaction inhibitors features.

3000 top ranked compounds from the ChemDiv and the eMolecules libraries were finally selected.

As a final selection step, a hierarchical cluster analysis was performed, in order to reduce the number of the significant scaffolds to consider, while maximising the diversification of the chemical space among the potential lead compounds. In this case, the dendrogram was cut in order to obtain 100 clusters, which were singularly analysed in order to extract from each cluster the compounds characterised by the highest consensus score. Specifically, among similar structures, lead compounds showing the highest consensus score were selected. Singletons, characterised by a medium-high consensus score, were also included in the final selection, in order to enhance the diversity among the scaffolds.

This process led to the identification of 200 compounds from the eMolecules and ChemDiv-PPI libraries, which will be evaluated to test their activity as potential YAP-TEAD interaction inhibitors, in order to identify promising lead compounds for the further chemical optimisation.

*Validation of the docking protocol: docking study of known active synthetic peptides*

In order to validate the screening protocol applied for the identification of the potential YAP-TEAD inhibitors, and in particular to test the reliability of the docking score assigned to ligands, a docking study on a series of synthetic peptides mimicking the YAP Ω-loop, the YAP affinities of which have been recently reported,[342] has been performed.

The peptides are characterised by a macro-cyclic structure, overlapping the typical Ω conformation adopted by YAP residues 84-100. These peptides have been obtained, starting from the YAP sequence, inducing the formation of internal disulfide bonds between residues 87 and 96, which have been mutated to cysteine and/or homocysteine residues. A selection of the reported peptides showing an inhibitory potency ranging from the low-nanomolar to the micromolar, including the reference peptide with the sequence of Ω-loop[333], was then used as a test set, in order to evaluate the ability of the docking procedure used in this research project to predict the experimental $IC_{50}$ values of YAP-TEAD inhibitors.

| Peptide | Mutations (respect to YAP Ω loop) | $IC_{50}$ (μM) |
|---|---|---|
| **#1**[342] | F96C<br>R87C | 100 |
| **#2**[342] | F96C<br>R87HCys | 6.9 |
| **#3**[342] | F96C<br>R87HCys<br>D93A | 1.5 |
| **#4**[342] | F96C<br>R87HCys<br>D93A<br>L91Nle | 0.15 |
| **#5**[342] | F96C<br>R87HCys<br>D93A<br>L91Ahe | 0.075 |
| **#6**[342] | F96C<br>R87HCys<br>D93A<br>L91Nle<br>M86Nle | 0.34 |
| **Ω-peptide**[333] | F96C<br>R87HCys<br>D93A<br>L91Nle<br>M86 3-Cl-Phe | 0.025 |

*Table 4 Potency values of YAP-TEAD peptide inhibitors and of the reference Ω-peptide. Single point mutations performed on each peptide are reported.*

The docking studies were performed starting from the crystal structure of hTEAD in complex with an engineered form of YAP (PDB 4RE1), characterised by the Ω-loop permanently stabilised in its conformation by an internal disulfide. The complexes of hTEAD with each macro-peptide were then evaluated and ranked according the GScore, that is, the predicted binding affinity.

The correlation between the experimental $IC_{50}$ of the macro-peptides and the predicted affinity, i.e. GScore, calculated within the docking procedure, was evaluated.

The Spearman's rank correlation coefficient was applied, in order to evaluate the ability to rank the experimental $IC_{50}$ (dependent variable) of compounds according to the predicted binding affinity (independent variable). The Spearman's rank correlation coefficient ($\boldsymbol{\rho}$) is a non-parametric measure of the strength of the statistical dependence between two ordinal variables. More specifically, this parameter assess how well the relationship between the ranked variables is described by a monotonic function. In an ideal case, if the dependent variable (**y**) is the monotone function of the independent one (**x**), $\boldsymbol{\rho}$ is equal to +1 or -1, depending on the tendency of **y** to increase or decrease when **x** increases. A Spearman's coefficient of 0 indicates that there is not a monotonic relationship between the variables. For a sample size of *n*, with the ranked scores $\mathbf{x_i}$ and $\mathbf{y_i}$, $\boldsymbol{\rho}$ is calculated as following:

$$\rho = 1 - \frac{6 \sum d_i^2}{n(n^2 - 1)}$$

Where $d_i$ is the difference between ranks ($\mathbf{x_i} - \mathbf{y_i}$).

The data set considered in this work comprises the seven peptides used in the docking study. The independent variable **x** (predicted binding affinity, GScore) and the dependent variable **y** (the measured $IC_{50}$) where preliminarily converted into ranked variables, by assigning a rank of 1 to Ω-peptide (top ranked GScore compound) and of 7 to peptide **#1**, showing the lowest GScore:

| Peptide | X (GScore) | x (ranked GScore) | Y ($IC_{50}$, μM) | Y (ranked $IC_{50}$) | *d* (x-y) | $d^2$ |
|---|---|---|---|---|---|---|
| **Ω-peptide** | -7.502 | **1** | 0.025 | **1** | 0 | 0 |
| **#2** | -6.555 | **2** | 6.9 | **6** | -4 | 16 |
| **#5** | -6.452 | **3** | 0.075 | **2** | 1 | 1 |
| **#4** | -6.176 | **4** | 0.15 | **3** | 1 | 1 |
| **#13** | -5.518 | **5** | 0.34 | **4** | 1 | 1 |
| **#3** | -5.153 | **6** | 1.5 | **5** | 1 | 1 |
| **#1** | -1.247 | **7** | 100 | **7** | 0 | 0 |

$$\rho = 1 - \frac{6\sum d_i^2}{n(n^2-1)} = 1 - \frac{6 \times 20}{7 \times 48} = \mathbf{0.643}$$

The Spearman's coefficient value obtained reveals a weak positive monotone relationship between the two variables. In fact, docked peptides, characterised by a good GScore value, generally show a higher inhibitory potency. On the other hand, the data set used here comprises an object, peptide **#2**, showing a remarkable difference between the GScore ranking value (2) and the corresponding ranked $IC_{50}$ (6). The peptide is indeed one of the weakest YAP-TEAD inhibitors considered here, while the Glide scoring function predicted a good binding affinity for the complex TEAD-**#2**. Notably, the elimination of **#2** from the data set gave a perfect positive monotone relationship between the GScore and the $IC_{50}$ of known active peptides.

$$\rho = 1 - \frac{6\sum d_i^2}{n(n^2-1)} = 1 - \frac{6 \times 0}{6 \times 36} = \mathbf{1.000}$$

The reliability of this docking procedure, which was able to discriminate between know active and inactive YAP-TEAD inhibitors, was thus assessed, suggesting that the virtual

screening protocol applied in this work is a solid protocol. On the other hand, the presence of outliers (i.e. **#2**) reveals the weakness of the docking procedure in the prediction of the binding affinity of big and flexible compounds, such as polypeptides.

## *Conclusions*

The YAP-TEAD complex represents an emerging target of great interest under different aspects. Being the downstream effector of the growth control pathway Hippo, the regulation of its activity is of straightforward importance in the view of the identification of novel antitumor drugs or, conversely, of new compounds able to promote the stem cell proliferation, to be optimised for regenerative medicine applications.

To date, there are not small molecules known to be selective and potent inhibitors of the YAP-TEAD interaction, and the molecular mechanism of compounds that interfere with the YAP-TEAD-mediated genic effects, such as verteporfin or compound C108, is still unknown.

Virtual screening studies, aiming at the identification of YAP-TEAD modulators, represent a challenging research field, hindered by the lack of knowledge about the binding modes of active compounds. On the other hand, protein-protein interactions represent a complex and multifaceted issue in the field of the rational design of biologically active compounds.

In this research project, a solid computational protocol has been prompted, which allowed the identification of potential lead compounds through the combination of multiple screening approaches, aiming at the minimisation of the deficiencies of each approach and at the optimal use of the structural elements available.

## *Computational protocol*

### *Protein preparation*

The crystal structure of the hYAP1-TEAD4 complex (PDB 3KYS; chain D and C, respectively) was prepared using the Protein Preparation Wizard tool provided with the Schrödinger 2014-2

software suite[w]. Missing residues, producing gaps in the amino acids sequence, were modelled with Prime 3.6[x]. The C- and N-*termini* of TEAD were capped with acetyl and methylamino groups, respectively. The missing hydrogen atoms were added, while the missing side chains were remodelled. The orientation of hydroxyl groups, thiols, and the conformation of histidine residues were modelled in order to maximise the overall hydrogen-bonding network. Basic and acid residues were modelled in their charged form. The complex structure was minimised with the OPLS2005 force field through a first minimisation run with constrained heavy atoms, and a second minimisation run with heavy atoms position restrained to a RMSD value of 0.3 Å.

*Building the TEAD-peptide complex*

The prediction of the binding mode of flexible polypeptides to proteins is a strong limit of the principal docking tools. A major issue is related to the limited of the sampling protocol, hampering a comprehensive conformational sampling of large structures characterised by a large number of rotatable bonds. In order to overcome this specific issue ad hoc protocol was set up.

1. In order to reduce the number of rotatable bonds, and to allow the docking of a simplified version of the cyclic macro-peptide to TEAD surface, a model of the Ω-peptide was built in Maestro 9.8[y]. The side chains of residues 84-86 and 95-100, which can be considered as substituents inserted on the cyclic peptide, were temporarily removed. The remaining residues were temporarily mutated to alanine.
2. The docking studies were performed using Glide 6.3[z]. The docking grid was built on TEAD surface with a cubic inner box of 10 Å, centred on the position of residues K289, E383, V406 and Y421. The van der Waals radii of TEAD were reduced of a scaling factor of 0.6. The van der Waals radii of the cyclopeptide were reduced of a scaling factor of 0.6. The docking study was performed using the SP-Peptide protocol implemented in Glide 6.3. In order to obtain binding modes characterised by a correct orientation, the position of the cyclopeptide core was constrained to the position of the YAP Ω-loop.

[w] Schrödinger Release 2014-2: Schrödinger Suite 2014-2 Protein Preparation Wizard; Epik version 2.8, Schrödinger, LLC, New York, NY, 2014; Impact version 6.3, Schrödinger, LLC, New York, NY, 2014; Prime version 3.6, Schrödinger, LLC, New York, NY, 2014.
[x] Prime, version 3.6, Schrödinger, LLC, New York, NY, 2014.
[y] Maestro, version 9.8, Schrödinger, LLC, New York, NY, 2014.
[z] Glide, version 6.3, Schrödinger, LLC, New York, NY, 2014.

3. The temporarily removed and mutated side chains were reintroduced, and the complex was minimised with Macromodel 10.4[aa] applying the Polak-Ribiere conjugate gradient method to a covergence treshold of 0.05 kJ $mol^{-1}Å^{-1}$. During the minimisation, the backbone atoms of both TEAD and the Ω-peptide were restrained. A final minimisation run without any restrain was performed in the same conditions.

*Molecular Dynamics simulation of the TEAD-Ω-peptide complex*

A Molecular Dynamics simulation was performed, in order to evaluate the dynamical stability of the model built following the procedure described above. The TEAD fragment was modelled using the force field parameters of OPLS2005[154] provided with Desmond 3.8[bb], while the parameters of the Ω-peptide were determined using the Charmm Generalized Force Field (CGenFF).

The complex was then solvated by approximatively 36500 TIP3P water molecules. Bond lengths to hydrogen atoms were constrained by applying the M-SHAKE algorithm. Short-range electrostatic interactions were cut off at 9Å, whereas long-range electrostatic interactions were treated using the Smooth Particle Mesh Ewald method. A RESPA integrator was used with a time-step of 2 fs, while long-range electrostatic interactions were computed every 6 fs. The systems were relaxed using a modified version the protocol implemented in the Desmond package:

1. Minimisation with restraints on the solute heavy atoms
2. Minimisation without any restraints
3. 200 ps simulation in the NVT ensemble with the Berendsen thermostat method with:
    a. a temperature of 300 K
    b. 50 kcal/mol restraints on the complex heavy atoms
4. 200 ps simulation in the NVT ensemble with:
    a. a temperature of 100 K
    b. 50 kcal/mol restraints on protein heavy atoms
5. 400 ps simulation in the NVT ensemble with:
    a. a temperature of 100 K
    b. 50 kcal/mol restraints on TEAD backbone and Ω-peptide Cα and Cβ
6. 400 ps simulation in the NVT ensemble with:
    a. a temperature of 300 K
    b. 50 kcal/mol restraints on TEAD backbone and Ω-peptide Cα and Cβ

[aa] MacroModel, version 10.4, Schrödinger, LLC, New York, NY, 2014.
[bb] Desmond Molecular Dynamics System, version 3.8, D. E. Shaw Research, New York, NY, 2014. Maestro-Desmond Interoperability Tools, version 3.8, Schrödinger, New York, NY, 2014.

7. 400 ps simulation in the NVT ensemble with:
    a. a temperature of 300 K
    b. 25 kcal/mol restraints on TEAD backbone and Ω-peptide Cα and Cβ
8. 600 ps simulation in the NPT ensemble with:
    a. a temperature of 300 K
    b. 25 kcal/mol restraints on TEAD and Ω-peptide Cα and Cβ
9. 400 ps simulation in the NPT ensemble with:
    a. a temperature of 300 K
    b. 10 kcal/mol restraints on TEAD and Ω-peptide Cα and Cβ
10. 400 ps simulation in the NPT ensemble with:
    a. a temperature of 300 K
    b. 10 kcal/mol restraints on TEAD and Ω-peptide Cα
11. 400 ps simulation in the NPT ensemble with:
    a. a temperature of 300 K
    b. 5 kcal/mol restraints on TEAD and Ω-peptide Cα
12. 400 ps simulation in the NPT ensemble with:
    a. a temperature of 300 K
    b. 5 kcal/mol restraints on Ω-peptide Cα
13. 200 ps simulation in the NPT ensemble with:
    a. a temperature of 300 K
    b. no restraints.

Following the equilibration protocol, the MD simulation was run for 50ns.

*Filtering and preparation of the chemical libraries*

The chemical libraries were preliminary filtered, in order to eliminate compounds characterised by a high reactivity, giving aspecific an positive results within screening assays (PAINS; pan-assays interference compounds), while compounds characterised by a low molecular weight were filtered out. The following criteria were imposed:

| **Criterion** | **Value** |
|---|---|
| **Molecular Weight** | 100 < MW < 900 (ChemDiv)<br>250 < MW < 900 (eMolecules) |
| **# reactive groups** | = 0 |
| **# Michael acceptors** | = 0 |
| **# phosphonate esters** | = 0 |
| **# peroxides** | = 0 |

| | |
|---|---|
| **# sulphonate esters** | = 0 |
| **# aziridines** | = 0 |
| **# epoxides** | = 0 |
| **# acyl halides** | = 0 |
| **# halopyrimidines** | = 0 |
| **# isothiocyanates** | = 0 |
| **# isonitriles** | = 0 |
| **# acceptor groups** | ≥ 1 (eMolecules) |

The filtered ligands were prepared using the LigPrep 3.0[cc] tool. Epik 2.8[dd] was used to generate the protonation states at physiological pH and to generate the energetic penalties. The chirality of the ligands was maintained (if specified in the 2D file), while all the possible stereoisomers were generated for other compounds. Salts and other cofactors molecules were removed.

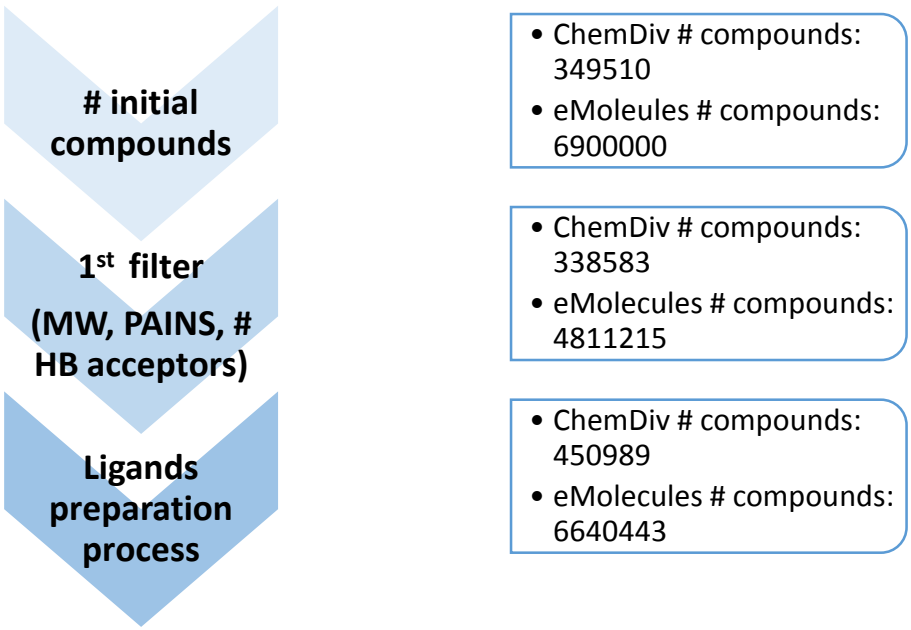


*Figure 523 Progressive modification of the libraries composition within the filtering and preparation procedures*

[cc] LigPrep, version 3.0, Schrödinger, LLC, New York, NY, 2014.
[dd] Epik, version 2.8, Schrödinger, LLC, New York, NY, 2014.

*Pharmacophore models*

The pharmacophore models were built with Phase 3.9[ee,343,344]. For both the pharmacophore models, three distinct pharmacophore features were mapped to their specific location in the TEAD-binding Ω-peptide conformation. The matching of all the pharmacophore features was imposed. The screened compounds were ranked according to their fitness score, which is a linear combination of the site and vector alignment score, providing a measure of how well the ligands in their specific conformation match the pharmacophore hypothesis.

The pharmacophore-based screening led to the identification of 22137 compounds from the ChemDiv library and 15202 compounds from the eMolecules library, with a fitness value ranging from 0 to 1.473 for ChemDiv ligands and from 0 to 1.482 for eMolecules ligands.

*Docking study on TEAD surface*

The compounds screened for the adherence to the pharmacophore models were submitted to a docking study on hTEAD (PDB 3KYS) using Glide 6.3[u].

The docking grid was built on TEAD surface with a cubic inner box of 14 Å, centred on the position of residues K289, E383, V406 and Y421. The SP-Peptide docking protocol implemented in Glide 3.6 was used, in order to permit a more comprehensive conformational search of the ligands, while all the other parameters were set to the default value.

The docking study gave 22135 poses from the ChemDiv compounds and 13916 from the eMolecules library.

*Shape similarity screening*

The Shape similarity search was performed using Phase 3.9[z]; a portion of the YAP Ω loop was selected as template molecule, adjusting the residues weights in order to impose a higher relevance for S94, F95, L91 and M86 side chains. The shape similarity search was performed on atom types, using the MacroModel atom types search, which imposes the most stringent conditions. The compounds similarity was calculated as a function of the overlap between the template and the ligands, and the self-overlaps. Shape similarity values obtained for ChemDiv and eMolecules compounds ranged from 0 to 0.455 and from 0 to 0.448, respectively

[ee] Phase, version 3.9, Schrödinger, LLC, New York, NY, 2014.

*Determination of the Consensus score*

The specific consensus score, calculated in order to rank the lead compounds emerged from the virtual screening study, takes into account the adherence to pharmacophore model (fitness score), the similarity to the YAP Ω-loop (shape similarity) and the predicted binding affinity (GScore). The molecular weight has been introduced, in order to privilege medium-high MW compounds. The calculated consensus score is:

$$Consensus\ score\ =\ X_{fitness} \times X_{shape\ similarity} \times X_{GScore} \times [X_{MW}]^2$$

Where:

$$X_{(term)} = \frac{(X - X_{min})}{(X_{max} - X_{min})}$$

*Hierarchical cluster analysis*

The hierarchical cluster analysis was performed with Canvas 2.0[ff,345,346], applying a top-down approach, aiming at the identification of a predefined number of clusters (100, in this case). Linear hashed fingerprints were used in this work, and the Tanimoto similarity metrics was used to cluster the compounds. The Tanimoto similarity is calculated over bitmaps, in which each bit of a fixed-size array stands for the presence or the absence of specific chemical feature. The similarity value is calculated as the ratio between the number of common bits and the number of bits in either sample. For two bitmaps X and Y, in which $X_i$ is the $i^{th}$ bit of $X$, and $Y_i$ is the $i^{th}$ bit of $Y$, the similarity ratio $T_S$ is calculated as following:

$$T_S(X, Y)\ =\ \frac{\sum_i (X_i \cup Y_i)}{\sum_i (X_i \cap Y_i)}$$

*Docking studies of known active peptides*

The peptides were prepared in Maestro 9.8[gg] and submitted to a minimisation run performed with Macromodel 10.4[hh] using the OPLS2005[154] force field.

[ff] Canvas, version 2.0, Schrödinger, LLC, New York, NY, 2014.
[gg] Maestro, version 9.8, Schrödinger, LLC, New York, NY, 2014.
[hh] MacroModel, version 10.4, Schrödinger, LLC, New York, NY, 2014

The docking grid was built hTEAD structure (PDB 4RE1) using Glide 6.3[ii], imposing an inner box of 10 Å. The van der Waals radii of the receptor and of the ligands were reduced of a scaling factor of 0.6 and 0.4, respectively. The SP-peptide protocol was applied, and restraints were imposed on the backbone atoms of the ligands, in order to obtain an optimal superposition of the inhibitor structures to the YAP Ω loop. The binding modes obtained were finally ranked according to their GScore values.

[ii] Glide, version 6.3, Schrödinger, LLC, New York, NY, 2014.

## References


1. Howlett, A. C. *et al.* The cannabinoid receptor: biochemical, anatomical and behavioral characterization. *Trends Neurosci.* **13,** 420–423 (1990).
2. Devane, W. A. *et al.* Isolation and structure of a brain constituent that binds to the cannabinoid receptor. *Science* **258,** 1946–1949 (1992).
3. Mechoulam, R. *et al.* Identification of an endogenous 2-monoglyceride, present in canine gut, that binds to cannabinoid receptors. *Biochem. Pharmacol.* **50,** 83–90 (1995).
4. Sugiura, T. *et al.* 2-Arachidonoylgylcerol: A Possible Endogenous Cannabinoid Receptor Ligand in Brain. *Biochem. Biophys. Res. Commun.* **215,** 89–97 (1995).
5. Stella, N., Schweitzer, P. & Piomelli, D. A second endogenous cannabinoid that modulates long-term potentiation. *Nature* **388,** 773–778 (1997).
6. Tsou, K., Brown, S., Sañudo-Peña, M. C., Mackie, K. & Walker, J. M. Immunohistochemical distribution of cannabinoid CB1 receptors in the rat central nervous system. *Neuroscience* **83,** 393–411 (1998).
7. Egertová, M., Giang, D. K., Cravatt, B. F. & Elphick, M. R. A new perspective on cannabinoid signalling: complementary localization of fatty acid amide hydrolase and the CB1 receptor in rat brain. *Proc. Biol. Sci.* **265,** 2081–2085 (1998).
8. Katona, I. *et al.* Presynaptically located CB1 cannabinoid receptors regulate GABA release from axon terminals of specific hippocampal interneurons. *J. Neurosci. Off. J. Soc. Neurosci.* **19,** 4544–4558 (1999).
9. Kawamura, Y. *et al.* The CB1 cannabinoid receptor is the major cannabinoid receptor at excitatory presynaptic sites in the hippocampus and cerebellum. *J. Neurosci. Off. J. Soc. Neurosci.* **26,** 2991–3001 (2006).

10. Lee, S.-H., Földy, C. & Soltesz, I. Distinct endocannabinoid control of GABA release at perisomatic and dendritic synapses in the hippocampus. *J. Neurosci. Off. J. Soc. Neurosci.* **30,** 7993–8000 (2010).

11. Katona, I. *et al.* GABAergic interneurons are the targets of cannabinoid actions in the human hippocampus. *Neuroscience* **100,** 797–804 (2000).

12. Van Sickle, M. D. *et al.* Identification and functional characterization of brainstem cannabinoid CB2 receptors. *Science* **310,** 329–332 (2005).

13. Maresz, K. *et al.* Direct suppression of CNS autoimmune inflammation via the cannabinoid receptor CB1 on neurons and CB2 on autoreactive T cells. *Nat. Med.* **13,** 492–497 (2007).

14. Piomelli, D. & Sasso, O. Peripheral gating of pain signals by endogenous lipid mediators. *Nat. Neurosci.* **17,** 164–174 (2014).

15. Piomelli, D., Astarita, G. & Rapaka, R. A neuroscientist's guide to lipidomics. *Nat. Rev. Neurosci.* **8,** 743–754 (2007).

16. Piomelli, D. The molecular logic of endocannabinoid signalling. *Nat. Rev. Neurosci.* **4,** 873–884 (2003).

17. Hájos, N. *et al.* Cannabinoids inhibit hippocampal GABAergic transmission and network oscillations. *Eur. J. Neurosci.* **12,** 3239–3249 (2000).

18. Wilson, R. I. & Nicoll, R. A. Endogenous cannabinoids mediate retrograde signalling at hippocampal synapses. *Nature* **410,** 588–592 (2001).

19. Ohno-Shosaku, T., Maejima, T. & Kano, M. Endogenous cannabinoids mediate retrograde signals from depolarized postsynaptic neurons to presynaptic terminals. *Neuron* **29,** 729–738 (2001).

20. Kreitzer, A. C. & Regehr, W. G. Retrograde inhibition of presynaptic calcium influx by endogenous cannabinoids at excitatory synapses onto Purkinje cells. *Neuron* **29,** 717–727 (2001).

21. Xu, J.-Y. & Chen, C. Endocannabinoids in Synaptic Plasticity and Neuroprotection. *The Neuroscientist* **21,** 152–168 (2015).

22. Chevaleyre, V., Takahashi, K. A. & Castillo, P. E. Endocannabinoid-mediated synaptic plasticity in the CNS. *Annu. Rev. Neurosci.* **29,** 37–76 (2006).

23. Mato, S., Lafourcade, M., Robbe, D., Bakiri, Y. & Manzoni, O. J. Role of the cyclic-AMP/PKA cascade and of P/Q-type Ca++ channels in endocannabinoid-mediated long-term depression in the nucleus accumbens. *Neuropharmacology* **54,** 87–94 (2008).

24. Kano, M., Ohno-Shosaku, T., Hashimotodani, Y., Uchigashima, M. & Watanabe, M. Endocannabinoid-mediated control of synaptic transmission. *Physiol. Rev.* **89,** 309–380 (2009).

25. Heifets, B. D. & Castillo, P. E. Endocannabinoid signaling and long-term synaptic plasticity. *Annu. Rev. Physiol.* **71,** 283–306 (2009).

26. Clapper, J. R. *et al.* Anandamide suppresses pain initiation through a peripheral endocannabinoid mechanism. *Nat. Neurosci.* **13,** 1265–1270 (2010).

27. Kinsey, S. G. *et al.* Blockade of endocannabinoid-degrading enzymes attenuates neuropathic pain. *J. Pharmacol. Exp. Ther.* **330,** 902–910 (2009).

28. Straiker, A. *et al.* COX-2 and fatty acid amide hydrolase can regulate the time course of depolarization-induced suppression of excitation. *Br. J. Pharmacol.* **164,** 1672–1683 (2011).

29. Gerdeman, G. L., Ronesi, J. & Lovinger, D. M. Postsynaptic endocannabinoid release is critical to long-term depression in the striatum. *Nat. Neurosci.* **5,** 446–451 (2002).

30. Kim, J. & Alger, B. E. Reduction in endocannabinoid tone is a homeostatic mechanism for specific inhibitory synapses. *Nat. Neurosci.* **13,** 592–600 (2010).

31. Chávez, A. E., Chiu, C. Q. & Castillo, P. E. TRPV1 activation by endogenous anandamide triggers postsynaptic long-term depression in dentate gyrus. *Nat. Neurosci.* **13,** 1511–1518 (2010).

32. Grueter, B. A., Brasnjo, G. & Malenka, R. C. Postsynaptic TRPV1 triggers cell type-specific long-term depression in the nucleus accumbens. *Nat. Neurosci.* **13,** 1519–1525 (2010).

33. Dinh, T. P., Freund, T. F. & Piomelli, D. A role for monoglyceride lipase in 2-arachidonoylglycerol inactivation. *Chem. Phys. Lipids* **121,** 149–158 (2002).

34. Gulyas, A. I. *et al.* Segregation of two endocannabinoid-hydrolyzing enzymes into pre- and postsynaptic compartments in the rat hippocampus, cerebellum and amygdala. *Eur. J. Neurosci.* **20,** 441–458 (2004).

35. Ludányi, A. *et al.* Complementary synaptic distribution of enzymes responsible for synthesis and inactivation of the endocannabinoid 2-arachidonoylglycerol in the human hippocampus. *Neuroscience* **174,** 50–63 (2011).

36. Bisogno, T. *et al.* Cloning of the first sn1-DAG lipases points to the spatial and temporal regulation of endocannabinoid signaling in the brain. *J. Cell Biol.* **163,** 463–468 (2003).

37. Mátyás, F. *et al.* Identification of the sites of 2-arachidonoylglycerol synthesis and action imply retrograde endocannabinoid signaling at both GABAergic and glutamatergic synapses in the ventral tegmental area. *Neuropharmacology* **54,** 95–107 (2008).

38. Yoshida, T. *et al.* Localization of diacylglycerol lipase-alpha around postsynaptic spine suggests close proximity between production site of an endocannabinoid, 2-arachidonoyl-glycerol, and presynaptic cannabinoid CB1 receptor. *J. Neurosci. Off. J. Soc. Neurosci.* **26,** 4740–4751 (2006).

39. Jung, K.-M. *et al.* A key role for diacylglycerol lipase-alpha in metabotropic glutamate receptor-dependent endocannabinoid mobilization. *Mol. Pharmacol.* **72,** 612–621 (2007).

40. Kammermeier, P. J. & Worley, P. F. Homer 1a uncouples metabotropic glutamate receptor 5 from postsynaptic effectors. *Proc. Natl. Acad. Sci. U. S. A.* **104,** 6055–6060 (2007).

41. Brakeman, P. R. *et al.* Homer: a protein that selectively binds metabotropic glutamate receptors. *Nature* **386,** 284–288 (1997).

42. Katona, I. & Freund, T. F. Endocannabinoid signaling as a synaptic circuit breaker in neurological disease. *Nat. Med.* **14,** 923–930 (2008).

43. Dinh, T. P. *et al.* Brain monoglyceride lipase participating in endocannabinoid inactivation. *Proc. Natl. Acad. Sci.* **99,** 10819–10824 (2002).

44. Dinh, T. P., Kathuria, S. & Piomelli, D. RNA Interference Suggests a Primary Role for Monoacylglycerol Lipase in the Degradation of the Endocannabinoid 2-Arachidonoylglycerol. *Mol. Pharmacol.* **66,** 1260–1264 (2004).

45. Muccioli, G. G. *et al.* Identification of a Novel Endocannabinoid-Hydrolyzing Enzyme Expressed by Microglial Cells. *J. Neurosci.* **27,** 2883–2889 (2007).

46. Marrs, W. R. *et al.* The serine hydrolase ABHD6 controls the accumulation and efficacy of 2-AG at cannabinoid receptors. *Nat. Neurosci.* **13,** 951–957 (2010).

47. Blankman, J. L., Long, J. Z., Trauger, S. A., Siuzdak, G. & Cravatt, B. F. ABHD12 controls brain lysophosphatidylserine pathways that are deregulated in a murine model of the neurodegenerative disease PHARC. *Proc. Natl. Acad. Sci.* **110,** 1500–1505 (2013).

48. Hermanson, D. J., Gamble-George, J. C., Marnett, L. J. & Patel, S. Substrate-selective COX-2 inhibition as a novel strategy for therapeutic endocannabinoid augmentation. *Trends Pharmacol. Sci.* **35,** 358–367 (2014).

49. Jhaveri, M. D. *et al.* Inhibition of fatty acid amide hydrolase and cyclooxygenase-2 increases levels of endocannabinoid related molecules and produces analgesia via peroxisome proliferator-activated receptor-alpha in a model of inflammatory pain. *Neuropharmacology* **55,** 85–93 (2008).

50. Kim, J. & Alger, B. E. Inhibition of cyclooxygenase-2 potentiates retrograde endocannabinoid effects in hippocampus. *Nat. Neurosci.* **7,** 697–698 (2004).

51. Kozak, K. R., Rowlinson, S. W. & Marnett, L. J. Oxygenation of the Endocannabinoid, 2-Arachidonylglycerol, to Glyceryl Prostaglandins by Cyclooxygenase-2. *J. Biol. Chem.* **275,** 33744–33749 (2000).

52. Kozak, K. R., Prusakiewicz, J. J., Rowlinson, S. W., Schneider, C. & Marnett, L. J. Amino Acid Determinants in Cyclooxygenase-2 Oxygenation of the Endocannabinoid 2-Arachidonylglycerol. *J. Biol. Chem.* **276,** 30072–30077 (2001).

53. Valdeolivas, S. *et al.* The inhibition of 2-arachidonoyl-glycerol (2-AG) biosynthesis, rather than enhancing striatal damage, protects striatal neurons from malonate-induced death: a potential role of cyclooxygenase-2-dependent metabolism of 2-AG. *Cell Death Dis.* **4,** e862 (2013).

54. Nomura, D. K. *et al.* Endocannabinoid Hydrolysis Generates Brain Prostaglandins That Promote Neuroinflammation. *Science* **334,** 809–813 (2011).

55. Hu, S. S.-J., Bradshaw, H. B., Chen, J. S.-C., Tan, B. & Walker, J. M. Prostaglandin E 2 glycerol ester, an endogenous COX-2 metabolite of 2-arachidonoylglycerol, induces hyperalgesia and modulates NFκB activity. *Br. J. Pharmacol.* **153,** 1538–1549 (2008).

56. Di Marzo, V. *et al.* Formation and inactivation of endogenous cannabinoid anandamide in central neurons. *Nature* **372,** 686–691 (1994).

57. Ueda, N., Tsuboi, K. & Uyama, T. Metabolism of endocannabinoids and related N-acylethanolamines: Canonical and alternative pathways. *FEBS J.* **280,** 1874–1894 (2013).

58. Piomelli, D. More surprises lying ahead. The endocannabinoids keep us guessing. *Neuropharmacology* **76, Part B,** 228–234 (2014).

59. Gulyas, A. I. *et al.* Segregation of two endocannabinoid-hydrolyzing enzymes into pre- and postsynaptic compartments in the rat hippocampus, cerebellum and amygdala. *Eur. J. Neurosci.* **20,** 441–458 (2004).

60. Connell, K., Bolton, N., Olsen, D., Piomelli, D. & Hohmann, A. G. Role of the basolateral nucleus of the amygdala in endocannabinoid-mediated stress-induced analgesia. *Neurosci. Lett.* **397,** 180–184 (2006).

61. Gaetani, S., Cuomo, V. & Piomelli, D. Anandamide hydrolysis: a new target for anti-anxiety drugs? *Trends Mol. Med.* **9,** 474–478 (2003).

62. Cravatt, B. F. *et al.* Supersensitivity to anandamide and enhanced endogenous cannabinoid signaling in mice lacking fatty acid amide hydrolase. *Proc. Natl. Acad. Sci. U. S. A.* **98,** 9371–9376 (2001).

63. Solinas, M. *et al.* The endogenous cannabinoid anandamide produces delta-9-tetrahydrocannabinol-like discriminative and neurochemical effects that are enhanced by inhibition of fatty acid amide hydrolase but not by inhibition of anandamide transport. *J. Pharmacol. Exp. Ther.* **321,** 370–380 (2007).

64. Boger, D. L. *et al.* Fatty acid amide hydrolase substrate specificity. *Bioorg. Med. Chem. Lett.* **10,** 2613–2616 (2000).

65. Beltramo, M. & Piomelli, D. Carrier-mediated transport and enzymatic hydrolysis of the endogenous cannabinoid 2-arachidonylglycerol. *Neuroreport* **11,** 1231–1235 (2000).

66. Lichtman, A. H., Hawkins, E. G., Griffin, G. & Cravatt, B. F. Pharmacological Activity of Fatty Acid Amides Is Regulated, but Not Mediated, by Fatty Acid Amide Hydrolase in Vivo. *J. Pharmacol. Exp. Ther.* **302,** 73–79 (2002).

67. Ludányi, A. *et al.* Downregulation of the CB1 cannabinoid receptor and related molecular elements of the endocannabinoid system in epileptic human hippocampus. *J. Neurosci. Off. J. Soc. Neurosci.* **28,** 2976–2990 (2008).

68. Kirschstein, T. *et al.* Loss of metabotropic glutamate receptor-dependent long-term depression via downregulation of mGluR5 after status epilepticus. *J. Neurosci. Off. J. Soc. Neurosci.* **27,** 7696–7704 (2007).

69. Fernández-Ruiz, J. *et al.* Cannabidiol for neurodegenerative disorders: important new clinical applications for this phytocannabinoid? *Br. J. Clin. Pharmacol.* **75,** 323–333 (2013).

70. Chiarlone, A. *et al.* A restricted population of CB1 cannabinoid receptors with neuroprotective activity. *Proc. Natl. Acad. Sci. U. S. A.* **111,** 8257–8262 (2014).

71. Xu, J.-Y. & Chen, C. Endocannabinoids in synaptic plasticity and neuroprotection. *Neurosci. Rev. J. Bringing Neurobiol. Neurol. Psychiatry* **21,** 152–168 (2015).

72. Zhang, J., Teng, Z., Song, Y., Hu, M. & Chen, C. Inhibition of monoacylglycerol lipase prevents chronic traumatic encephalopathy-like neuropathology in a mouse model of repetitive mild closed head injury. *J. Cereb. Blood Flow Metab. Off. J. Int. Soc. Cereb. Blood Flow Metab.* **35,** 443–453 (2015).

73. Schmidt, W., Schäfer, F., Striggow, V., Fröhlich, K. & Striggow, F. Cannabinoid receptor subtypes 1 and 2 mediate long-lasting neuroprotection and improve motor behavior deficits after transient focal cerebral ischemia. *Neuroscience* **227,** 313–326 (2012).

74. Fernández-Ruiz, J., Moro, M. A. & Martínez-Orgado, J. Cannabinoids in Neurodegenerative Disorders and Stroke/Brain Trauma: From Preclinical Models to Clinical Applications. *Neurother. J. Am. Soc. Exp. Neurother.* **12,** 793–806 (2015).

75. Yang, L.-C. *et al.* Chronic oleoylethanolamide treatment improves spatial cognitive deficits through enhancing hippocampal neurogenesis after transient focal cerebral ischemia. *Biochem. Pharmacol.* **94,** 270–281 (2015).

76. Schomacher, M., Müller, H. D., Sommer, C., Schwab, S. & Schäbitz, W.-R. Endocannabinoids mediate neuroprotection after transient focal cerebral ischemia. *Brain Res.* **1240,** 213–220 (2008).

77. Carloni, S. *et al.* Pretreatment with the monoacylglycerol lipase inhibitor URB602 protects from the long-term consequences of neonatal hypoxic-ischemic brain injury in rats. *Pediatr. Res.* **72,** 400–406 (2012).

78. Rossi, S. *et al.* Cannabinoid CB1 receptors regulate neuronal TNF-α effects in experimental autoimmune encephalomyelitis. *Brain. Behav. Immun.* **25,** 1242–1248 (2011).

79. Blázquez, C. *et al.* Loss of striatal type 1 cannabinoid receptors is a key pathogenic factor in Huntington's disease. *Brain J. Neurol.* **134,** 119–136 (2011).

80. Bari, M. *et al.* In vitro and in vivo models of Huntington's disease show alterations in the endocannabinoid system. *FEBS J.* **280,** 3376–3388 (2013).

81. Naydenov, A. V. *et al.* Genetic rescue of CB1 receptors on medium spiny neurons prevents loss of excitatory striatal synapses but not motor impairment in HD mice. *Neurobiol. Dis.* **71,** 140–150 (2014).

82. Loría, F. *et al.* An endocannabinoid tone limits excitotoxicity in vitro and in a model of multiple sclerosis. *Neurobiol. Dis.* **37,** 166–176 (2010).

83. Hernández-Torres, G. *et al.* A reversible and selective inhibitor of monoacylglycerol lipase ameliorates multiple sclerosis. *Angew. Chem. Int. Ed Engl.* **53,** 13765–13770 (2014).

84. Bernal-Chico, A. *et al.* Blockade of monoacylglycerol lipase inhibits oligodendrocyte excitotoxicity and prevents demyelination in vivo. *Glia* **63,** 163–176 (2015).

85. Pryce, G. & Baker, D. Endocannabinoids in Multiple Sclerosis and Amyotrophic Lateral Sclerosis. *Handb. Exp. Pharmacol.* **231,** 213–231 (2015).

86. Bedse, G., Romano, A., Lavecchia, A. M., Cassano, T. & Gaetani, S. The role of endocannabinoid signaling in the molecular mechanisms of neurodegeneration in Alzheimer's disease. *J. Alzheimers Dis. JAD* **43,** 1115–1136 (2015).

87. Fagan, S. G. & Campbell, V. A. The influence of cannabinoids on generic traits of neurodegeneration. *Br. J. Pharmacol.* **171,** 1347–1360 (2014).

88. Pascual, A. C., Martín-Moreno, A. M., Giusto, N. M., de Ceballos, M. L. & Pasquaré, S. J. Normal aging in rats and pathological aging in human Alzheimer's disease decrease FAAH activity: modulation by cannabinoid agonists. *Exp. Gerontol.* **60,** 92–99 (2014).

89. Desai, R. I. *et al.* Analysis of tolerance and behavioral/physical dependence during chronic CB1 agonist treatment: effects of CB1 agonists, antagonists, and noncannabinoid drugs. *J. Pharmacol. Exp. Ther.* **344,** 319–328 (2013).

90. McLaughlin, P. J. *et al.* Behavioral effects of the novel potent cannabinoid CB1 agonist AM 4054. *Pharmacol. Biochem. Behav.* **109,** 16–22 (2013).

91. Rubino, T. *et al.* Role in anxiety behavior of the endocannabinoid system in the prefrontal cortex. *Cereb. Cortex N. Y. N 1991* **18,** 1292–1301 (2008).

92. Schneider, M., Drews, E. & Koch, M. Behavioral effects in adult rats of chronic prepubertal treatment with the cannabinoid receptor agonist WIN 55,212-2. *Behav. Pharmacol.* **16,** 447–454 (2005).

93. Dissanayake, D. W. N., Zachariou, M., Marsden, C. A. & Mason, R. Auditory gating in rat hippocampus and medial prefrontal cortex: effect of the cannabinoid agonist WIN55,212-2. *Neuropharmacology* **55,** 1397–1404 (2008).

94. Hajós, M., Hoffmann, W. E. & Kocsis, B. Activation of cannabinoid-1 receptors disrupts sensory gating and neuronal oscillation: relevance to schizophrenia. *Biol. Psychiatry* **63,** 1075–1083 (2008).

95. Tornqvist, H. & Belfrage, P. Purification and some properties of a monoacylglycerol-hydrolyzing enzyme of rat adipose tissue. *J. Biol. Chem.* **251,** 813–819 (1976).

96. Dinh, T. P. *et al.* Brain monoglyceride lipase participating in endocannabinoid inactivation. *Proc. Natl. Acad. Sci.* **99,** 10819–10824 (2002).

97. Karlsson, M., Contreras, J. A., Hellman, U., Tornqvist, H. & Holm, C. cDNA Cloning, Tissue Distribution, and Identification of the Catalytic Triad of Monoglyceride Lipase EVOLUTIONARY RELATIONSHIP TO ESTERASES, LYSOPHOSPHOLIPASES, AND HALOPEROXIDASES. *J. Biol. Chem.* **272,** 27218–27223 (1997).

98. Karlsson, M., Tornqvist, H. & Holm, C. Expression, Purification, and Characterization of Histidine-Tagged Mouse Monoglyceride Lipase from Baculovirus-Infected Insect Cells. *Protein Expr. Purif.* **18,** 286–292 (2000).

99. Zvonok, N. *et al.* Covalent Inhibitors of Human Monoacylglycerol Lipase: Ligand-Assisted Characterization of the Catalytic Site by Mass Spectrometry and Mutational Analysis. *Chem. Biol.* **15,** 854–862 (2008).

100. Zvonok, N. *et al.* Full Mass Spectrometric Characterization of Human Monoacylglycerol Lipase Generated by Large-Scale Expression and Single-Step Purification. *J. Proteome Res.* **7,** 2158–2164 (2008).

101. Saario, S. M. *et al.* Characterization of the Sulfhydryl-Sensitive Site in the Enzyme Responsible for Hydrolysis of 2- Arachidonoyl-Glycerol in Rat Cerebellar Membranes. *Chem. Biol.* **12,** 649–656 (2005).

102. Laitinen, T. *et al.* Mutation of Cys242 of Human Monoacylglycerol Lipase Disrupts Balanced Hydrolysis of 1- and 2-Monoacylglycerols and Selectively Impairs Inhibitor Potency. *Mol. Pharmacol.* **85,** 510–519 (2014).

103. Dotsey, E. Y. *et al.* Peroxide-Dependent MGL Sulfenylation Regulates 2-AG-Mediated Endocannabinoid Signaling in Brain Neurons. *Chem. Biol.* **22,** 619–628 (2015).

104. Labar, G. *et al.* Crystal Structure of the Human Monoacylglycerol Lipase, a Key Actor in Endocannabinoid Signaling. *ChemBioChem* **11,** 218–227 (2010).

105. Bertrand, T. *et al.* Structural Basis for Human Monoglyceride Lipase Inhibition. *J. Mol. Biol.* **396,** 663–673 (2010).

106. Griebel, G. *et al.* Selective blockade of the hydrolysis of the endocannabinoid 2-arachidonoylglycerol impairs learning and memory performance while producing antinociceptive activity in rodents. *Sci. Rep.* **5,** 7642 (2015).

107. Schalk-Hihi, C. *et al.* Crystal structure of a soluble form of human monoglyceride lipase in complex with an inhibitor at 1.35 Å resolution. *Protein Sci. Publ. Protein Soc.* **20,** 670–683 (2011).

108. Triazolopyridine carboxamide derivatives, preparation thereof and therapeutic use thereof. at <http://www.google.com/patents/US7868007>

109. Aloulou, A. *et al.* Exploring the specific features of interfacial enzymology based on lipase studies. *Biochim. Biophys. Acta* **1761,** 995–1013 (2006).

110. Cambillau, C., Longhi, S., Nicolas, A. & Martinez, C. Acyl glycerol hydrolases: inhibitors, interface and catalysis. *Curr. Opin. Struct. Biol.* **6,** 449–455 (1996).

111. Reis, P., Holmberg, K., Watzke, H., Leser, M. E. & Miller, R. Lipases at interfaces: A review. *Adv. Colloid Interface Sci.* **147–148,** 237–250 (2009).

112. Tyukhtenko, S. *et al.* Specific Inter-residue Interactions as Determinants of Human Monoacylglycerol Lipase Catalytic Competency: A Role for Global Conformational Changes. *J. Biol. Chem.* jbc.M115.670257 (2015). doi:10.1074/jbc.M115.670257

113. Nasr, M. L. *et al.* Membrane phospholipid bilayer as a determinant of monoacylglycerol lipase kinetic profile and conformational repertoire. *Protein Sci. Publ. Protein Soc.* **22,** 774–787 (2013).

114. Finkel, T. Signal transduction by reactive oxygen species. *J. Cell Biol.* **194,** 7–15 (2011).

115. Patel, J. C. & Rice, M. E. Classification of $H_2O_2$as a neuromodulator that regulates striatal dopamine release on a subsecond time scale. *ACS Chem. Neurosci.* **3,** 991–1001 (2012).

116. Conte, M. L. & Carroll, K. S. The Redox Biochemistry of Protein Sulfenylation and Sulfinylation. *J. Biol. Chem.* **288,** 26480–26488 (2013).

117. Barford, D. The role of cysteine residues as redox-sensitive regulatory switches. *Curr. Opin. Struct. Biol.* **14,** 679–686 (2004).

118. Paulsen, C. E. & Carroll, K. S. Cysteine-mediated redox signaling: chemistry, biology, and tools for discovery. *Chem. Rev.* **113,** 4633–4679 (2013).

119. van Montfort, R. L. M., Congreve, M., Tisi, D., Carr, R. & Jhoti, H. Oxidation state of the active-site cysteine in protein tyrosine phosphatase 1B. *Nature* **423,** 773–777 (2003).

120. Sivaramakrishnan, S., Keerthi, K. & Gates, K. S. A chemical model for redox regulation of protein tyrosine phosphatase 1B (PTP1B) activity. *J. Am. Chem. Soc.* **127,** 10830–10831 (2005).

121. Lee, J.-W., Soonsanga, S. & Helmann, J. D. A complex thiolate switch regulates the Bacillus subtilis organic peroxide sensor OhrR. *Proc. Natl. Acad. Sci. U. S. A.* **104,** 8743–8748 (2007).

122. Carballal, S. *et al.* Sulfenic acid in human serum albumin. *Amino Acids* **32,** 543–551 (2007).

123. Yan, B., Yates, Z., Balland, A. & Kleemann, G. R. Human IgG1 Hinge Fragmentation as the Result of H2O2-mediated Radical Cleavage. *J. Biol. Chem.* **284,** 35390–35402 (2009).

124. Sun, Q.-A., Wang, B., Miyagi, M., Hess, D. T. & Stamler, J. S. Oxygen-coupled redox regulation of the skeletal muscle ryanodine receptor/Ca2+ release channel (RyR1): sites and nature of oxidative modification. *J. Biol. Chem.* **288,** 22961–22971 (2013).

125. Dickinson, B. C. & Chang, C. J. Chemistry and biology of reactive oxygen species in signaling or stress responses. *Nat. Chem. Biol.* **7,** 504–511 (2011).

126. Hohmann, A. G. *et al.* An endocannabinoid mechanism for stress-induced analgesia. *Nature* **435,** 1108–1112 (2005).

127. Connell, K., Bolton, N., Olsen, D., Piomelli, D. & Hohmann, A. G. Role of the basolateral nucleus of the amygdala in endocannabinoid-mediated stress-induced analgesia. *Neurosci. Lett.* **397,** 180–184 (2006).

128. Desroches, J., Guindon, J., Lambert, C. & Beaulieu, P. Modulation of the anti-nociceptive effects of 2-arachidonoyl glycerol by peripherally administered FAAH and MGL inhibitors in a neuropathic pain model. *Br. J. Pharmacol.* **155,** 913–924 (2008).

129. King, A. R. *et al.* URB602 Inhibits Monoacylglycerol Lipase and Selectively Blocks 2-Arachidonoylglycerol Degradation in Intact Brain Slices. *Chem. Biol.* **14,** 1357–1365 (2007).

130. Szabo, M., Agostino, M., Malone, D. T., Yuriev, E. & Capuano, B. The design, synthesis and biological evaluation of novel URB602 analogues as potential monoacylglycerol lipase inhibitors. *Bioorg. Med. Chem. Lett.* **21,** 6782–6787 (2011).

131. Long, J. Z. *et al.* Selective blockade of 2-arachidonoylglycerol hydrolysis produces cannabinoid behavioral effects. *Nat. Chem. Biol.* **5,** 37–44 (2009).

132. Long, J. Z., Nomura, D. K. & Cravatt, B. F. Characterization of Monoacylglycerol Lipase Inhibition Reveals Differences in Central and Peripheral Endocannabinoid Metabolism. *Chem. Biol.* **16,** 744–753 (2009).

133. Schlosburg, J. E. *et al.* Chronic monoacylglycerol lipase blockade causes functional antagonism of the endocannabinoid system. *Nat. Neurosci.* **13,** 1113–1119 (2010).

134. Long, J. Z. *et al.* Dual blockade of FAAH and MAGL identifies behavioral processes regulated by endocannabinoid crosstalk in vivo. *Proc. Natl. Acad. Sci.* **106,** 20270–20275 (2009).

135. Chang, J. W. *et al.* Highly Selective Inhibitors of Monoacylglycerol Lipase Bearing a Reactive Group that Is Bioisosteric with Endocannabinoid Substrates. *Chem. Biol.* **19,** 579–588 (2012).

136. Chang, J. W., Cognetta, A. B., Niphakis, M. J. & Cravatt, B. F. Proteome-Wide Reactivity Profiling Identifies Diverse Carbamate Chemotypes Tuned for Serine Hydrolase Inhibition. *ACS Chem. Biol.* **8,** 1590–1599 (2013).

137. Niphakis, M. J. *et al.* Evaluation of NHS Carbamates as a Potent and Selective Class of Endocannabinoid Hydrolase Inhibitors. *ACS Chem. Neurosci.* **4,** 1322–1332 (2013).

138. Pasquarelli, N. *et al.* Comparative biochemical characterization of the monoacylglycerol lipase inhibitor KML29 in brain, spinal cord, liver, spleen, fat and muscle tissue. *Neuropharmacology* **91,** 148–156 (2015).

139. Aaltonen, N. *et al.* Piperazine and Piperidine Triazole Ureas as Ultrapotent and Highly Selective Inhibitors of Monoacylglycerol Lipase. *Chem. Biol.* **20,** 379–390 (2013).

140. Käsnänen, H. *et al.* 1,3,4-Oxadiazol-2-ones as fatty-acid amide hydrolase and monoacylglycerol lipase inhibitors: Synthesis, in vitro evaluation and insight into potency and selectivity determinants by molecular modelling. *Eur. J. Pharm. Sci.* **49,** 423–433 (2013).

141. Ortar, G. *et al.* Biaryl tetrazolyl ureas as inhibitors of endocannabinoid metabolism: Modulation at the N-portion and distal phenyl ring. *Eur. J. Med. Chem.* **63,** 118–132 (2013).

142. Tuccinardi, T. *et al.* Identification and characterization of a new reversible MAGL inhibitor. *Bioorg. Med. Chem.* **22,** 3285–3291 (2014).

143. Matuszak, N., Muccioli, G. G., Labar, G. & Lambert, D. M. Synthesis and in Vitro Evaluation of N-Substituted Maleimide Derivatives as Selective Monoglyceride Lipase Inhibitors. *J. Med. Chem.* **52,** 7410–7420 (2009).

144. Labar, G., Bauvois, C., Muccioli, G. G., Wouters, J. & Lambert, D. M. Disulfiram is an Inhibitor of Human Purified Monoacylglycerol Lipase, the Enzyme Regulating 2-Arachidonoylglycerol Signaling. *ChemBioChem* **8,** 1293–1297 (2007).

145. Kapanda, C. N., Muccioli, G. G., Labar, G., Poupaert, J. H. & Lambert, D. M. Bis(dialkylaminethiocarbonyl)disulfides as Potent and Selective Monoglyceride Lipase Inhibitors. *J. Med. Chem.* **52,** 7310–7314 (2009).

146. King, A. *et al.* A critical cysteine residue in monoacylglycerol lipase is targeted by a new class of isothiazolinone-based enzyme inhibitors. *Br. J. Pharmacol.* **157,** 974–983 (2009).

147. Matuszak, N., Es Saadi, B., Labar, G., Marchand-Brynaert, J. & Lambert, D. M. Benzisothiazolinone as a useful template for the design of new monoacylglycerol lipase inhibitors: Investigation of the target residues and comparison with octhilinone. *Bioorg. Med. Chem. Lett.* **21,** 7321–7324 (2011).

148. King, A. R. *et al.* Discovery of Potent and Reversible Monoacylglycerol Lipase Inhibitors. *Chem. Biol.* **16,** 1045–1052 (2009).

149. Chicca, A., Marazzi, J. & Gertsch, J. The antinociceptive triterpene β-amyrin inhibits 2-arachidonoylglycerol (2-AG) hydrolysis without directly targeting cannabinoid receptors. *Br. J. Pharmacol.* **167,** 1596–1608 (2012).

150. Sivaramakrishnan, S., Keerthi, K. & Gates, K. S. A chemical model for redox regulation of protein tyrosine phosphatase 1B (PTP1B) activity. *J. Am. Chem. Soc.* **127,** 10830–10831 (2005).

151. Barducci, A., Bussi, G. & Parrinello, M. Well-tempered metadynamics: a smoothly converging and tunable free-energy method. *Phys. Rev. Lett.* **100,** 020603 (2008).

152. Barducci, A., Bonomi, M. & Parrinello, M. Linking well-tempered metadynamics simulations with experiments. *Biophys. J.* **98,** L44–46 (2010).

153. Berendsen, H. J. C., Postma, J. P. M., van Gusteren, W. F. & Hermans, J. Interaction models for water in relation to protein hydration.

154. Jorgensen, W. L., Maxwell, D. S. & Tirado-Rives, J. Development and Testing of the OPLS All-Atom Force Field on Conformational Energetics and Properties of Organic Liquids. *J. Am. Chem. Soc.* **118,** 11225–11236 (1996).

155. Lomize, M. A., Lomize, A. L., Pogozheva, I. D. & Mosberg, H. I. OPM: orientations of proteins in membranes database. *Bioinforma. Oxf. Engl.* **22,** 623–625 (2006).

156. Matuszak, N., Es Saadi, B., Labar, G., Marchand-Brynaert, J. & Lambert, D. M. Benzisothiazolinone as a useful template for the design of new monoacylglycerol lipase inhibitors: Investigation of the target residues and comparison with octhilinone. *Bioorg. Med. Chem. Lett.* **21,** 7321–7324 (2011).

157. Laio, A. & Parrinello, M. Escaping free-energy minima. *Proc. Natl. Acad. Sci.* **99,** 12562–12566 (2002).

158. Raiteri, P., Laio, A., Gervasio, F. L., Micheletti, C. & Parrinello, M. Efficient Reconstruction of Complex Free Energy Landscapes by Multiple Walkers Metadynamics†. *J. Phys. Chem. B* **110,** 3533–3539 (2006).

159. Bonomi, M. *et al.* PLUMED: A portable plugin for free-energy calculations with molecular dynamics. *Comput. Phys. Commun.* **180,** 1961–1972 (2009).

160. Berendsen, H. J. C., van der Spoel, D. & van Drunen, R. GROMACS: A message-passing parallel molecular dynamics implementation. *Comput. Phys. Commun.* **91,** 43–56 (1995).

161. Iqbal, K., Liu, F. & Gong, C.-X. Tau and neurodegenerative disease: the story so far. *Nat. Rev. Neurol.* **advance online publication,** (2015).

162. Heneka, M. T. *et al.* Neuroinflammation in Alzheimer's disease. *Lancet Neurol.* **14,** 388–405 (2015).

163. Hatanaka, H. *et al.* Differences in peripheral oxidative stress markers in Alzheimer's disease, vascular dementia and mixed dementia patients. *Geriatr. Gerontol. Int.* **15,** 53–58 (2015).

164. Arimon, M. *et al.* Oxidative stress and lipid peroxidation are upstream of amyloid pathology. *Neurobiol. Dis.* **84,** 109–119 (2015).

165. Praticò, D. Evidence of Oxidative Stress in Alzheimer's Disease Brain and Antioxidant Therapy. *Ann. N. Y. Acad. Sci.* **1147,** 70–78 (2008).

166. Giacobini, E. Cholinergic function and Alzheimer's disease. *Int. J. Geriatr. Psychiatry* **18,** S1–5 (2003).

167. Morphy, R. & Rankovic, Z. Designed multiple ligands. An emerging drug discovery paradigm. *J. Med. Chem.* **48,** 6523–6543 (2005).

168. Benito, C. *et al.* Cannabinoid CB2 receptors and fatty acid amide hydrolase are selectively overexpressed in neuritic plaque-associated glia in Alzheimer's disease brains. *J. Neurosci. Off. J. Soc. Neurosci.* **23,** 11136–11141 (2003).

169. Fowler, C. J., Rojo, M. L. & Rodriguez-Gaztelumendi, A. Modulation of the endocannabinoid system: neuroprotection or neurotoxicity? *Exp. Neurol.* **224,** 37–47 (2010).

170. Rivers-Auty, J. R., Smith, P. F. & Ashton, J. C. The cannabinoid CB2 receptor agonist GW405833 does not ameliorate brain damage induced by hypoxia-ischemia in rats. *Neurosci. Lett.* **569,** 104–109 (2014).

171. Cravatt, B. F. *et al.* Molecular characterization of an enzyme that degrades neuromodulatory fatty-acid amides. *Nature* **384,** 83–87 (1996).

172. Patricelli, M. P., Lashuel, H. A., Giang, D. K., Kelly, J. W. & Cravatt, B. F. Comparative characterization of a wild type and transmembrane domain-deleted fatty acid amide hydrolase: identification of the transmembrane domain as a site for oligomerization. *Biochemistry (Mosc.)* **37,** 15177–15187 (1998).

173. Patricelli, M. P. & Cravatt, B. F. Clarifying the Catalytic Roles of Conserved Residues in the Amidase Signature Family. *J. Biol. Chem.* **275,** 19177–19184 (2000).

174. McKinney, M. K. & Cravatt, B. F. Evidence for Distinct Roles in Catalysis for Residues of the Serine-Serine-Lysine Catalytic Triad of Fatty Acid Amide Hydrolase. *J. Biol. Chem.* **278,** 37393–37399 (2003).

175. Patricelli, M. P. & Cravatt, B. F. Fatty Acid Amide Hydrolase Competitively Degrades Bioactive Amides and Esters through a Nonconventional Catalytic Mechanism. *Biochemistry (Mosc.)* **38,** 14125–14130 (1999).

176. Carter, P. & Wells, J. A. Dissecting the catalytic triad of a serine protease. *Nature* **332,** 564–568 (1988).

177. Craik, C. S., Roczniak, S., Largman, C. & Rutter, W. J. The catalytic role of the active site aspartic acid in serine proteases. *Science* **237,** 909–913 (1987).

178. Lodola, A. *et al.* QM/MM modelling of oleamide hydrolysis in fatty acid amide hydrolase (FAAH) reveals a new mechanism of nucleophile activation. *Chem. Commun. Camb. Engl.* 4399–4401 (2005). doi:10.1039/b503887a

179. Holt, S., Nilsson, J., Omeir, R., Tiger, G. & Fowler, C. J. Effects of pH on the inhibition of fatty acid amidohydrolase by ibuprofen. *Br. J. Pharmacol.* **133,** 513–520 (2001).

180. Cravatt, B. F. *et al.* Supersensitivity to anandamide and enhanced endogenous cannabinoid signaling in mice lacking fatty acid amide hydrolase. *Proc. Natl. Acad. Sci.* **98,** 9371–9376 (2001).

181. Desarnaud, F., Cadas, H. & Piomelli, D. Anandamide Amidohydrolase Activity in Rat Brain Microsomes IDENTIFICATION AND PARTIAL CHARACTERIZATION. *J. Biol. Chem.* **270,** 6030–6035 (1995).

182. Ueda, N., Kurahashi, Y., Yamamoto, S. & Tokunaga, T. Partial purification and characterization of the porcine brain enzyme hydrolyzing and synthesizing anandamide. *J. Biol. Chem.* **270,** 23823–23827 (1995).

183. Hillard, C. J., Wilkison, D. M., Edgemond, W. S. & Campbell, W. B. Characterization of the kinetics and distribution of N-arachidonylethanolamine (anandamide) hydrolysis by rat brain. *Biochim. Biophys. Acta BBA - Lipids Lipid Metab.* **1257,** 249–256 (1995).

184. Maccarrone, M. *et al.* Anandamide hydrolysis by human cells in culture and brain. *J. Biol. Chem.* **273,** 32332–32339 (1998).

185. Bracey, M. H., Hanson, M. A., Masuda, K. R., Stevens, R. C. & Cravatt, B. F. Structural adaptations in a membrane enzyme that terminates endocannabinoid signaling. *Science* **298,** 1793–1796 (2002).

186. Kono, M. *et al.* Synthesis, SAR study, and biological evaluation of a series of piperazine ureas as fatty acid amide hydrolase (FAAH) inhibitors. *Bioorg. Med. Chem.* **21,** 28–41 (2013).

187. Otrubova, K. *et al.* Rational design of fatty acid amide hydrolase inhibitors that act by covalently bonding to two active site residues. *J. Am. Chem. Soc.* **135,** 6289–6299 (2013).

188. Mileni, M. *et al.* X-ray crystallographic analysis of alpha-ketoheterocycle inhibitors bound to a humanized variant of fatty acid amide hydrolase. *J. Med. Chem.* **53,** 230–240 (2010).

189. Mileni, M. *et al.* Binding and inactivation mechanism of a humanized fatty acid amide hydrolase by alpha-ketoheterocycle inhibitors revealed from cocrystal structures. *J. Am. Chem. Soc.* **131,** 10497–10506 (2009).

190. Ezzili, C. *et al.* Reversible competitive α-ketoheterocycle inhibitors of fatty acid amide hydrolase containing additional conformational constraints in the acyl side chain: orally active, long-acting analgesics. *J. Med. Chem.* **54,** 2805–2822 (2011).

191. Ahn, K. *et al.* Discovery and characterization of a highly selective FAAH inhibitor that reduces inflammatory pain. *Chem. Biol.* **16,** 411–420 (2009).

192. Mor, M. *et al.* Cyclohexylcarbamic acid 3'- or 4'-substituted biphenyl-3-yl esters as fatty acid amide hydrolase inhibitors: synthesis, quantitative structure-activity relationships, and molecular modeling studies. *J. Med. Chem.* **47,** 4998–5008 (2004).

193. Tarzia, G. *et al.* Design, synthesis, and structure-activity relationships of alkylcarbamic acid aryl esters, a new class of fatty acid amide hydrolase inhibitors. *J. Med. Chem.* **46,** 2352–2360 (2003).

194. Mileni, M. *et al.* Crystal structure of fatty acid amide hydrolase bound to the carbamate inhibitor URB597: discovery of a deacylating water molecule and insight into enzyme inactivation. *J. Mol. Biol.* **400,** 743–754 (2010).

195. Clapper, J. R. *et al.* The fatty-acid amide hydrolase inhibitor URB597 does not affect triacylglycerol hydrolysis in rat tissues. *Pharmacol. Res.* **54,** 341–344 (2006).

196. Russo, R. *et al.* The fatty acid amide hydrolase inhibitor URB597 (cyclohexylcarbamic acid 3'-carbamoylbiphenyl-3-yl ester) reduces neuropathic pain after oral administration in mice. *J. Pharmacol. Exp. Ther.* **322,** 236–242 (2007).

197. Jayamanne, A. *et al.* Actions of the FAAH inhibitor URB597 in neuropathic and inflammatory chronic pain models. *Br. J. Pharmacol.* **147,** 281–288 (2006).

198. Piomelli, D. *et al.* Pharmacological profile of the selective FAAH inhibitor KDS-4103 (URB597). *CNS Drug Rev.* **12,** 21–38 (2006).

199. Bortolato, M. *et al.* Antidepressant-like activity of the fatty acid amide hydrolase inhibitor URB597 in a rat model of chronic mild stress. *Biol. Psychiatry* **62,** 1103–1110 (2007).

200. Kathuria, S. *et al.* Modulation of anxiety through blockade of anandamide hydrolysis. *Nat. Med.* **9,** 76–81 (2003).

201. Vacondio, F. *et al.* Structure-property relationships of a class of carbamate-based fatty acid amide hydrolase (FAAH) inhibitors: chemical and biological stability. *ChemMedChem* **4,** 1495–1504 (2009).

202. Clapper, J. R. *et al.* Anandamide suppresses pain initiation through a peripheral endocannabinoid mechanism. *Nat. Neurosci.* **13,** 1265–1270 (2010).

203. Alexander, J. P. & Cravatt, B. F. The putative endocannabinoid transport blocker LY2183240 is a potent inhibitor of FAAH and several other brain serine hydrolases. *J. Am. Chem. Soc.* **128,** 9699–9704 (2006).

204. Even, L. & Hoornaert, C. Triazolopyridine Carboxamide Derivatives and Triazolopyrimidine Carboxamide Derivatives, Preparation Thereof and Therapeutic Use Thereof. (2008). at <https://patentscope.wipo.int/search/en/detail.jsf%3Bjsessionid=F69F2C9F1F223EC8ADD1D9719BEDC0BC.wapp2?docId=WO2008145843&recNum=51&office=&queryString=&prevFilter=%26fq%3DOF%3AWO%26fq%3DICF_M%3A%22C07D%22%26fq%3DPAF_M%3A%22SANOFI-AVENTIS%22%26fq%3DDP%3A2008&sortOption=Relevance&maxRec=70>

205. Triazolopyridine carboxamide derivatives and triazolopyrimidine carboxamide derivatives, preparation thereof and therapeutic use thereof. at <http://www.google.com/patents/WO2008145839A8>

206. Matsumoto, T., Kori, M., Miyazaki, J. & Kiyota, Y. Amide Compound. (2006). at <https://patentscope.wipo.int/search/en/detail.jsf?docId=WO2006054652>

207. N-heteroarylpiperazinyl ureas as modulators of fatty acid amide hydrolase. at <http://www.google.com/patents/WO2007005510A1>

208. Ahn, K. *et al.* Novel mechanistic class of fatty acid amide hydrolase inhibitors with remarkable selectivity. *Biochemistry (Mosc.)* **46,** 13019–13030 (2007).

209. Boger, D. L. *et al.* Discovery of a potent, selective, and efficacious class of reversible alpha-ketoheterocycle inhibitors of fatty acid amide hydrolase effective as analgesics. *J. Med. Chem.* **48,** 1849–1856 (2005).

210. Lichtman, A. H. *et al.* Reversible Inhibitors of Fatty Acid Amide Hydrolase That Promote Analgesia: Evidence for an Unprecedented Combination of Potency and Selectivity. *J. Pharmacol. Exp. Ther.* **311,** 441–448 (2004).

211. Timmons, A. *et al.* Novel ketooxazole based inhibitors of fatty acid amide hydrolase (FAAH). *Bioorg. Med. Chem. Lett.* **18,** 2109–2113 (2008).

212. Kimball, F. S. *et al.* Optimization of alpha-ketooxazole inhibitors of fatty acid amide hydrolase. *J. Med. Chem.* **51,** 937–947 (2008).

213. Hardouin, C. *et al.* Structure-activity relationships of alpha-ketooxazole inhibitors of fatty acid amide hydrolase. *J. Med. Chem.* **50,** 3359–3368 (2007).

214. DeMartino, J. K., Garfunkle, J., Hochstatter, D. G., Cravatt, B. F. & Boger, D. L. Exploration of a fundamental substituent effect of alpha-ketoheterocycle enzyme

inhibitors: Potent and selective inhibitors of fatty acid amide hydrolase. *Bioorg. Med. Chem. Lett.* **18,** 5842–5846 (2008).

215. Romero, F. A. *et al.* Potent and selective alpha-ketoheterocycle-based inhibitors of the anandamide and oleamide catabolizing enzyme, fatty acid amide hydrolase. *J. Med. Chem.* **50,** 1058–1068 (2007).

216. Romero, F. A., Hwang, I. & Boger, D. L. Delineation of a fundamental alpha-ketoheterocycle substituent effect for use in the design of enzyme inhibitors. *J. Am. Chem. Soc.* **128,** 14004–14005 (2006).

217. 2-keto-oxazoles as modulators of fatty acid amide hydrolase. at <http://www.google.com/patents/WO2007061862A3>

218. Slaymaker, I. M. *et al.* Correlation of inhibitor effects on enzyme activity and thermal stability for the integral membrane protein fatty acid amide hydrolase. *Bioorg. Med. Chem. Lett.* **18,** 5847–5850 (2008).

219. Adams, J. *et al.* Boronic Acids and Esters as Inhibitors of Fatty Acid Amide Hydrolase. (2008). at <https://patentscope.wipo.int/search/en/detail.jsf?docId=WO2008063300>

220. Behnke, M. *et al.* Inhibitors of Fatty Acid Amide Hydrolase. (2009). at <https://patentscope.wipo.int/search/en/detail.jsf?docId=WO2009126691>

221. Urbach, A., Muccioli, G. G., Stern, E., Lambert, D. M. & Marchand-Brynaert, J. 3-Alkenyl-2-azetidinones as fatty acid amide hydrolase inhibitors. *Bioorg. Med. Chem. Lett.* **18,** 4163–4167 (2008).

222. Feledziak, M. *et al.* beta-Lactams derived from a carbapenem chiron are selective inhibitors of human fatty acid amide hydrolase versus human monoacylglycerol lipase. *J. Med. Chem.* **52,** 7054–7068 (2009).

223. Mendel, B. & Rudney, H. ON THE TYPE OF CHOLINESTERASE PRESENT IN BRAIN TISSUE. *Science* **98,** 201–202 (1943).

224. Tago, H., Maeda, T., McGeer, P. L. & Kimura, H. Butyrylcholinesterase-rich neurons in rat brain demonstrated by a sensitive histochemical method. *J. Comp. Neurol.* **325,** 301–312 (1992).

225. Darvesh, S., Grantham, D. L. & Hopkins, D. A. Distribution of butyrylcholinesterase in the human amygdala and hippocampal formation. *J. Comp. Neurol.* **393,** 374–390 (1998).

226. Darvesh, S. *et al.* Cholinesterases in cardiac ganglia and modulation of canine intrinsic cardiac neuronal activity. *J. Auton. Nerv. Syst.* **71,** 75–84 (1998).

227. Mesulam, M.-M. *et al.* Acetylcholinesterase knockouts establish central cholinergic pathways and can use butyrylcholinesterase to hydrolyze acetylcholine. *Neuroscience* **110,** 627–639 (2002).

228. Layer, P. G. Cholinesterases during development of the avian nervous system. *Cell. Mol. Neurobiol.* **11,** 7–33 (1991).

229. Kostovic, I. & Goldman-Rakic, P. S. Transient cholinesterase staining in the mediodorsal nucleus of the thalamus and its connections in the developing human and monkey brain. *J. Comp. Neurol.* **219,** 431–447 (1983).

230. Dubovy, P. & Haninec, P. Non-specific cholinesterase activity of the developing peripheral nerves and its possible function in cells in intimate contact with growing axons of chick embryo. *Int. J. Dev. Neurosci. Off. J. Int. Soc. Dev. Neurosci.* **8,** 589–602 (1990).

231. Mesulam, M., Guillozet, A., Shaw, P. & Quinn, B. Widely spread butyrylcholinesterase can hydrolyze acetylcholine in the normal and Alzheimer brain. *Neurobiol. Dis.* **9,** 88–93 (2002).

232. Li, B. *et al.* Abundant tissue butyrylcholinesterase and its possible function in the acetylcholinesterase knockout mouse. *J. Neurochem.* **75,** 1320–1331 (2000).

233. Nachon, F. *et al.* Crystal structures of human cholinesterases in complex with huprine W and tacrine: elements of specificity for anti-Alzheimer's drugs targeting acetyl- and butyryl-cholinesterase. *Biochem. J.* **453,** 393–399 (2013).

234. Nicolet, Y., Lockridge, O., Masson, P., Fontecilla-Camps, J. C. & Nachon, F. Crystal Structure of Human Butyrylcholinesterase and of Its Complexes with Substrate and Products. *J. Biol. Chem.* **278,** 41141–41147 (2003).

235. Cheung, J. *et al.* Structures of human acetylcholinesterase in complex with pharmacologically important ligands. *J. Med. Chem.* **55,** 10282–10286 (2012).

236. Ordentlich, A. *et al.* Dissection of the human acetylcholinesterase active center determinants of substrate specificity. Identification of residues constituting the anionic site, the hydrophobic site, and the acyl pocket. *J. Biol. Chem.* **268,** 17083–17095 (1993).

237. Johnson, G. & Moore, S. W. The peripheral anionic site of acetylcholinesterase: structure, functions and potential role in rational drug design. *Curr. Pharm. Des.* **12,** 217–225 (2006).

238. Hosea, N. A. *et al.* Aspartate 74 as a primary determinant in acetylcholinesterase governing specificity to cationic organophosphonates. *Biochemistry (Mosc.)* **35,** 10995–11004 (1996).

239. Mallender, W. D., Szegletes, T. & Rosenberry, T. L. Acetylthiocholine binds to asp74 at the peripheral site of human acetylcholinesterase as the first step in the catalytic pathway. *Biochemistry (Mosc.)* **39,** 7753–7763 (2000).

240. Shafferman, A. *et al.* Mutagenesis of human acetylcholinesterase. Identification of residues involved in catalytic activity and in polypeptide folding. *J. Biol. Chem.* **267,** 17640–17648 (1992).

241. Brus, B. *et al.* Discovery, biological evaluation, and crystal structure of a novel nanomolar selective butyrylcholinesterase inhibitor. *J. Med. Chem.* **57,** 8167–8179 (2014).

242. Knapp, M. J. *et al.* A 30-week randomized controlled trial of high-dose tacrine in patients with Alzheimer's disease. The Tacrine Study Group. *JAMA* **271,** 985–991 (1994).

243. Watkins, P. B., Zimmerman, H. J., Knapp, M. J., Gracon, S. I. & Lewis, K. W. Hepatotoxic effects of tacrine administration in patients with Alzheimer's disease. *JAMA* **271,** 992–998 (1994).

244. Winker, M. A. Tacrine for Alzheimer's disease. Which patient, what dose? *JAMA* **271,** 1023–1024 (1994).

245. Barreiro, E. J. *et al.* Design, synthesis, and pharmacological profile of novel fused pyrazolo[4,3-d]pyridine and pyrazolo[3,4-b][1,8]naphthyridine isosteres: a new class of

potent and selective acetylcholinesterase inhibitors. *J. Med. Chem.* **46,** 1144–1152 (2003).

246. Campiani, G. *et al.* Development of molecular probes for the identification of extra interaction sites in the mid-gorge and peripheral sites of butyrylcholinesterase (BuChE). Rational design of novel, selective, and highly potent BuChE inhibitors. *J. Med. Chem.* **48,** 1919–1929 (2005).

247. Savini, L. *et al.* Novel and potent tacrine-related hetero- and homobivalent ligands for acetylcholinesterase and butyrylcholinesterase. *Bioorg. Med. Chem. Lett.* **11,** 1779–1782 (2001).

248. Savini, L. *et al.* Specific Targeting of Acetylcholinesterase and Butyrylcholinesterase Recognition Sites. Rational Design of Novel, Selective, and Highly Potent Cholinesterase Inhibitors. *J. Med. Chem.* **46,** 1–4 (2003).

249. Muñoz-Ruiz, P. *et al.* Design, synthesis, and biological evaluation of dual binding site acetylcholinesterase inhibitors: new disease-modifying agents for Alzheimer's disease. *J. Med. Chem.* **48,** 7223–7233 (2005).

250. Enz, A., Boddeke, H., Gray, J. & Spiegel, R. Pharmacologic and clinicopharmacologic properties of SDZ ENA 713, a centrally selective acetylcholinesterase inhibitor. *Ann. N. Y. Acad. Sci.* **640,** 272–275 (1991).

251. Weinstock, M., Razin, M., Chorev, M. & Enz, A. Pharmacological evaluation of phenyl-carbamates as CNS-selective acetylcholinesterase inhibitors. *J. Neural Transm. Suppl.* **43,** 219–225 (1994).

252. Lin, G., Lai, C. Y. & Liao, W. C. Molecular recognition by acetylcholinesterase at the peripheral anionic site: structure-activity relationships for inhibitions by aryl carbamates. *Bioorg. Med. Chem.* **7,** 2683–2689 (1999).

253. Belluti, F. *et al.* Cholinesterase inhibitors: xanthostigmine derivatives blocking the acetylcholinesterase-induced beta-amyloid aggregation. *J. Med. Chem.* **48,** 4444–4456 (2005).

254. Piazzi, L. *et al.* Cholinesterase inhibitors: SAR and enzyme inhibitory activity of 3-[omega-(benzylmethylamino)alkoxy]xanthen-9-ones. *Bioorg. Med. Chem.* **15,** 575–585 (2007).

255. Schalk, I. *et al.* 6-Coumarin diazonium salt: a specific affinity label of the Torpedo acetylcholinesterase peripheral site. *Mol. Pharmacol.* **48,** 1063–1067 (1995).

256. Radić, Z. & Taylor, P. The influence of peripheral site ligands on the reaction of symmetric and chiral organophosphates with wildtype and mutant acetylcholinesterases. *Chem. Biol. Interact.* **119-120,** 111–117 (1999).

257. Fallarero, A. *et al.* Inhibition of acetylcholinesterase by coumarins: the case of coumarin 106. *Pharmacol. Res.* **58,** 215–221 (2008).

258. Piazzi, L. *et al.* 3-(4-[[Benzyl(methyl)amino]methyl]phenyl)-6,7-dimethoxy-2H-2-chromenone (AP2238) inhibits both acetylcholinesterase and acetylcholinesterase-induced beta-amyloid aggregation: a dual function lead for Alzheimer's disease therapy. *J. Med. Chem.* **46,** 2279–2282 (2003).

259. Rizzo, S. *et al.* Targeting Alzheimer's disease: Novel indanone hybrids bearing a pharmacophoric fragment of AP2238. *Bioorg. Med. Chem.* **18,** 1749–1760 (2010).

260. Montanari, S. *et al.* Multitarget Strategy to Address Alzheimer's Disease: Design, Synthesis, Biological Evaluation, and Computational Studies of Coumarin-Based Derivatives. *ChemMedChem* n/a–n/a (2015). doi:10.1002/cmdc.201500392

261. Piazzi, L. *et al.* Multi-target-directed coumarin derivatives: hAChE and BACE1 inhibitors as potential anti-Alzheimer compounds. *Bioorg. Med. Chem. Lett.* **18,** 423–426 (2008).

262. Farina, R. *et al.* Structure-Based Design and Optimization of Multitarget-Directed 2H-Chromen-2-one Derivatives as Potent Inhibitors of Monoamine Oxidase B and Cholinesterases. *J. Med. Chem.* **58,** 5561–5578 (2015).

263. Rochais, C. *et al.* Novel Multitarget-Directed Ligands (MTDLs) with Acetylcholinesterase (AChE) Inhibitory and Serotonergic Subtype 4 Receptor (5-HT4R) Agonist Activities As Potential Agents against Alzheimer's Disease: The Design of Donecopride. *J. Med. Chem.* **58,** 3172–3187 (2015).

264. Makhaeva, G. F. *et al.* Conjugates of γ-Carbolines and Phenothiazine as new selective inhibitors of butyrylcholinesterase and blockers of NMDA receptors for Alzheimer Disease. *Sci. Rep.* **5,** 13164 (2015).

265. Rampa, A. *et al.* The First Dual ChE/FAAH Inhibitors: New Perspectives for Alzheimer's Disease? *ACS Med. Chem. Lett.* **3,** 182–186 (2012).

266. Rizzo, S. *et al.* Structure-activity relationships and binding mode in the human acetylcholinesterase active site of pseudo-irreversible inhibitors related to xanthostigmine. *ChemMedChem* **4,** 670–679 (2009).

267. Więckowska, A., Bajda, M., Guzior, N. & Malawska, B. Novel alkyl- and arylcarbamate derivatives with N-benzylpiperidine and N-benzylpiperazine moieties as cholinesterases inhibitors. *Eur. J. Med. Chem.* **45,** 5602–5611 (2010).

268. Friesner, R. A. *et al.* Glide: A New Approach for Rapid, Accurate Docking and Scoring. 1. Method and Assessment of Docking Accuracy. *J. Med. Chem.* **47,** 1739–1749 (2004).

269. Halgren, T. A. *et al.* Glide: A New Approach for Rapid, Accurate Docking and Scoring. 2. Enrichment Factors in Database Screening. *J. Med. Chem.* **47,** 1750–1759 (2004).

270. Hong, W. & Guan, K.-L. The YAP and TAZ transcription co-activators: Key downstream effectors of the mammalian Hippo pathway. *Semin. Cell Dev. Biol.* **23,** 785–793 (2012).

271. Couzens, A. L. *et al.* Protein Interaction Network of the Mammalian Hippo Pathway Reveals Mechanisms of Kinase-Phosphatase Interactions. *Sci Signal* **6,** rs15–rs15 (2013).

272. Creasy, C. L. & Chernoff, J. Cloning and characterization of a member of the MST subfamily of Ste20-like kinases. *Gene* **167,** 303–306 (1995).

273. Udan, R. S., Kango-Singh, M., Nolo, R., Tao, C. & Halder, G. Hippo promotes proliferation arrest and apoptosis in the Salvador/Warts pathway. *Nat. Cell Biol.* **5,** 914–920 (2003).

274. Xu, T., Wang, W., Zhang, S., Stewart, R. A. & Yu, W. Identifying tumor suppressors in genetic mosaics: the Drosophila lats gene encodes a putative protein kinase. *Dev. Camb. Engl.* **121,** 1053–1063 (1995).

275. Creasy, C. L. & Chernoff, J. Cloning and characterization of a human protein kinase with homology to Ste20. *J. Biol. Chem.* **270,** 21695–21700 (1995).

276. Densham, R. M. *et al.* MST Kinases Monitor Actin Cytoskeletal Integrity and Signal via c-Jun N-Terminal Kinase Stress-Activated Kinase To Regulate p21Waf1/Cip1 Stability. *Mol. Cell. Biol.* **29,** 6380–6390 (2009).

277. Hergovich, A., Schmitz, D. & Hemmings, B. A. The human tumour suppressor LATS1 is activated by human MOB1 at the membrane. *Biochem. Biophys. Res. Commun.* **345,** 50–58 (2006).

278. Yin, F. *et al.* Spatial organization of Hippo signaling at the plasma membrane mediated by the tumor suppressor Merlin/NF2. *Cell* **154,** 1342–1355 (2013).

279. Meng, Z. *et al.* MAP4K family kinases act in parallel to MST1/2 to activate LATS1/2 in the Hippo pathway. *Nat. Commun.* **6,** 8357 (2015).

280. Zheng, Y. *et al.* Identification of Happyhour/MAP4K as Alternative Hpo/Mst-like Kinases in the Hippo Kinase Cascade. *Dev. Cell* **34,** 642–655 (2015).

281. Kanai, F. *et al.* TAZ: a novel transcriptional co-activator regulated by interactions with 14-3-3 and PDZ domain proteins. *EMBO J.* **19,** 6778–6791 (2000).

282. Schumacher, B., Skwarczynska, M., Rose, R. & Ottmann, C. Structure of a 14-3-3σ-YAP phosphopeptide complex at 1.15 A resolution. *Acta Crystallograph. Sect. F Struct. Biol. Cryst. Commun.* **66,** 978–984 (2010).

283. Sambandam, S. A. T. *et al.* 14-3-3σ regulates keratinocyte proliferation and differentiation by modulating Yap1 cellular localization. *J. Invest. Dermatol.* **135,** 1621–1628 (2015).

284. Liu, C.-Y. *et al.* The hippo tumor pathway promotes TAZ degradation by phosphorylating a phosphodegron and recruiting the SCF{beta}-TrCP E3 ligase. *J. Biol. Chem.* **285,** 37159–37169 (2010).

285. Oh, H. & Irvine, K. D. In vivo regulation of Yorkie phosphorylation and localization. *Dev. Camb. Engl.* **135,** 1081–1088 (2008).

286. Zhao, B., Li, L., Tumaneng, K., Wang, C.-Y. & Guan, K.-L. A coordinated phosphorylation by Lats and CK1 regulates YAP stability through SCF(beta-TRCP). *Genes Dev.* **24,** 72–85 (2010).

287. Guo, T. *et al.* A novel partner of Scalloped regulates Hippo signaling via antagonizing Scalloped-Yorkie activity. *Cell Res.* **23,** 1201–1214 (2013).

288. Koontz, L. M. *et al.* The Hippo effector Yorkie controls normal tissue growth by antagonizing scalloped-mediated default repression. *Dev. Cell* **25,** 388–401 (2013).

289. Ota, M. & Sasaki, H. Mammalian Tead proteins regulate cell proliferation and contact inhibition as transcriptional mediators of Hippo signaling. *Dev. Camb. Engl.* **135,** 4059–4069 (2008).

290. Nishioka, N. *et al.* The Hippo signaling pathway components Lats and Yap pattern Tead4 activity to distinguish mouse trophectoderm from inner cell mass. *Dev. Cell* **16,** 398–410 (2009).

291. Gumbiner, B. M. & Kim, N.-G. The Hippo-YAP signaling pathway and contact inhibition of growth. *J. Cell Sci.* **127,** 709–717 (2014).

292. Zhou, D. *et al.* Mst1 and Mst2 maintain hepatocyte quiescence and suppress hepatocellular carcinoma development through inactivation of the Yap1 oncogene. *Cancer Cell* **16,** 425–438 (2009).

293. Lu, L. *et al.* Hippo signaling is a potent in vivo growth and tumor suppressor pathway in the mammalian liver. *Proc. Natl. Acad. Sci. U. S. A.* **107,** 1437–1442 (2010).

294. Song, H. *et al.* Mammalian Mst1 and Mst2 kinases play essential roles in organ size control and tumor suppression. *Proc. Natl. Acad. Sci. U. S. A.* **107,** 1431–1436 (2010).

295. Heallen, T. *et al.* Hippo pathway inhibits Wnt signaling to restrain cardiomyocyte proliferation and heart size. *Science* **332,** 458–461 (2011).

296. von Gise, A. *et al.* YAP1, the nuclear target of Hippo signaling, stimulates heart growth through cardiomyocyte proliferation but not hypertrophy. *Proc. Natl. Acad. Sci. U. S. A.* **109,** 2394–2399 (2012).

297. Xin, M. *et al.* Regulation of insulin-like growth factor signaling by Yap governs cardiomyocyte proliferation and embryonic heart size. *Sci. Signal.* **4,** ra70 (2011).

298. Camargo, F. D. *et al.* YAP1 increases organ size and expands undifferentiated progenitor cells. *Curr. Biol. CB* **17,** 2054–2060 (2007).

299. Schlegelmilch, K. *et al.* Yap1 acts downstream of α-catenin to control epidermal proliferation. *Cell* **144,** 782–795 (2011).

300. Zhang, H., Pasolli, H. A. & Fuchs, E. Yes-associated protein (YAP) transcriptional coactivator functions in balancing growth and differentiation in skin. *Proc. Natl. Acad. Sci. U. S. A.* **108,** 2270–2275 (2011).

301. Harvey, K. F., Zhang, X. & Thomas, D. M. The Hippo pathway and human cancer. *Nat. Rev. Cancer* **13,** 246–257 (2013).

302. Dong, J. *et al.* Elucidation of a universal size-control mechanism in Drosophila and mammals. *Cell* **130,** 1120–1133 (2007).

303. Overholtzer, M. *et al.* Transforming properties of YAP, a candidate oncogene on the chromosome 11q22 amplicon. *Proc. Natl. Acad. Sci. U. S. A.* **103,** 12405–12410 (2006).

304. Zender, L. *et al.* Identification and validation of oncogenes in liver cancer using an integrative oncogenomic approach. *Cell* **125,** 1253–1267 (2006).

305. Steinhardt, A. A. *et al.* Expression of Yes-associated protein in common solid tumors. *Hum. Pathol.* **39,** 1582–1589 (2008).

306. Cordenonsi, M. *et al.* The Hippo transducer TAZ confers cancer stem cell-related traits on breast cancer cells. *Cell* **147,** 759–772 (2011).

307. Lei, Q.-Y. *et al.* TAZ promotes cell proliferation and epithelial-mesenchymal transition and is inhibited by the hippo pathway. *Mol. Cell. Biol.* **28,** 2426–2436 (2008).

308. Zhang, N. *et al.* The Merlin/NF2 tumor suppressor functions through the YAP oncoprotein to regulate tissue homeostasis in mammals. *Dev. Cell* **19,** 27–38 (2010).

309. Liu-Chittenden, Y. *et al.* Genetic and pharmacological disruption of the TEAD-YAP complex suppresses the oncogenic activity of YAP. *Genes Dev.* **26,** 1300–1305 (2012).

310. Zhang, T. *et al.* Hepatitis B virus X protein modulates oncogene Yes-associated protein by CREB to promote growth of hepatoma cells. *Hepatol. Baltim. Md* **56,** 2051–2059 (2012).

311. Diep, C. H. *et al.* Down-regulation of Yes Associated Protein 1 expression reduces cell proliferation and clonogenicity of pancreatic cancer cells. *PloS One* **7,** e32783 (2012).

312. Lamar, J. M. *et al.* The Hippo pathway target, YAP, promotes metastasis through its TEAD-interaction domain. *Proc. Natl. Acad. Sci. U. S. A.* **109,** E2441–2450 (2012).

313. Zhou, Z., Zhu, J.-S., Xu, Z.-P. & Zhang, Q. Lentiviral vector-mediated siRNA knockdown of the YAP gene inhibits growth and induces apoptosis in the SGC7901 gastric cancer cell line. *Mol. Med. Rep.* **4,** 1075–1082 (2011).

314. Wang, X., Su, L. & Ou, Q. Yes-associated protein promotes tumour development in luminal epithelial derived breast cancer. *Eur. J. Cancer Oxf. Engl. 1990* **48,** 1227–1234 (2012).

315. Li, V. S. W. & Clevers, H. Intestinal regeneration: YAP-tumor suppressor and oncoprotein? *Curr. Biol. CB* **23,** R110–112 (2013).

316. Barry, E. R. *et al.* Restriction of intestinal stem cell expansion and the regenerative response by YAP. *Nature* **493,** 106–110 (2013).

317. Lian, I. *et al.* The role of YAP transcription coactivator in regulating stem cell self-renewal and differentiation. *Genes Dev.* **24,** 1106–1118 (2010).

318. Xin, M. *et al.* Hippo pathway effector Yap promotes cardiac regeneration. *Proc. Natl. Acad. Sci. U. S. A.* **110,** 13839–13844 (2013).

319. Lavado, A. *et al.* Tumor suppressor Nf2 limits expansion of the neural progenitor pool by inhibiting Yap/Taz transcriptional coactivators. *Dev. Camb. Engl.* **140,** 3323–3334 (2013).

320. Qin, H. *et al.* Transcriptional analysis of pluripotency reveals the Hippo pathway as a barrier to reprogramming. *Hum. Mol. Genet.* **21,** 2054–2067 (2012).

321. Anand, R. *et al.* Toward the development of a potent and selective organoruthenium mammalian sterile 20 kinase inhibitor. *J. Med. Chem.* **52,** 1602–1611 (2009).

322. Yu, F.-X. *et al.* Regulation of the Hippo-YAP pathway by G-protein-coupled receptor signaling. *Cell* **150,** 780–791 (2012).

323. Yu, F.-X. *et al.* Protein kinase A activates the Hippo pathway to modulate cell proliferation and differentiation. *Genes Dev.* **27,** 1223–1232 (2013).

324. Zhao, B. *et al.* TEAD mediates YAP-dependent gene induction and growth control. *Genes Dev.* **22,** 1962–1971 (2008).

325. Guan, K.-L., Yu, F. & Ding, S. Inhibitors of Hippo-Yap Signaling Pathway. (2013). at <https://patentscope.wipo.int/search/en/detail.jsf?docId=WO2013188138>

326. Brodowska, K. *et al.* The clinically used photosensitizer Verteporfin (VP) inhibits YAP-TEAD and human retinoblastoma cell growth in vitro without light activation. *Exp. Eye Res.* **124,** 67–73 (2014).

327. Hau, J. C. *et al.* The TEAD4-YAP/TAZ protein-protein interaction: expected similarities and unexpected differences. *Chembiochem Eur. J. Chem. Biol.* **14,** 1218–1225 (2013).

328. Anbanandam, A. *et al.* Insights into transcription enhancer factor 1 (TEF-1) activity from the solution structure of the TEA domain. *Proc. Natl. Acad. Sci. U. S. A.* **103,** 17225–17230 (2006).

329. Li, Z. *et al.* Structural insights into the YAP and TEAD complex. *Genes Dev.* **24,** 235–240 (2010).

330. Tian, W., Yu, J., Tomchick, D. R., Pan, D. & Luo, X. Structural and functional analysis of the YAP-binding domain of human TEAD2. *Proc. Natl. Acad. Sci.* **107,** 7293–7298 (2010).

331. Fossdal, R. *et al.* A novel TEAD1 mutation is the causative allele in Sveinsson's chorioretinal atrophy (helicoid peripapillary chorioretinal degeneration). *Hum. Mol. Genet.* **13,** 975–981 (2004).

332. Chen, L. *et al.* Structural basis of YAP recognition by TEAD4 in the hippo pathway. *Genes Dev.* **24,** 290–300 (2010).

333. Zhang, Z. *et al.* Structure-Based Design and Synthesis of Potent Cyclic Peptides Inhibiting the YAP-TEAD Protein-Protein Interaction. *ACS Med. Chem. Lett.* **5,** 993–998 (2014).

334. Zhou, Z. *et al.* Targeting Hippo pathway by specific interruption of YAP-TEAD interaction using cyclic YAP-like peptides. *FASEB J. Off. Publ. Fed. Am. Soc. Exp. Biol.* **29,** 724–732 (2015).

335. Lipinski, C. A., Lombardo, F., Dominy, B. W. & Feeney, P. J. Experimental and computational approaches to estimate solubility and permeability in drug discovery and development settings1. *Adv. Drug Deliv. Rev.* **46,** 3–26 (2001).

336. Hughes, J. D. *et al.* Physiochemical drug properties associated with in vivo toxicological outcomes. *Bioorg. Med. Chem. Lett.* **18,** 4872–4875 (2008).

337. Gleeson, M. P. Generation of a Set of Simple, Interpretable ADMET Rules of Thumb. *J. Med. Chem.* **51,** 817–834 (2008).

338. Villoutreix, B. O., Labbé, C. M., Lagorce, D., Laconde, G. & Sperandio, O. A leap into the chemical space of protein-protein interaction inhibitors. *Curr. Pharm. Des.* **18,** 4648–4667 (2012).

339. Labbé, C. M., Laconde, G., Kuenemann, M. A., Villoutreix, B. O. & Sperandio, O. iPPI-DB: a manually curated and interactive database of small non-peptide inhibitors of protein-protein interactions. *Drug Discov. Today* **18,** 958–968 (2013).

340. Hu, Y. & Bajorath, J. Influence of Search Parameters and Criteria on Compound Selection, Promiscuity, and Pan Assay Interference Characteristics. *J. Chem. Inf. Model.* **54,** 3056–3066 (2014).

341. Baell, J. B. & Holloway, G. A. New substructure filters for removal of pan assay interference compounds (PAINS) from screening libraries and for their exclusion in bioassays. *J. Med. Chem.* **53,** 2719–2740 (2010).

342. Zhou, Z. *et al.* Targeting Hippo pathway by specific interruption of YAP-TEAD interaction using cyclic YAP-like peptides. *FASEB J. Off. Publ. Fed. Am. Soc. Exp. Biol.* **29,** 724–732 (2015).

343. Dixon, S. L. *et al.* PHASE: a new engine for pharmacophore perception, 3D QSAR model development, and 3D database screening: 1. Methodology and preliminary results. *J. Comput. Aided Mol. Des.* **20,** 647–671 (2006).

344. Dixon, S. L., Smondyrev, A. M. & Rao, S. N. PHASE: A Novel Approach to Pharmacophore Modeling and 3D Database Searching. *Chem. Biol. Drug Des.* **67,** 370–372 (2006).

345. Sastry, M., Lowrie, J. F., Dixon, S. L. & Sherman, W. Large-Scale Systematic Analysis of 2D Fingerprint Methods and Parameters to Improve Virtual Screening Enrichments. *J. Chem. Inf. Model.* **50,** 771–784 (2010).

346. Duan, J., Dixon, S. L., Lowrie, J. F. & Sherman, W. Analysis and comparison of 2D fingerprints: Insights into database screening performance using eight fingerprint methods. *J. Mol. Graph. Model.* **29,** 157–170 (2010).